Large-eddy simulation and analytical modelling of katabatic winds

Simon Looijen Axelsen

ISBN 978-90-393-5256-4
Institute for Marine and Atmospheric research Utrecht (IMAU)
Faculty of Science, Department of Physics and Astronomy
Utrecht University, The Netherlands

Cover: Langfjordjøkelen, Courtesy R.H. Giesen

Large-eddy simulation and analytical modelling of katabatic winds

Grote wervel simulatie en analytische modellering van katabatische stromingen

(met een samenvatting in het Nederlands)

Proefschrift

ter verkrijging van de graad van doctor aan de Universiteit Utrecht
op gezag van de rector magnificus, prof. dr. J.C. Stoof,
ingevolge het besluit van het college voor promoties
in het openbaar te verdedigen op

maandag 13 januari 2010 des middags om 12:45 uur

door

Simon Looijen Axelsen

geboren op 23 april 1978 te Arendal, Noorwegen

Promotor: **Prof. dr. J. Oerlemans**
Co-promotor: **Dr. H. van Dop**

Contents

1

Introduction

This thesis is concerned with the numerical and analytical modelling of the downslope winds often observed over sloping terrain. In this chapter, the motivation for this study, and an introduction to the methodology is presented. First, a general sketch of the atmospheric boundary layer is given, followed by a description of slope winds and their roles in weather and climate studies. In the past, these slope winds have been studied using analytical and numerical models. Here frequently cited works are summarized. Lastly, an outline of this dissertation is given.

1.1 The atmospheric boundary layer

In scientific textbooks and discussions on meteorology, the atmosphere is frequently divided into multiple regions, and the region immediately above the earth's surface is called the atmospheric boundary layer (ABL). In contrast to regions further aloft, the flow in the ABL is directly influenced by the presence of the surface. As will be explained below, physical processes taking place near the surface produce turbulent motions in the ABL. Turbulence generates swirls of motion, also called turbulent eddies, which act to mix and transport properties (e.g. momentum and heat) throughout the ABL.

1.1.1 The convective boundary layer

The processes in the ABL typically have a diurnal cycle, see Figure 1.1. During the daytime solar radiation heats the earth's surface. Since different soil and vegetation types absorb and emit radiation at different rates, the warming of the overlying air is not uniform. Any spatial temperature difference is associated with a density difference, which gives rise to a buoyancy force. When an

air parcel in a stably stratified environment (e.g. density decreases with height) is heavier than its surroundings (associated with an air parcel being colder than its environment), it must descend in order to reach a level of neutral buoyancy. Analogously, air parcels that are warmer than their environment (e.g. lighter) will start to ascend. As these air parcels ascend, they "push aside" the ambient atmosphere, whereby turbulent eddies are generated. The ascending motion takes place in cell-like structures and is called convection, and the boundary layer is therefore frequently called the convective boundary layer (CBL). The vertical extent of convective cells is typically a couple of kilometres. At the top of the ABL, the ambient atmosphere is stably stratified, which inhibits convective cells to penetrate the free atmosphere overlying the boundary layer. The depth of the CBL can grow through turbulent entrainment of air from the free atmosphere. This takes place in the entrainment zone.
Convection is responsible for transporting water vapour from the surface up to higher altitudes where condensation takes place, whereby clouds are formed. Fair weather clouds, or cumulus clouds, thus originate at the surface. Convection is also responsible for transporting natural and anthropogenic pollutants from the surface to the free atmosphere. The role of convection and cloud dynamics in climate still poses great challenges in the atmospheric sciences.

1.1.2 The stable boundary layer (SBL)

The temperature in the boundary layer decreases during the evening and night due to radiative cooling. During the polar winter this cooling is persistent. The overlaying air is cooled from below and a stably stratified boundary layer is produced. The stable boundary layer (SBL) is also formed by advection of warmer air over a cooler surface (e.g land/sea breeze). In the SBL, buoyancy suppresses vertical motion whereby turbulence is destroyed, and the only turbulence production term is shear: The wind at a couple of metres to hundreds of metres above the surface can be substantial, but must cease at the surface due to friction. In a layman's vision, the rapid change in wind speed close to the ground is responsible for layers of air "stumbling" over slower moving layers below. In the SBL, the shear generated turbulent eddies are typically stretched in the direction of the wind, and since buoyancy limits any vertical motion, the vertical extent of the SBL is much smaller compared to that of the CBL, at most a couple of hundred metres. If the winds are weak, the shear production of turbulence can be sporadic and patchy, allowing upper portions of the SBL to decouple from the surface forcing. In the absence of turbulence, other transport mechanisms such as gravity waves become important (e.g. Nappo, 2002). Due to this complexity, the SBL is difficult to describe and model. In slope flows (introduced below) the wind speed is usually large, and the shear production of turbulence by far exceeds the destruction by buoyancy. In the remainder of this dissertation it is therefore assumed that in the SBL turbulence is the only mechanism for mixing and transport of properties such as momentum and

heat/buoyancy. The reader is referred to Stull (1988) and Garratt (1992) for a general discussion on the convective and stable boundary layers.

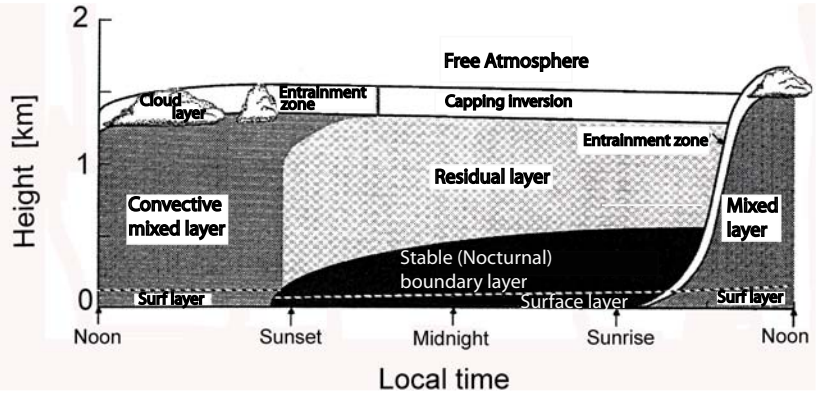

Figure 1.1. Illustration of the atmospheric boundary layer over land during one day. Adapted from Stull (1988).

1.2 Katabatic winds

1.2.1 General characteristics

It is well known that the local weather in mountainous regions are partly determined by thermally driven slope winds. Downslope (katabatic) and up-slope (anabatic) winds arise when there is a horizontal temperature difference between the air at the surface and the environmental air at the same altitude, see illustration in Figure 1.2 for a katabatic flow case. The negative (positive) buoyancy associated with the negative (positive) temperature difference has a component in the downslope (up-slope) direction and induces a katabatic (anabatic) flow.

Figure 1.3(a) illustrates the buoyancy in the katabatic layer. The negative buoyancy is the largest at the surface. The associated temperature difference between the near-surface air parcel and the environment may be several centigrade, and diminishes further aloft, typically at a height[1] of some tens of metres. The decrease in temperature difference (buoyancy) implies that the temperature in the katabatic layer increases with height, i.e. there is a temperature inversion.

Katabatic winds are furthermore characterized by wind profiles persistently exhibiting a wind maximum of the order of several metres per second, see illustration in Figure 1.3(b). The wind maximum is normally located a couple of

[1]Distance perpendicular to the slope.

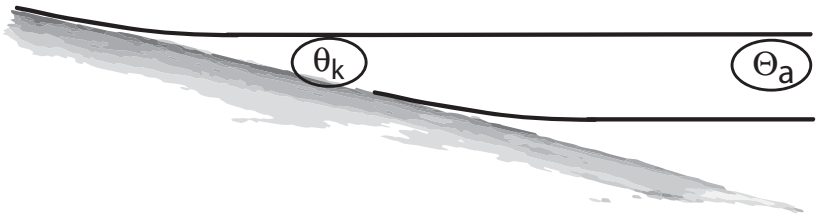

Figure 1.2. Isolines of a potential temperature eld that facilitates the development of katabatic winds. The gure shows an air parcel taking part in the katabatic ow ($_k$), and an ambient air parcel ($_a$) at the same altitude. Due to the surface cooling, the potential temperature of a near-surface air parcel is lower than that of the environment, i.e. $_k <$ $_a$. The surface cooling is therefore also responsible for the curvature of the isolines close to the ground.

metres to tens of metres above the surface. Turbulence in the katabatic layer is produced by wind shear, and is largely responsible for the vertical mixing of momentum and heat in the lowest part of the boundary layer over sloping surfaces.

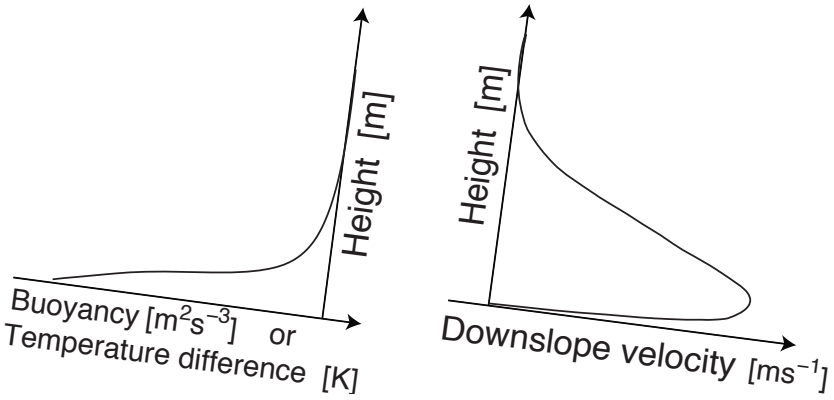

(a) (b)

Figure 1.3. Sketch of the katabatic buoyancy (temperature di erence) (a) and the downslope velocity (b) as functions of height. A typical surface value for the buoyancy (temperature di erence) is $0\,35\,\mathrm{m^2 s^{-3}}$ ($10\,\mathrm{K}$). The wind maximum in (b) has a magnitude of several metres per second and is located a couple of metres to tens of metres above the surface.

The characteristics of katabatic winds (e.g. buoyancy, downslope velocity) do not only vary with height, but also to some degree with downslope distance. Observations have shown that katabatic flows deepen and increase in strength with downslope distance, provided the synoptic forcing being weak or the slope being shallow (e.g. Horst and Doran, 1986; Haiden and Whiteman, 2005; Whiteman and Zhong, 2008). On the other hand, when the ambient atmosphere is strongly stably stratified or the slope angle is large, the katabatic flow is close to one-dimensional, i.e. the flow characteristics do not vary significantly with downslope distance (e.g. Nappo and Rao, 1987; Papadopoulos *et al.*, 1997; Whiteman and Zhong, 2008).

Katabatic winds are common in nature. They have been observed over simple, shallow slopes (e.g. Mahrt and Larsen, 1990), over steep slopes (e.g. Papadopoulos *et al.*, 1997; Papadopoulos and Helmis, 1999), in deep valleys (e.g. Banta *et al.*, 1995, and references herein), and in shallow gullies (e.g. Mahrt, 2001; Soler *et al.*, 2002). Glaciers and ice sheets, which continuously cool the ABL, are also regions with persistent downslope flows. The katabatic winds observed at the ice sheets of Greenland (e.g. Meesters *et al.*, 1997a,b) and Antarctica (e.g. Chiba and Kobayashi, 1986; Kodoma *et al.*, 1989) differ from those over glaciers. The downslope and cross-slope length scales of the ice sheets are much larger than the length scales associated with a glacier. Due to the large length and time scales of the katabatic flow over ice sheets, the Coriolis force becomes important. This force, however, plays only a minor role in the katabatic flow over glaciers. Furthermore, glacier surfaces are usually much steeper than the weakly inclined slopes on Greenland and Antarctica. Finally, whereas ice sheets span vast areas covering any underlying topography, the geometry of glaciers is determined by the surrounding orography. Glaciers are frequently situated in valleys with (ice-free) walls, which limit the cross-slope extent of the flow, and are responsible for a cross-slope variation in the surface buoyancy. Examples of observations of katabatic winds over glaciers are reported in e.g. Van den Broeke (1997a,b), Van der Avoird and Duynkerke (1999), and Smeets *et al.* (1999).

Katabatic winds are partly determined by external factors such as the ambient wind. Mahrt and Larsen (1990) reported that katabatic flows could develop over a gentle slope with weak ambient up-slope wind, provided the ambient atmosphere was very stably stratified. For strong up-slope ambient winds, katabatic flows would not develop, but retard the ambient up-slope winds. In the case of anabatic flows, they observed that the buoyancy force could accelerate the surface flow beyond the ambient speeds.

The stratification of the ambient atmosphere is also an external factor influencing the slope flow. Haiden and Whiteman (2005) and Whiteman and Zhong (2008) observed katabatic winds becoming weaker with increasing ambient stratification. They found that in a strongly stratified boundary layer, the katabatic flow does not vary significantly in the downslope direction. On the other hand, in a weakly stratified boundary layer they found that the mo-

mentum and buoyancy fluxes increase along the slope.

1.2.2 Katabatic winds in the larger picture

Slope winds play an important role in various research areas of the atmospheric sciences. For instance, the diurnal characteristics of precipitation amounts and frequencies can be influenced by complications associated with the atmospheric flow over topography. Sen Roy and Balling Jr. (2004) studied the diurnal rainfall patterns of Hawaii and found that the early morning and late afternoon precipitation maxima were influenced by slope flows. The nocturnal cooling of the air over the coastal slopes facing the East induced a katabatic flow, which near the surface converged with the easterly trade winds and produced an uplift mechanism. On the other hand, during the daytime, anabatic sea-breezes on the West coast (leeward slope) converged with the trade winds.

Katabatic and anabatic flows can furthermore play an important role in the dispersion of pollutants in valleys. Banta *et al.* (1997) studied how slope flows influenced the concentration of ozone and pollutants during photochemical air pollution episodes in the Lower Fraser Valley near Vancouver, BC, Canada. They found that the daytime upvalley flows carried polluted air into tributary valleys. The concentration of ozone and pollutants measured in the downvalley flow during the night was much lower, suggesting that the air had been cleansed in the tributary valleys.

The turbulent katabatic winds over glaciers, also called glacier winds, play an important role in the surface energy budgets of the ice. In the ablation zone of glaciers, the ice is at the melting temperature during much of the year. When this is the case, any warming of the ice, e.g. by katabatic flows venting heat from the atmosphere to the surface, will cause melting. This is illustrated in Figure 1.4, which shows the monthly averaged surface energy fluxes measured at the Morteratsch glacier, Switzerland. The data, obtained using an automatic weather station located in the ablation zone, are averaged over the period October 2000 to September 2006, see Oerlemans and Klok (2002) and Giesen *et al.* (2008) for more details. The figure shows the annual variability of the net radiation (sum of the incoming solar short-wave and the outgoing long-wave radiation), the sensible heat flux (the turbulent transport of heat from the atmosphere to the ice pack), the latent heat flux (associated with sublimation/evaporation/condensation), and the subsurface energy flux (the energy penetrating into the subsurface ice layers). Positive fluxes are directed towards the surface. Melting takes place if the sum of these terms is positive, provided that the ice is at the melting temperature. From November to March, the nocturnal radiative cooling exceeds the diurnal solar heating, yielding a negative net radiative energy flux. The sensible heat flux balances this cooling by transporting heat from the atmosphere to the surface. The melting starts in March, and by April the net radiation is positive. At that

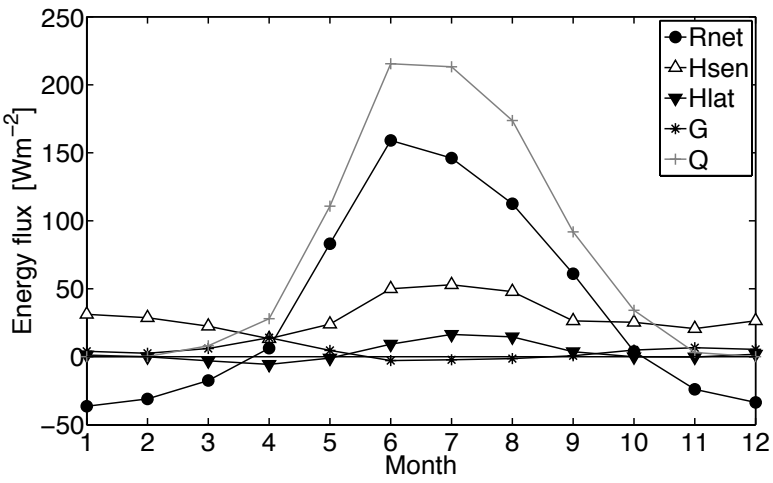

Figure 1.4. Surface energy budget of the Morteratsch glacier, Switzerland: Monthly averaged values of the net radiation (Rnet), sensible heat flux (Hsen), latent heat flux (Hlat), and subsurface heat flux (G). Their sum (Q) equals the energy available for melt if the ice is at the melting temperature. Courtesy R.H. Giesen.

time, the radiation, the sensible heat flux, and the subsurface energy flux are approximately equal. The small negative latent heat flux is associated with sublimation taking place at the surface. During the summer period, the largest two terms are the net radiation and the sensible heat flux, and they contribute on average by respectively ~ 70 and $\sim 25\,\%$ to the melt energy. The relative contribution to the melt energy by the latent heat flux ($\sim 7\,\%$) is small compared to the sensible heat flux contribution. In the fall season, only the net radiation and sensible heat flux contribute to the melt energy.

Other observations of katabatic winds over glaciers and ice sheets have also shown that the relative contribution by the sensible heat flux to the surface energy budget is substantial. Giesen *et al.* (2009), citing previous observations, list sensible heat flux contributions in the range 17 to 49 %.

The melting of glaciers plays an important role for the sustainability of agriculture. For instance, on a regional scale, glaciers supply melt water for irrigation systems (e.g. Oerlemans, 1998), as well as for hydropower reservoirs. Understanding glacier melt is essential also from the perspective of climate change. The rapid decrease in glacier lengths during the last couple of decades has been linked to global warming (e.g. Oerlemans, 1994). The melt of glaciers also plays a contributing role in the observed sea level rise; the largest estimate by the Intergovernmental Panel on Climate Change (Solomon *et al.*, 2007) on the ice volume constituted by glaciers not immediately adjacent to the ice sheets of Greenland and Antarctica was 0.37 m sea level

equivalent. On a larger scale, the katabatic winds over the vast ice sheets on Antarctica and Greenland play an important role in the weather and climate of these areas (e.g Pettré *et al.*, 1990; Van den Broeke *et al.*, 1997; Oerlemans, 1998; Van As and Van den Broeke, 2007; Van den Berg *et al.*, 2008).

1.3 Analytical models of katabatic flows

In order to better understand katabatic flows, several analytical models have been presented. Due to the non-linearity of the equations of motion, these analytical models only offer a solution to simplified governing equations. Several simplifications are discussed in Mahrt (1982), one being the assumption that the flow only varies with height; Mahrt called this 'equilibrium flow'. This assumption is approximately valid for slope winds in a strongly stratified environment, or over a steep slope (e.g. Nappo and Rao, 1987; Papadopoulos *et al.*, 1997; Haiden and Whiteman, 2005; Whiteman and Zhong, 2008). One of the first analytical solutions to an equilibrium flow was presented by Prandtl (1942). His classical model describes katabatic winds along a uniformly cooled sloping planar surface in a stably stratified atmosphere. In the downslope momentum equation, acceleration by buoyancy is opposed by a momentum flux divergence, whereas in the thermodynamic energy equation, the along-slope advection of warm air is balanced by the buoyancy flux divergence induced by the surface cooling. The turbulence fluxes of momentum and buoyancy are modelled using first-order closure, i.e. second-order moments are expressed in terms of first-order moments. For example, the momentum flux (second-order) is assumed to be proportional to the vertical gradient of the velocity field (first-order). Prandtl used a fixed proportionality constant, which can be used to fit the model results to e.g. observations. The Prandtl solution shows a layer of negative buoyancy near the surface, capped by a layer of slightly positively buoyant air (further aloft the oscillation in the profile around neutral buoyancy quickly dampens out). The associated profile of downslope velocity exhibits a low-level wind maximum, topped by a weak reverse flow. Observations of katabatic winds have shown that in some cases an appropriately tuned Prandtl model qualitatively reproduces the observed profiles of downslope velocity and buoyancy (e.g. Papadopoulos *et al.*, 1997; Grisogono and Oerlemans, 2001a).
Several extensions to the one-dimensional Prandtl model have been proposed. Grisogono and Oerlemans (2001a,b) introduced height-dependent turbulence exchange coefficients and presented analytical solutions valid in the WKB[2] approximation. Grisogono (2003) further extended the model to include time dependence.
The time- and spatial scales of the katabatic winds over the vast land areas of Greenland and Antarctica are large, whereby the Coriolis force becomes im-

[2]Wentzel - Kramers - Brillouin.

portant. Extensions to the Prandtl model have made provision for the Coriolis force (e.g. Gutman and Malbakhov, 1964; Lykosov and Gutman, 1972; Gutman and Melgarejo, 1981; Egger, 1985; Stiperski *et al.*, 2007; Kavcic and Grisogono, 2007), some in combination with external winds, radiative damping and time dependence. The various models treat the exchange coefficients differently, from constants to more complex height-dependent functions. As shown by Gutman and Malbakhov (1964), the buoyancy and cross-slope velocity fields spread inexorably upward when the Coriolis force is included. Egger (1985) argued that these fields vanish when either an external geostrophic wind or a radiative damping is taken into account. However, in the case of an imposed geostrophic wind, unrealistically large values (exceeding $100\,\mathrm{ms}^{-1}$) of those winds were required to prevent the continued upward growth of the buoyancy and cross-slope velocity fields. More recently, Kavcic and Grisogono (2007) argued that the upward growth would diminish if the turbulence exchange coefficients far above the surface would approach a small value (but not zero), a result questioned in the review by Shapiro and Fedorovich (2008).

Katabatic winds in a weakly stratified environment or over a shallow slope deepen and increase in strength with downslope distance (e.g. Horst and Doran, 1986; Haiden and Whiteman, 2005; Whiteman and Zhong, 2008). This downslope variability of the katabatic flow structure is captured by the so-called hydraulic models. Examples of this type of model are given in Fleagle (1950), Ball (1956), Ellison and Turner (1959), and Manins and Sawford (1979). By vertically integrating the equations of motion, mass conservation and (usually) the thermodynamic energy equation, the hydraulic models consider layer-mean budgets. Closures in these models usually involve the neglect of some terms in the governing equations, the introduction of empirical shape factors, and the specification of an entrainment rate at the top of the katabatic layer. The immediate benefit of hydraulic models over the models that only describe the vertical structure of katabatic winds (e.g. Prandtl type), is that they permit a downslope variation of the flow. Hydraulic models have been used to derive slope flow parameterizations that are frequently used in numerical weather prediction and climate models (see also next section). Lastly, improving hydraulic models can be achieved by further advancing models of the Prandtl type and providing appropriate vertical averaging.

1.4 Numerical modelling of katabatic winds

Analytical models provide conceptual descriptions of slope winds, but can only retain a limited number of terms in the momentum and thermodynamic energy equations. This has prompted the use of numerical models, which can solve complex equations that may include non-linear terms and the effects of e.g. radiation and phase change.

In this introduction, some of the models that have previously been used to

study katabatic winds are summarized. The discussion is placed in the context of the turbulence kinetic energy (TKE) spectrum (also referred to as the energy spectrum), which is schematically depicted in Figure 1.5.

The large-scale atmospheric flow is associated with small wave numbers κ.

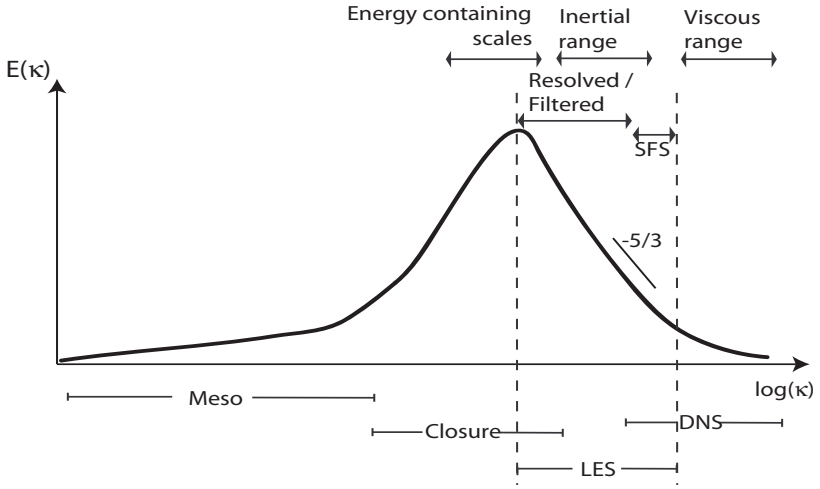

Figure 1.5. A schematic of the TKE spectrum E as a function of the wave number κ. The relevant length scales related to meso-scale, closure, LES, and DNS modelling of katabatic winds are shown as bars. Note that the first axis is chosen to emphasize the length scales relevant to LES. Meso-scale and closure models all solve the RANS equations, the distinction in the figure is motivated in the text. In LES, the motion of the large turbulent eddies are resolved explicitly by filtering the governing equations, hence the terminology "resolved" and "filtered motions". The filter should be in the inertial sub-range, which has a $-5/3$ slope in the energy spectrum. Turbulent eddies, whose integral length scale is smaller than the filter width, are treated in the SFS model. See text for abbreviations. Figure adapted from Wyngaard (2004).

It is frequently assumed that the flow at these scales can be described as being the sum of a mean flow and fluctuations, the latter being zero on average. Mathematically, these flow problems can be studied by solving the Reynolds[3] Averaged Navier-Stokes (RANS) equations (e.g Garratt, 1992). Below a review of some aspects of two types of numerical models solving the RANS equations (e.g. the meso-scale and closure models) is presented. At smaller length scales, the atmospheric flow is essentially turbulent. Large-eddy simulation (LES) is a technique that explicitly solves the motion of the largest turbulent eddies, whereas a parameterization is used to model the effect of small-scale turbulent eddies. Lastly, in direct numerical simulation (DNS) no parameterization

[3]The Reynolds number is a dimensionless number used to characterize how turbulent a flow is, e.g. Stull (1988).

is used, permitting the governing equations to be solved for very small-scale turbulence.

1.4.1 RANS models

In numerical weather prediction and climate models, the effect of turbulence on the atmospheric motions is frequently modelled using low-order turbulence closure. These models are classified as meso-scale models. Special versions of these RANS models have been developed to explicitly study the first and higher-order moments of boundary layer flows. Instead of using bulk parameterizations, these models use parameterizations of higher-order turbulence moments, which is done by applying closure theory, hence the models are referred to as closure models. Although they can be used to solve the RANS equations for different length scales, closure models are in Figure 1.5 arranged according to the turbulence length scales encountered in katabatic flows.

Meso-scale models

Meso-scale models have for some time been used to study katabatic winds in several settings. For example, Parish (1984) performed a numerical study of the katabatic winds over Antarctica, and Pettré *et al.* (1990) studied the influence of katabatic winds on the Antarctic circulation. These simulations used idealized atmospheric forcings. More recently, realistic atmospheric forcings have also been used, e.g. Van Lipzig *et al.* (1999) simulated the Antarctic atmosphere using ECMWF[4] reanalysis data to force the prognostic variables at the boundaries, Bromwich *et al.* (2001) used the Polar MM5 model to simulate two months of observations (analysis from ECMWF, automatic weather stations, and instrumented aircraft observations) of katabatic winds over the Greenland ice sheet, and Klein *et al.* (2001) used the same data to validate the Norwegian Limited Area Model.
Whereas the above studies focussed on katabatic flows over the vast areas of Antarctica and Greenland, meso-scale modelling of slope winds confined to smaller regions has also been performed. This requires a finer numerical resolution, which has become available during the last decade. Söderberg and Parmhed (2006) used the Coupled Ocean/Atmosphere Meso-scale Prediction System to numerically simulate the katabatic flows observed over an outflow glacier. The finest horizontal resolution was 3 km, and in the vertical direction, the lowest model level was at 1 m with 2 m intervals up to 21 m, and 21 levels were below 190 m. The initial and lateral boundary conditions were provided using data from an ECMWF analysis. In a different study, Zhong and Whiteman (2008) used the Regional Atmospheric Modelling System to numerically simulate observations over a gentle slope (1.6 °) in the Salt Lake Valley, Utah, U.S. The topography of this valley was accounted for by using three terrain

[4]European Center for Medium-Range Weather Forecasts

cross-sections. The finest horizontal resolution was 250 m, and in the vertical direction 15 levels were within the lowest 50 m and 6 within the lowest 15 m. Evidently, meso-scale models have several capabilities, e.g. the ability of using real atmospheric forcings and realistic topography. On the other hand, these models were initially not designed to study the detailed structure of the planetary boundary layer. Instead, they use bulk parameterizations, which are frequently derived from observations or turbulence-resolving numerical models such as LES.

Closure models

In this type of models, the effect of turbulence on the mean flow is accounted for by including higher-order moments in the governing equations. Subsequently, the prognostic equations for the higher-order moments must be solved, which is only possible by using closure theory, i.e. higher-order moments are expressed in terms of lower-order moments. Several authors have used closure models to study katabatic winds: Rao and Snodgrass (1981); Doran and Horst (1983); Arritt and Pielke (1986), and Denby (1999) presented vertical profiles of first and second-order moments, depending on the order of their closure models. Other papers have focussed on the downslope variability of katabatic winds, e.g. Yamada (1983) and Nappo and Rao (1987).
Several of the closure models mentioned above apply the 1.5-order closure introduced by Delage (1974), in which the turbulent exchange coefficients are modelled as the product of the square root of the TKE and a length scale. The latter was related to the local Monin-Obukhov (MO) length scale. Denby (1999) argued that the local MO length scale goes to zero at the height of the wind maximum, causing a decoupling of the flow. Since katabatic winds do not experience such a decoupling, he proposed a second-order closure model. Using input data from three measurement campaigns, Denby (1999) showed that his model was capable of reproducing both mean and flux profiles when the flow was almost one-dimensional and the turbulence was locally determined.
Since closure models parameterize higher-order moments, they do not require as fine a numerical mesh as other turbulence resolving models like LES and DNS (discussed below). However, the drawback of closure models is that they rely on a set of closure constants that must be determined empirically. Moreover, in order to obtain agreement between model results and observations, tuning is frequently required.

1.4.2 LES

LES is an alternative to closure models and builds on the turbulence theory. The atmospheric motion in the boundary layer contains turbulent eddies of various sizes. Most of the turbulence energy is contained in the large eddies, which become unsteady and break, whereby small eddies are formed. The energy of

the large eddies is cascaded down to the smaller-scale eddies. Finally, on a very small scale, the energy is cascaded down to the small (assumed) isotropic turbulent eddies where it is dissipated. In LES, the motions of the large eddies are explicitly resolved, hence the terminology "resolved motions". These large eddies are distinguished from the small eddies by filtering the governing equations. The "resolved motions" are therefore also called "filtered motions". The filter should lie in the inertial sub-range (e.g. Pope, 2000), and should be larger or at least equal to the numerical grid spacing (e.g. Geurts, 2004). The effect of the small, unresolved eddies on the mean flow has to be parameterized. These parameterizations form the subfilter-scale (SFS) model.
In the early days of LES, the technique was used to study the CBL. The turbulence length scales in the SBL are much smaller than in the CBL, which implies that a smaller filter width and thus also a finer numerical grid are needed. Due to high computational costs, LES studies of the SBL were first introduced in the early nineties. Mason and Derbyshire (1990) used their LES results, as well as other numerical models, to review the theory and observations of the SBL presented by Nieuwstadt (1984). More recently, Beare *et al.* (2006), and Van Dop and Axelsen (2007) also simulated the SBL, and found that the turbulence characteristics obtained from LES were in good agreement with the majority of Nieuwstadt's SBL observations.
Only a small number of LES studies of the sloping boundary layer have been carried out. Schumann (1990) simulated anabatic flow for a variety of slope angles and surface roughnesses, whereas Skyllingstad (2003) used LES to study katabatic flow subject to an imposed cross-slope flow. Later Smith and Skyllingstad (2005) simulated katabatic flow over a surface with a non-constant slope angle. These papers warrant a thorough discussion, which is given in Chapters 3 and 4.

1.4.3 Direct numerical simulation

On the right end of the energy spectrum (e.g. Figure 1.5), DNS numerically solves the governing equations of turbulent flows having low to moderately high Reynolds numbers. DNS of katabatic winds is an emerging branch in the atmospheric sciences (e.g. Fedorovich and Shapiro, 2009). Shapiro and Fedorovich (2008) performed a DNS study of katabatic flows subject the Coriolis force. They studied the effect of two different surface buoyancy fields. In one case, the surface buoyancy was uniform, whereas in the second case, the surface buoyancy field was constant in the downslope direction, but had a finite width, i.e. they studied katabatic winds induced by an isolated strip. An important finding was that two of the four flow variables would spread inexorably upward, i.e. for a homogeneous surface buoyancy, the buoyancy and cross-slope velocity spread continuously upward, whereas for the isolated strip case, the downslope and slope-normal velocities would not reach a steady-state. In idealized katabatic flows subject to the Coriolis force, this upward spread is

attributed to turbulence mixing. Shapiro and Fedorovich (2008) found that the upward growth could only diminish if either the eddy viscosity (momentum) or eddy diffusivity (heat) coefficients were identically zero starting from some height. More realistically is, which the authors also pointed out, that secondary processes may, if persistent, play a vital role in determining the structure of the steady-state flow.
The numerical simulations and analytical work presented in Shapiro and Fedorovich (2008) illustrate the importance of turbulence on the katabatic flow. In DNS, the turbulent motions are numerically resolved down to the molecular length scale. This requires a fine resolution, which is also the drawback of DNS. With the present day computers, it is possible to numerically simulate turbulent flows with Reynolds numbers of the order 10^4. Atmospheric Reynolds numbers are, however, several orders of magnitude larger. DNS studies are therefore of idealized flows, and generally cannot resolve the largest turbulent eddies.

1.5 Dutch Atmospheric Large-Eddy Simulation (DALES)

In the Netherlands, there is a small research community that studies the dynamics of the ABL. The participants are affiliated with Utrecht University, Wageningen University, the technical university of Delft, the Royal Dutch Meteorological Institute, and some institutes abroad.
The strength of the group is that a common LES code is used, called DALES. The code, which is written in Fortran, was brought to the Netherlands by Frans Nieuwstadt and documented in Nieuwstadt and Brost (1986). Since its introduction in the Dutch ABL community, several improvements have been made, and many physical processes have been coded. The latest version, 3.1, was released in February 2009. When version 3.0 was released the code had undergone a complete overhaul. Results from versions 2.0 and 3.0 (v2 and v3 for short) are presented in this dissertation, see next paragraph for more details.

1.6 This thesis

This thesis discusses several aspects of numerical and analytical modeling of the (sloping) ABL. Chapter 2 introduces the governing equations and summarizes how these are solved numerically using LES. Using DALES v2, the sensitivity to numerical resolution and filter width is studied, and the model results are compared to a previous LES intercomparison study (e.g. the GABLS study by Beare *et al.*, 2006) and to observations from the horizontal SBL.
The subsequent two chapters describe LES studies of katabatic winds. Version 3 of DALES is used. In order to simulate the boundary layer flow over a

sloping terrain, adjustments to the numerical code are required. In Chapter 3 the modifications and novelties in DALES v3 are discussed, and the numerical model's ability to simulate slope winds is verified by comparing model output to observations.

Chapter 4 investigates how mean and turbulence profiles of katabatic flow are influenced by changes to external parameters such as the slope angle, the stratification of the ambient atmosphere, and the surface forcing. Analytical expressions for estimating the surface buoyancy flux are derived from the analytical models by Prandtl (1942) and Grisogono and Oerlemans (2001a,b) and compared to the LES results, and to observations of katabatic winds.

The development of numerical models has during the last couple of decades enabled the simulation of boundary layer flows subject to complex forcings. However, analytical models may provide a conceptual picture of these boundary layer flows. In Chapter 5, a new analytical model is presented, which can be used to study katabatic winds subject to a cross-slope variability in the surface buoyancy.

Throughout this dissertation a variety of symbols and abbreviations are used. They are listed in Appendix A.

2

Large-eddy simulation of stable boundary layers over a horizontal surface

The concept of large-eddy simulation (LES) is summarized. LES is a tool that can be used to study the turbulent motion in the ABL. It assumes that by filtering the governing equations, the motions of the largest eddies can be resolved explicitly, whereas the so-called subfilter-scale (SFS) model parameterizes the effect of the small eddies on the mean flow. LES results therefore depend on the filter, which in turn is related to the numerical resolution. The effect of the filter and the resolution is studied by simulating the stable boundary layer (SBL), and the results are compared to the results from the GABLS intercomparison study (e.g. Beare *et al.*, 2006).

The effect of resolution is studied using three numerical meshes. The coarsest resolution experiences laminarization, and its energy spectrum does not show a clear dissipation region. The two finer resolutions are not subject to laminarization, and both show energy spectra with a dissipation region. The fluxes and mean fields show that the two finest resolutions produce comparable results.

Four different filter width definitions have been tested using the finest resolution. The filter definitions are based on a buoyancy length scale or a shear length scale. Furthermore, we have kept the turbulent exchange coefficients constant, and also defined a filter width that is larger than the numerical grid in the bulk of the boundary layer. The largest difference between the simulations is the SFS contribution to the total turbulent kinetic energy. Moreover, the energy budgets show a non-vanishing numerical diffusion for all simulations, and that the smallest numerical diffusion is found when the filter width is larger than the numerical resolution. The numerical results are also compared to the observations by Nieuwstadt (1984), and the agreement is satisfactory. However, there is no strong evidence for z-less scaling, and the observations do not answer which SFS parameterization is to be preferred. Based on our results and conceptual grounds, we recommend using a filter width that is larger than the grid distance.

2.1 Introduction

The first successfully performed large-eddy simulation (LES) studies of the atmospheric boundary layer (ABL) date back to the late sixties (e.g. Lilly, 1968; Deardorff, 1976). Since then, LES has been used in an overwhelming amount of studies that have mainly focussed on dry and moist convective boundary layers (CBL). For example, Deardorff (1980) used LES to study turbulence and entrainment within mixed layers containing stratocumulus, and looked at how a parameterized cloud-top radiative cooling would influence the profiles of these clouds. His numerical results eliminated most of the assumptions invoked in theories of cloud-capped mixed layers, but suffered from disadvantages which included poor resolution, and large truncation errors in and above the capping inversion. Later, Siebesma and Cuijpers (1995) used LES to simulate the observations gathered during the BOMEX[1] campaign. Their numerical results indicated that the mass flux paramterization used in numerical weather prediction models was ten times too active, and that when adopting entrainment and detrainment rates obtained from LES, the mass flux schemes produced realistic mass fluxes and cloud excess values for moisture and heat (Siebesma and Holtslag, 1996).

The neutral boundary layer has also been studied using LES . Andrén *et al.* (1994) used four different LES codes to simulate a neutrally stratified Ekman layer that was limited in depth by a stress-free rigid lid. They studied the LES sensitivity to subfilter-scale (SFS) model assumptions and numerical methods, and found that the profiles of first- and second-order moments, as well as the budgets of resolved-scale second-order moments, in the lowest third of the boundary layer depended on the SFS model. When using a common SFS model, the results from the four codes converged, implying that the SFS model rather than the various numerics influenced the LES results.

Because of the high computational costs, LES studies of the SBL were first introduced in the early nineties. Mason and Derbyshire (1990) used their LES results, as well as other numerical models to review Nieuwstadt's (Nieuwstadt, 1984) theory and observations of the SBL. Although today's computers are much more powerful, LES studies of the SBL are still difficult. The difficulty lies in the fact that the eddies are so small that it is numerically difficult to keep the flow turbulent at moderate or low resolutions. For this reason, some simulations have started from the outset with a turbulent CBL (e.g. Andrén, 1994), which would generate turbulence kinetic energy (TKE), and after switching off the convection and introducing a small negative heat flux, an SBL formed. However, it is questionable if the latter could be considered stationary after some time. More recently, with increasing computer power, moderately stable SBLs have been simulated, e.g. Kosović and Curry (2000). They imposed initial and boundary conditions using the dataset from BASE[2] and studied a

[1] The Barbados Oceanographic and Meteorological Experiment.

[2] Beaufort Sea Arctic Stratus Experiment

clear-air SBL as it approached a quasi-steady-state. They did this for different latitudes, surface cooling rates, geostrophic winds, inversion strengths and surface roughnesses. An overall agreement was found between the LES results and the observations, and with Nieuwstadt's analytical model.
The case by Kosović and Curry (2000) was more recently revisited in the LES intercomparison study reported on in Beare *et al.* (2006). The latter is a part of GABLS[3], which was an initiative to understand and improve the parameterization of SBLs in large-scale models. The LES intercomparison study showed that all participating models produced successful simulations, but that the spread between the different models was larger than for LES studies of the CBL. The results were found to be sensitive to resolution as well as the SFS model. Lastly, the authors concluded that the results provided improved understanding of the SBL and motivation for future development of parametrizations of the SBL.
The SBL over a sloping terrain is often characterized by the presence of downslope winds. In the subsequent two chapters, these winds are studied using LES. Prior to doing so, it is important to verify that our numerical code can simulate the the SBL above a flat surface. In this chapter, we perform such a test by simulating the case by Kosović and Curry (2000), and compare our results to the GABLS intercomparison study, and to Nieuwstadt's observations. Our main emphasis will differ slightly from that of the GABLS study, we shall focus on the filter width definition (also called filter parameterization), and only give some consideration to the numerical resolution.
This chapter is divided as follows: In the next section we introduce the governing equations. Section 2.3.1 explains the concept behind LES, and summarizes the most commonly used SFS models, where special attention is paid to our SFS model. The different length scales used in LES and numerical diffusion are also discussed. In section 2.4, our numerical model is sketched, followed by the results in Section 2.5, and concluding remarks in Section 2.6.

2.2 Governing equations

The density of air varies only slightly in the ABL. Any change in density from a constant reference density affects the buoyancy the most, and the general practice is therefore to replace the density by a constant mean value, ρ_0 , except in the buoyancy term in the vertical momentum equation. This is called the Boussinesq approximation (e.g. Holton, 1992). Under this approximation the continuity equation reads (using the Einstein summation notation)

$$\frac{\partial u_i}{\partial x_i} = 0, \tag{2.1}$$

with $i = 1, 2, 3$. u_i are components of the velocity vector $\vec{v}$, which has the components u, v and w in the x, y and z-directions, respectively. Using Equa-

[3]Global Energy and Water Cycle Experimet Atmospheric Boundary Layer Study

tion (2.1) in the Navier-Stokes equation for momentum, valid for a rotating (Eulerian) reference frame, one gets (e.g. Kundu and Cohen, 2004)

$$\frac{\partial u_i}{\partial t} = -\frac{\partial u_i u_j}{\partial x_j} - \frac{1}{\rho_0}\frac{\partial p}{\partial x_i} - 2\epsilon_{ijk}\Omega_j u_k + \frac{\theta - \Theta_a}{T_0} g\delta_{i3} + \nu\frac{\partial^2 u_i}{\partial x_j \partial x_j} + S_i^m. \quad (2.2)$$

In an Eulerian description, the time rate of change of the flow in one point $\vec{x}$ in space is considered. This time rate of change of momentum is given by the left hand side. Any momentum transport to or from $\vec{x}$ is accounted for by the advection term, the first term on the right hand side (rhs). The second term on the rhs is the acceleration due to differences in pressure p. For atmospheric motions with time scales of several hours, the rotation of the earth becomes important. In the third term on the rhs, Ω_i are the components of the earth's rotation vector, and ϵ_{ijk} is the Levi-Civita symbol. The potential temperature θ is defined as the temperature an air parcels would have if it was brought adiabatically to a reference pressure. At location $\vec{x}$, the potential temperature may differ from that of the ambient atmosphere, Θ_a. The relative difference in potential temperatures (scaled by g/T_0 with g and T_0 being the constant of gravity and a reference temperature, respectively) gives rise to a buoyancy force, the fourth term on the rhs. Here δ_{ij} is the Kronecker-Delta function. The fifth term is the molecular dissipation term with ν being the molecular kinematic diffusion coefficient of momentum. The term S_i^m represents any sources or sinks not accounted for by the previous terms, such as a large-scale forcing. In this dissertation these sources/sinks (if any) are parameterized in a simple manner, and the S_i^m term is therefore discarded in the further considerations of the momentum equation.
Due to the buoyancy term in (2.2), the evolution of the potential temperature must be determined. The temporal change of the potential temperature field at $\vec{x}$ is governed by the thermodynamic energy equation

$$\frac{\partial \theta}{\partial t} = -\frac{\partial u_j \theta}{\partial x_j} + \kappa\frac{\partial^2 \theta}{\partial x_j \partial x_j} + S^\theta. \quad (2.3)$$

On the left hand side is the time rate of change of θ. The first term on the rhs is the advection term, and the second is the molecular diffusivity term with κ being the thermal diffusivity coefficient. S^θ represents sources and sinks such as solar heating and radiative cooling. We shall in the remainder assume that these sources/sinks are at the surface and that they can be parameterized, e.g. by prescribing a surface temperature change or a surface heat flux. Moreover, we will only consider dry atmospheres, and the processes of phase change (a.o. evaporation and condensation) are therefore neglected.

2.3 LES and SFS modelling

2.3.1 The concept of LES

In high Reynolds number flows, there is a large range of turbulent eddy sizes, and it is well known that present day computers are not sufficiently powerful to provide a numerical solution for all scales. The largest eddies, which contain the most energy, depend on the large-scale flow (e.g. synoptic-scale flow). The smallest eddies, on the other hand, are believed to have a more isotropic structure, and parameterization based on studies of turbulence are therefore applicable (e.g. Pope, 2000).
In LES studies of turbulent flows, the smallest scales are separated from the largest by means of a filter. Subsequently, the Navier-Stokes equation for the filtered (large-scale) quantities are solved numerically, whereas the effect of the small-scale eddies on the flow is parameterized. By a filtering process we separate the large-scale motion from the smaller scales. Spatial filtering is achieved by introducing a filter function G, which yields the filtered velocity $\overline{u}_i$ (filtered quantities are denoted by an overbar),

$$\overline{u}_i(\vec{x}) = \int G(\vec{x} - \vec{x''}) u_i(\vec{x''}) d^3\vec{x''}.$$

The unresolved motion u_i' is defined as the difference between the actual velocity and the filtered velocity,

$$u_i' = u_i - \overline{u}_i.$$

There are different filters available. The most important filters are the box-, Gaussian- and the sharp spectral filters. With the box filter, $\overline{u}_i(\vec{x})$ is the average of $u_i(\vec{x''})$ in the interval $\vec{x} - \lambda/2 < \vec{x''} < \vec{x} + \lambda/2$, and the Gaussian filter function is the Gaussian distribution with a zero mean and variance $\sigma^2 = \lambda^2/12$ (e.g. Leonard, 1974). The filter width is denoted by λ, and is discussed below. The wave number corresponding to the filter is κ_λ. The sharp spectral filter resolves all motions of eddies whose length scales l are such that $\kappa_l < \kappa_\lambda$. More details on different filters and implications can be found in e.g. Sagaut (1998), Pope (2000) and Geurts (2004).
The equations for the evolution of the filtered velocity fields are derived from the Navier-Stokes equations, the difference being a residual stress tensor, τ_{ij}^{SFS}. Below are the filtered form of the Boussinesq conservation equations for mass, momentum and thermodynamic energy i.e. the filtered version of (2.1) - (2.3),

with the molecular viscosity and heat transfer having been neglected:

$$\frac{\partial \overline{u}_i}{\partial x_i} = 0, \tag{2.4}$$

$$\frac{\partial \overline{u}_i}{\partial t} = -\frac{\partial \overline{u}_i\,\overline{u}_j}{\partial x_j} - \frac{\partial \overline{\pi}}{\partial x_i} - 2\epsilon_{ijk}\Omega_j\overline{u}_k + \frac{\overline{\theta}-\Theta_a}{T_0}g\delta_{i3} - \frac{\partial \tau_{ij}}{\partial x_j}^{\mathrm{SFS}}, \tag{2.5}$$

$$\frac{\partial \overline{\theta}}{\partial t} = -\frac{\partial \overline{u}_j\,\overline{\theta}}{\partial x_j} - \frac{\partial \tau_{\theta_j}}{\partial x_j}^{\mathrm{SFS}}. \tag{2.6}$$

The SFS stress tensor and heat flux (indicated by superscript SFS) are given by, respectively

$$\tau_{ij}^{\mathrm{SFS}} = \overline{u_i u_j} - \overline{u}_i\,\overline{u}_j - \tfrac{2}{3}\overline{e'}\delta_{ij}, \quad \text{and} \tag{2.7}$$

$$\tau_{\theta j}^{\mathrm{SFS}} = \overline{u_j\theta} - \overline{u}_j\overline{\theta}, \tag{2.8}$$

where $\overline{e'}$ is the SFS TKE. The modelling of the SFS fluxes and TKE is discussed in the next section. The reason for subtracting $2\overline{e'}/3$ from the SFS stress tensor is the explicit separation of the terms into isotropic and anisotropic categories (Cuijpers, 1994). In the isotropic turbulence, the sum τ_{ii}^{SFS} equals zero, thus the normal stresses vanish. The term $2\overline{e'}/3$ is added back in the pressure term, yielding the modified pressure

$$\overline{\pi} = \frac{\overline{p}}{\rho_0} + \frac{2}{3}\overline{e'}, \tag{2.9}$$

where $\overline{p}$ is the filtered pressure field.
The aim of LES is to resolve the most energetic motions. Therefore, the model domain size should be large enough to contain the large energy-carrying eddies. At the same time, the filter size should be chosen such that the energy of the residual small-scale motion is a small fraction of the total energy. These residual motions are treated in the SFS model. A short overview of different SFS models is given below.

2.3.2 SFS models

The most SFS models encountered in literature are the Smagorinsky model, the Smagorinsky model with backscatter, the dynamic Smagorinsky, and the TKE model. Below we give a short introduction to the first three SFS models. In this study we use the TKE model, which is discussed in more detail.
The Smagorinsky model in a neutral case assumes that the only source of SFS TKE is due to shear, and relates the residual stress to the filtered rate of strain, i.e.

$$\tau_{ij}^{\mathrm{SFS}} = -2\nu_r\overline{S}_{ij},$$

where

$$\overline{S}_{ij} = \frac{1}{2}\left(\frac{\partial \overline{u}_i}{\partial x_j} + \frac{\partial \overline{u}_j}{\partial x_i}\right). \tag{2.10}$$

The eddy viscosity of the residual motion ν_r, is modelled according to

$$\nu_r = (C_s\lambda)^2\ \overline{S}, \tag{2.11}$$

where $\overline{S} = \sqrt{2\overline{S}_{ij}\overline{S}_{ij}}$. Assuming that in a stationary state the production of SFS TKE equals dissipation, and applying the Kolmogorov spectrum, a theoretical value of 0.17 for the Smagorinsky constant C_s can be obtained (e.g. Pope, 2000).

The assumption above that all the SFS energy is eventually dissipated, may in some situations be inaccurate, since interactions between unresolved eddies can produce TKE on the resolved scale. Brown *et al.* (1994), and later Beare and MacVean (2004), incorporated this interaction by using stochastic backscatter, which allows energy to be cascaded from small to larger scales.

The dynamic Smagorinsky model presents another improvement. The classical Smagorinsky model depends on the 'global constant' C_s, i.e. it attains the same value everywhere. Germano *et al.* (1991) proposed using a 'local' C_s by first running the model with a test filter, determining the best value for C_s, and then rerunning the model.

In previous studies, the Smagorinsky with backscatter and the dynamic Smagorinsky models have shown improved performance with respect to the classical Smagorinsky model. For example, Beare *et al.* (2006) found that the latter model damps the turbulence compared to the refined models, which in the GABLS case lead to a lowering of the boundary layer height. However, they also found that the refinements to the SFS model do not play an important role if the numerical resolution is sufficiently high.

In this study, we adopt a frequently used alternative to the Smagorinsky model, namely the so-called TKE model, which was first introduced by Lilly (1968). The residual stress tensor and the SFS heat flux are modelled according to

$$\tau_{ij}^{\mathrm{SFS}} = -2K_m^{\mathrm{SFS}}\overline{S}_{ij}, \quad \text{and} \tag{2.12}$$

$$\tau_{\theta j}^{\mathrm{SFS}} = -K_h^{\mathrm{SFS}}\frac{\partial \overline{\theta}}{\partial x_j}. \tag{2.13}$$

The expression for the residual stress is similar to its counterpart in the Smagorinsky model, except the eddy viscosity or turbulence exchange coefficient is defined differently. The SFS exchange coefficients of momentum and heat are modelled as, respectively

$$K_{m,h}^{\mathrm{SFS}} = c_{m,h}\lambda\sqrt{\overline{e'}}, \tag{2.14}$$

where $c_{m,h}$ are constants (values are discussed below). The turbulence exchange coefficients are thus functions of the SFS TKE, which depends on the flow. In contrast to the Smagorinsky model, the TKE model permits the SFS TKE to vary in time, and the buoyancy term is retained. The prognostic equation for the filtered SFS TKE is modelled as

$$\begin{aligned}\frac{\partial \overline{e'}}{\partial t} &= \overbrace{-\overline{u}_j \frac{\partial \overline{e'}}{\partial x_j}}^{\text{Advection}} + \overbrace{K_m^{\text{SFS}} \frac{\partial \overline{u}_i}{\partial x_j}\left(\frac{\partial \overline{u}_i}{\partial x_j} + \frac{\partial \overline{u}_j}{\partial x_i}\right)}^{\text{Shear}} \\ &- \underbrace{K_h^{\text{SFS}} \frac{g}{T_0}\frac{\partial \overline{\theta}}{\partial z}}_{\text{Buoyancy}} + \underbrace{\frac{\partial}{\partial x_j} K_m^{\text{SFS}} \frac{\partial \overline{e'}}{\partial x_j}}_{\text{Transport}} - \underbrace{c_\epsilon \frac{\overline{e'}^{3/2}}{\lambda}}_{\text{Dissipation}} ,\end{aligned} \tag{2.15}$$

where c_ϵ is a constant, and its value is derived from turbulence theory[4]: $c_\epsilon = \pi(3C_k/2)^{-3/2} = 0.93$ where $C_k = 1.5$ is the Kolmogorov constant. As we shall see below, in numerical modelling, adjustments to the value of c_ϵ are sometimes made.

The last constants to be discussed are $c_{m,h}$. The theoretical value for c_m is $c_\epsilon \pi^{-2} = 0.094$. In order to find a value for c_h, we turn to the Prandtl number, which is the ratio of the turbulence exchange coefficient of momentum to heat. Observations have shown that in the weakly SBL, the Prandtl number is close to unity (e.g. Grachev *et al.*, 2007, and references herein). Although these observations are of turbulent eddies whose integral length scales (see next section) may be much larger than the filter, we assume that this value can be applied to the SFS model, i.e. $c_h = c_m$. This issue is in Section 3.4 discussed more thoroughly with respect to LES of katabatic flows.

2.3.3 Length scales

In the previous sections we discussed large and small eddies with respect to an integral length scale and a filter width. These length scales, however, were not properly introduced. In this section we therefore address the length scales relevant to LES more thoroughly.

The integral length scale of an eddy can be defined as the integral of the autocorrelation of the fluid velocity. The longitudinal autocorrelation of the x-component of the fluid velocity, u, at two locations $\vec{x}$ and $\vec{x} + \vec{r}$ in isotropic turbulence is

$$f(r) = \frac{\langle u(\vec{x})u(\vec{x}+\vec{r})\rangle}{\langle u^2\rangle}.$$

[4] A sharp spectral filter is assumed with cut-off wave number $\kappa_c = \pi/\lambda$.

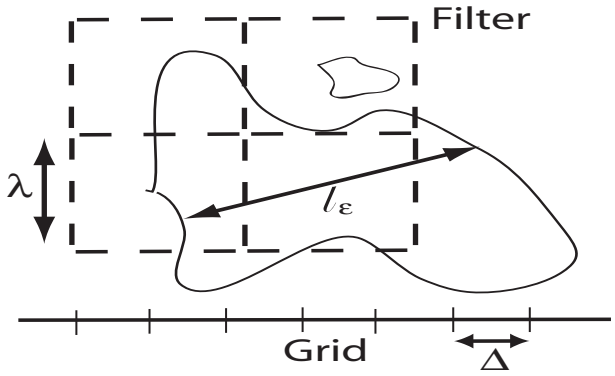

Figure 2.1. Sketch of an unresolved and a resolved eddy. The characteristic length of the turbulent flow is denoted by l_ϵ. The figure also shows the filter width λ, and the numerical resolution Δ.

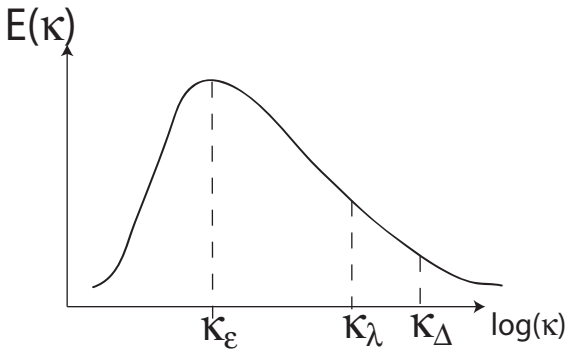

Figure 2.2. Sketch of the energy spectrum. The most energetic eddies have wavenumber κ_ϵ. The filter width, which has wave number κ_λ, is within the inertial subrange. The numerical resolution should not influence the results, hence the grid distance should be smaller than the filter width, i.e. $\kappa_\Delta > \kappa_\lambda$.

Here the brackets $\langle\cdot\rangle$ denote an ensemble average. The corresponding integral length scale, l_u, is given by

$$l_u = \int_0^\infty f(r)dr.$$

The integral length scale is often simply called the turbulence length scale. The TKE at this scale will cascade down to smaller scales where it is eventually dissipated. We therefore label the characteristic length scale by l_ϵ.
Figures 2.1 and 2.2 sketch the different length scales used in LES. The former figure shows a large eddy with integral length scale l_ϵ. The large eddy can be resolved with the chosen filter width λ (dashed line). In the figure is also shown a small (unresolved) eddy whose length scale is smaller than λ. The third length scale shown is the grid distance Δ, which ideally should be smaller than the filter width. This is discussed in more details below.
In Figure 2.2, the three length scales are related to the energy spectrum. The wave number corresponding to the eddy integral length scale is κ_ϵ, which is the wavenumber where the energy spectrum has its maximum. Filtering takes place at wave number κ_λ, which should lie in the inertial subrange, to the right of the spectral maximum. At this point we must stress that we use different definitions for turbulent length scales and filter widths. For instance, for a given Brunt-Väisälä frequencey $N^2 = \frac{g}{T_0}\frac{\partial\overline{\theta}}{\partial z}$, $l_b \equiv w/N$ is a turbulence length scale related to vertical displacement of air parcels in a stably stratified ambient atmosphere, whereas $\lambda_b \propto \sqrt{\overline{e'}}/N$ is a frequently used filter width.
The filter choice may depend on the application at hand. To illustrate this, regard the LES output of the CBL simulation (no background wind) according to Jonker *et al.* (1999). Figure 2.3(a) shows contour plots of the xz-cross section of instantaneous $\overline{u}$ and $\overline{w}$ fields. In the simulated CBL, the $\overline{u}$ field is less structured than the $\overline{w}$ field, which shows clear convective plumes. It is therefore logical to relate the filter width to the buoyancy. In the SBL however, convection is suppressed, and turbulence is maintained by wind shear. This is illustrated in Figure 2.3(b), which shows a simulation of the SBL. The data are from case WU128, see description in Section 2.4.2. Whereas the $\overline{w}$ field shows no clear structure, the $\overline{u}$ field reveals a layered structure in the vertical direction. This layered structure indicates a strong presence of wind shear, hence deriving a length scale based on the shear seems plausible.
A justification for relating the turbulent length scale to the shear is given by Hunt *et al.* (1988), who analysed laboratory experiments of a stably stratified fluid, and *hypothesized* that the dissipation length scale can be modelled as

$$l_\epsilon^{-1} \equiv c_\epsilon l^{-1} = \underbrace{D_w/z}_{l_w^{-1}} + \underbrace{D_s\frac{\partial\langle u\rangle}{\partial z}/w'}_{l_s^{-1}}, \tag{2.16}$$

where $\langle u\rangle$ is the ensemble averaged velocity, w' is the root mean square of vertical velocity fluctuations, and D_w and D_s are dimensionless coefficients determining the relative magnitude of 'blocking' by, respectively, the wall and shear effects. Due to shear the eddies can be squeezed and the length scale is reduced, especially when the vertical gradients of velocity is large. Hunt *et al.* (1988) argued that a buoyancy related length scale l_b, is of less importance.

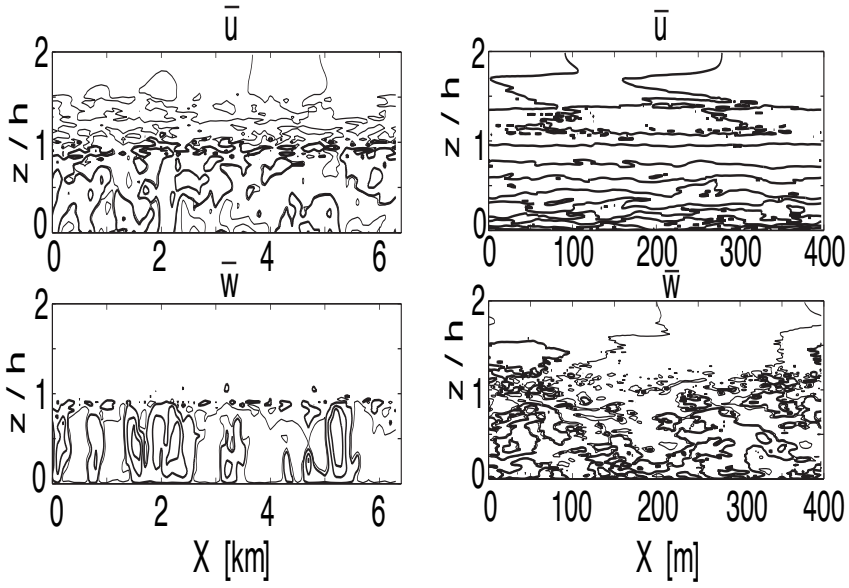

(a) CBL (b) SBL

Figure 2.3. Cross sections of the horizontal (top) and vertical (bottom) velocity fields. (a) CBL, contours of 0.5 ms^{-1} are shown, thin lines are negative velocities and thick lines positive velocities. The LES simulation is according to Jonker *et al.* (1999). (b) SBL with contour interval in upper panel being 1 ms^{-1}, and 0.5 ms^{-1} in the lower panel. Data taken from simulation WU128, see section 2.4.2 and Table 2.1.

Relation between filter width and numerical resolution

As mentioned above, the filter width should be smaller than the characteristic length scale, i.e. $\lambda < l_\epsilon$. In the neutral ABL, the characteristic size of the eddies depends only on the height z, and if we also impose the criteria that λ should be in the inertial subrange, then we have $\lambda \ll l_\epsilon(z)$. In practice, this condition is always violated close to the surface. If we disregard regions dominated by small eddies, which cover less than, say 10%, of the domain, we can define a length scale $l_{\epsilon D}$, such that $l_{\epsilon D} < l_\epsilon(z)$ in 90% of the domain. The requirement for the filter width then reads:

$$\lambda \ll l_{\epsilon D}. \tag{2.17}$$

A second requirement that should be satisfied in LES is that the results should be independent of resolution, which can only be fulfilled if $\lambda > \Delta$. Combined with Equation (2.17), the second requirement reads:

$$\Delta < \lambda \ll l_{\epsilon D}. \tag{2.18}$$

Computational costs are a limiting factor when simulating the ABL. In the bulk of the CBL, the characteristic length scale is of the order of the boundary layer depth h, which is much larger than Δ. Compared to the CBL, the characteristic length scales in the SBL are much smaller. Choosing a smaller domain is frequently not an option since some characteristics of the SBL would then not be contained within the numerical domain. Not changing the resolution implies that $l_{\epsilon D}$ approaches Δ, and the requirement (2.18) is no longer fulfilled.
If $\Delta \sim l_{\epsilon D}$, the filter width must be close to the numerical resolution (see Equation 2.18). Only a small fraction of the turbulence energy will be resolved, and the SFS parameterization becomes paramount. One way of solving this problem is to choose $\lambda < \Delta$. However, this approach is conceptually incorrect. A consequence of this ill-chosen solution is that numerical dissipation becomes important, see the next section.
If $\Delta < l_{\epsilon D}$, we are able to choose $\lambda < l_{\epsilon D}$ and the SFS contribution becomes smaller. The filter width λ, however, may not be in the inertial subrange, which makes the values of some constants (based on the -5/3 behaviour of the energy spectrum) debatable.

2.3.4 Numerical diffusion

Glendening and Haack (2001) studied the influence of different advection schemes on the LES results of a CBL with a relatively strong mean wind. They showed that both second- and fourth-order differencing of the advection term produce numerical dissipation of especially small eddies. The energy loss is due to inaccuracies introduced by discrete differencing in the presence of a mean wind. In this study, the geostrophic forcing of $8\,\mathrm{ms}^{-1}$ (see the next section) will introduce non-vanishing inaccuracies in the discrete differencing, and hence also significant numerical errors.
Here we use a second-order central-differences scheme (see Section 2.4.1), hence the numerical results are second-order accurate in the grid distance Δ. In section 2.5, we present some plots of the TKE budgets. The residual term in these budgets, which results from these numerical errors, is in most cases significant, and in one case where we have artificially reduced the eddy viscosity, it is the dominant term. For instance, in our model the numerical error ε_i^n in the advection term $\frac{\partial \overline{u}_i \overline{u}_j}{\partial x_j}$ in Equation (2.5), is given by

$$\varepsilon_i^n = \Delta^2 \mathcal{A}_i, \tag{2.19}$$

where $\mathcal{A}_i$ is a complex term containing first and second-order derivatives of the velocity field[5]. If we compare this for simplicity with the Smagorinsky model

[5]It should be noted that the Asselin filter, which is applied to the leap-frog time integration of the advection term (see Section 2.4.1), also contributes to numerical diffusion.

for the divergence of the eddy stresses, we have

$$\frac{\partial}{\partial x_j}\tau_{ij}^{\mathrm{SFS}} = -\Delta^2\ 2(C_s)^2\frac{\partial}{\partial x_j}(\overline{S}\ \overline{S}_{ij}) = -\Delta^2\mathcal{B}_i, \tag{2.20}$$

where we have taken the filter scale equal to Δ. We observe from Equations (2.19) and (2.20) that the numerical error and the residual stress divergence have the same order in Δ, and that both coefficients $\mathcal{A}_i$ and $\mathcal{B}_i$ consist of velocity derivatives. It appears that when $\lambda = \Delta$, the magnitude of the numerical error is of the same order as that of the modelled dissipation.
The numerical error is not purely diffusive. Let us turn to the TKE equation of the *resolved motions*, $\overline{E} = \frac{1}{2}\overline{u}_i\ \overline{u}_i$.[6] From Equation (2.5) we get for a horizontally homogeneous field

$$\frac{\partial\overline{E}}{\partial t} = -\frac{\partial\overline{\pi}\ \overline{u}_3}{\partial x_3} + \frac{\partial\overline{u}_3\overline{E}}{\partial x_3} + g\frac{\overline{\theta}-\Theta_a}{\theta_0}\overline{u}_3 - \overline{u}_3\ \overline{u}_i\frac{\partial\overline{u}_i}{\partial x_3} - \overline{u}_i\frac{\partial\tau_{ij}^{\mathrm{SFS}}}{\partial x_j}. \tag{2.21}$$

The terms on the right hand side are (from left to right): pressure redistribution, transport, buoyancy, shear and dissipation, respectively. Note that the advection term in (2.5) has been divided into a transport term and a shear term. The last term in the equation originates form the eddy stress, and can be rewritten as a divergence term (contributing to the internal transport) and a pure dissipation term, which is always smaller or equal to zero. By filling in (2.12) - (2.13) and (2.10) in the last term of (2.21), one gets

$$\overline{u}_i\frac{\partial\tau_{ij}^{\mathrm{SFS}}}{\partial x_j} = -\frac{\partial}{\partial x_j}\left[\overline{u}_i K_m^{\mathrm{SFS}}\Big(\frac{\partial\overline{u}_i}{\partial x_j}+\frac{\partial\overline{u}_j}{\partial x_i}\Big)\right] + \frac{1}{2}K_m^{\mathrm{SFS}}\left[\frac{\partial\overline{u}_i}{\partial x_j}+\frac{\partial\overline{u}_j}{\partial x_i}\right]^2, \tag{2.22}$$

where the last term is strictly positive or zero. The 'numerical dissipation', however, equals $\Delta^2\overline{u}_i\mathcal{A}_i$, and can be positive or negative. This term can therefore also have a destabilizing effect on the flow ('backscatter'). We conclude that for an accurate use of second-order schemes, the filter scale must be chosen (much) larger than Δ.

2.4 The numerical model and simulation set-up

2.4.1 DALES

This study uses version 2.0 of the Dutch atmospheric LES (DALES). In this numerical model, the filtered prognostic equations for momentum, thermodynamic energy and SFS TKE, e.g. Equations (2.5), (2.6) and (2.15) respectively, are obtained by applying a sharp spectral filter. The equations are solved numerically on an Arakawa C-grid, e.g. the $\overline{u}$ and $\overline{v}$ components

[6] In the numerical code, we evaluate $\left\langle\frac{1}{2}\overline{u}_i\ \overline{u}_i - \frac{1}{2}\langle\overline{u}_i\ \overline{u}_i\rangle\right\rangle$ in order to remove the energy of the mean background flow.

of the filtered velocity vector are calculated on the sides of the (staggered) rectangular grid, and $\overline{w}$ at the bottom. The pressure, the SFS TKE, and the closure coefficients (e.g. Equation 2.14) are calculated at the center of the grid.
For boundary conditions, we prescribe the rate of decrease of the surface potential temperature (value given below), and in the wall layer, e.g. between the solid surface and the first model layer, we use standard Monin-Obukhov (MO) theory (e.g. Foken, 2006) to determine the vertical gradients of velocity and temperature. Recent literature has raised concerns regarding the use of MO theory for the (very) SBL, this issue is commented upon in the next chapter. At the other end of the vertical domain, a sponge layer filling the top 25 per cent of the grid, filters out fluctuations of velocity and temperature, and dissipates gravity waves. Lastly, in the horizontal directions we apply cyclic boundary conditions.
The advection terms are spatially discretized using a second-order scheme. The time integration of the advection terms is performed using the leap-frog method with an Asselin filter (1972) to avoid time splitting, and the diffusion terms are calculated separately using an Euler forward scheme. The Poisson equation is solved using a fast-Fourier transform in the horizontal directions, and a finite difference technique in the vertical direction.

2.4.2 Case description

In the LES intercomparison described in Beare *et al.* (2006), a weakly SBL was simulated. The study focussed on the effects of the resolution and the SFS model on the first- and second-order statistics. Here we use the same simulation set-up and compare our results to those of the GABLS participants. In Beare *et al.* (2006), an extensive description of the simulation set-up is given, a short description is presented below.
The initial potential temperature profile consists of a mixed layer with a temperature of 265 K reaching up to 100 m, with an overlaying temperature inversion with strength $0.01\,\mathrm{Km}^{-1}$. At the surface, a temperature decrease is prescribed as -0.25 Kh^{-1}, which ensures that the boundary layer becomes stably stratified. The surface cooling is applied for 9 hours. At start-up of the simulation, the production of turbulence is stimulated by randomly perturbing the potential temperature field up to 50 m with a maximum amplitude of 0.1 K. The simulation furthermore requires an initial SFS TKE, $\overline{e'}$, which is prescribed according to $0.4(1 - z/250)^3\,\mathrm{m}^2\mathrm{s}^{-2}$ below a height of 250 m, and zero aloft. After initialization, turbulence is maintained by shear production; the system is forced by a geostrophic wind of $8\,\mathrm{ms}^{-1}$. Finally, the domain size is 400 m in all three spatial directions, and we have used a uniform grid, i.e. $\Delta_x = \Delta_y = \Delta_z = \Delta$.

In the *resolution study* we use three different numerical resolutions: 12.5, 6.25, and 3.125 m. The corresponding numbers of grid points (in each spatial direction) are 32, 64, and 128, respectively. For each resolution we perform two simulations, which differ in the filter width definition. Each simulation is assigned a label containing the acronym of the code's origin (or special feature) followed by the number of grid points. For example, the simulation WU128 uses the filter width definition utilized by Wageningen University (one of the participants in the GABLS intercomparison study) at a resolution of 3.125 m (128 grid points). Their model admits two filter width definitions, the first being

$$\lambda_{WU} = \min\left(\Delta, \lambda_b\right) \quad \text{with} \quad \lambda_b = A_b \sqrt{\frac{\overline{e'}}{|N^2|}}, \tag{2.23}$$

where $A_b = 0.76$ is a dimensionless constant, and the second option is to set the filter width equal to the grid distance, e.g.

$$\lambda_{WUD} = \Delta. \tag{2.24}$$

The filter parameterization (2.23) follows from Deardorff (1980). In order to prevent laminarization he altered the SFS TKE dissipation rate by including a height dependency in the dissipation constant c_ϵ. Following his approach, we here modify c_ϵ in the lowest 50 m of the vertical domain:

$$c_\epsilon(z) = \left(1 + 2.9 \max\left[1 - z/50, 0\right]\right)\left(0.19 + 0.51\lambda/\Delta\right). \tag{2.25}$$

In the *filter width study*, we test four filter width definitions using the finest numerical resolution (3.125 m). All simulation labels thus end on '128'. In addition to WU128, we adopt one filter from literature. Following Hunt *et al.* (1988) we use in simulation H128

$$\lambda_H = \begin{cases} \min\left(\Delta, \left[\lambda_s^{-1} + \lambda_w^{-1}\right]^{-1}\right) & \frac{\mathrm{d}\overline{\theta}}{\mathrm{d}z} > 0 \\ \min\left(\Delta, \lambda_w\right) & \text{otherwise,} \end{cases} \tag{2.26}$$

where

$$\lambda_s = A_s \left[\overline{e'} \Big/ \left(\frac{\partial \overline{u}_i}{\partial x_j} + \frac{\partial \overline{u}_j}{\partial x_i}\right)^2\right]^{1/2} \quad \text{and} \quad \lambda_w = A_w z,$$

with $A_s = 3.7$ and $A_w = 2.0$ being dimensionless constants. We use a dissipation constant that follows from theoretical considerations: $c_\epsilon = 0.93$ (see also Section 2.3.2).

Table 2.1. Summary of simulations. Each simulation has a label derived from the code's origin / special feature, which in each row is underlined. The number of grid points (in each spatial direction) is also given in the simulation label. Note that all simulations use a uniform grid. Several definitions of the filter width λ are used. A short summary of these definitions and their equation numbers are given. Some simulations use a special formulation for the SFS TKE dissipation constant c_ϵ, which is given in Equation (2.25).

Label	Origin	Grid points	Num res [m]	Filter width (λ)	Equation	c_ϵ	Remark
		Model resolution study (Results in Section 2.5.1)					
WU32		32	12.5	$\min(\Delta, \lambda_b)$	(2.23)	$c_{\epsilon(z)}$	
WUD32		32	12.5	Δ	(2.24)	$c_{\epsilon(z)}$	
WU64	Wageningen	64	6.25	$\min(\Delta, \lambda_b)$	(2.23)	$c_{\epsilon(z)}$	
WUD64	University	64	6.25	Δ	(2.24)	$c_{\epsilon(z)}$	
WU 128		128	3.125	$\min(\Delta, \lambda_b)$	(2.23)	$c_{\epsilon(z)}$	
WUD128		128	3.125	Δ	(2.24)	$c_{\epsilon(z)}$	
		Filter parameterization study (Results in Section 2.5.2)					
WU 128	Wageningen	128	3.125	$\min(\Delta, \lambda_b)$	(2.23)	$c_{\epsilon(z)}$	
WUD128	University	128	3.125	Δ	(2.24)	$c_{\epsilon(z)}$	
H128	Hunt *et al* (1988)	128	3.125	$\min(\Delta, \lambda_H)$	(2.26)	0.93	
CST128	This thesis	128	3.125				$K_{m,h}^{\mathrm{SFS}} = \underline{\mathrm{cst}}$ $= 0.01\,\mathrm{m^2 s^{-1}}$
COMP128	This thesis	128	3.125	$\min(\alpha z, 2\Delta)$	(2.27)	0.93	Compound filter

The remaining two filters have to our knowledge not been used before. In CST128 we bypass the evaluation of the exchange coefficients of momentum and heat by prescribing their values:

$$K_{m,h}^{\mathrm{SFS}} = 0.01\mathrm{m}^2\mathrm{s}^{-1}.$$

By choosing small values for the exchange coefficients, we effectively 'switch off' the SFS model, and consequently there is no meaningful filter in simulation CST128.
The last filter width definition is conceptually correct (e.g. $\lambda > \Delta$) in the bulk of the boundary layer. In COMP128 we *a priori* define a compound profile for λ:

$$\lambda_{COMP} = \min(\alpha z, 2\Delta), \tag{2.27}$$

where $\alpha = 0.3125$ is a dimensionless constant that ensures a matching at 20 metres. Below 20 metres, e.g. in the lowest 10% of the boundary layer (a rough estimate), the filter width thus increases linearly with height, and in the remaining 90% of the boundary layer we use $\lambda = 2\Delta$. Note that below 10 m, $\lambda < \Delta$, which was necessary to prevent laminarization. The SFS TKE dissipation constant is $c_\epsilon = 0.93$.
Table 2.1 presents a summary of all simulations and their numerical resolutions, filter width definitions, and SFS TKE dissipation constants c_ϵ.

2.5 Results

We now investigate the influence of resolution, filter parameterization, and numerical dissipation on the model output. All results are horizontally averaged and time averaged over the ninth hour. The data from the intercomparison study are shown as shaded areas. The latter data have been obtained from `www.gabls.org`, and we only show their 3.125 m resolution results.

2.5.1 Model resolution

A problem arising when simulating the SBL, is that the resolution has to be sufficiently high to resolve the smaller scales of the 'stable turbulence'. Beare *et al.* (2006) reported that some models experienced laminarization when using coarse resolutions. With laminarization we mean that the resolved velocities, fluxes, etc tend to zero (or remain zero) and that the SFS part fully describes the dynamics of the simulation. A measure for the respective contributions of the SFS and resolved-scale dynamics is the ratio of the SFS TKE to the total TKE. This ratio is plotted in Figure 2.4. The vertical axis displays the height, normalized by the boundary layer depth, which was computed according to (Kosović and Curry, 2000)

$$h = \frac{z(\tau = 0.05u_*^2)}{0.95}. \tag{2.28}$$

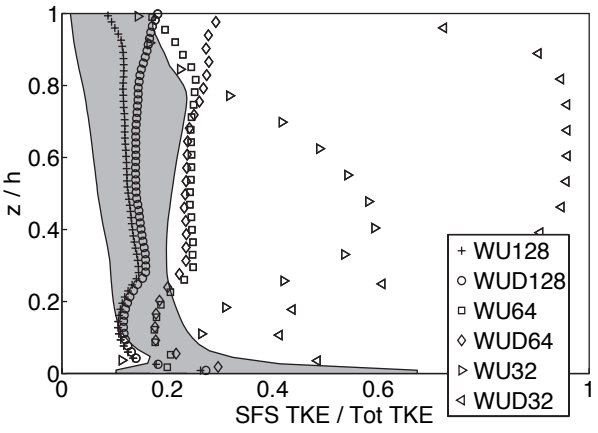

Figure 2.4. Ratio of the SFS TKE to the total TKE versus height normalized by the boundary layer depth h. The shaded area indicates the Beare *et al.* (2006) results.

Here $\tau \equiv \left[\overline{uw}^2 + \overline{vw}^2\right]^{1/2}$ is the total stress (i.e. resolved plus SFS contribution), and u_* the surface friction velocity. Simulation WU32 shows that the ratio of SFS TKE to total TKE is larger than 0.5 in the mid of the boundary layer, whereas WUD32 exceeds a ratio of 0.5 for all $z/h \gtrsim 0.25$. The fact that the SFS TKE is only a small fraction of the total TKE near the surface, is a consequence of the SFS TKE dissipation formulation (2.25).
Figure 2.4 also shows the SFS to total TKE ratio for the 64 and 128 grid points simulations. The former is an intermediate resolution, yet the 64 grid point simulations yield a ratio of approximately 0.25 in the bulk of the boundary layer, which is considerably smaller compared to WU(D)32. In the gross part of the boundary layer, only small differences between the WU64 and WUD64 simulations are noted. This implies that in the bulk of the boundary layer, the filter width λ_{WU} (2.23) is equal to the grid distance Δ. Lastly, the finest resolution (WU128 and WUD128) produces in the interior of the boundary layer a ratio of approximately 0.15. In our point of view, the upper limit of the ratio should be less than 40%, whereas the lower limit is determined by the computational costs.
To further study the influence of resolution, we show the energy spectra of the $\overline{w}$-component of the resolved velocity for WUD128, WUD64, WUD32 and WU32, Figure 2.5. The spectra for WU64 and WU128 are very similar to WUD64 and WUD128, respectively, and are therefore not plotted. The spectra are computed from a single instantaneous field in the xy-plane at 75 m ($\sim h/2$) after 9 hours of simulation.
The energy spectrum of three-dimensional, homogeneous turbulence should

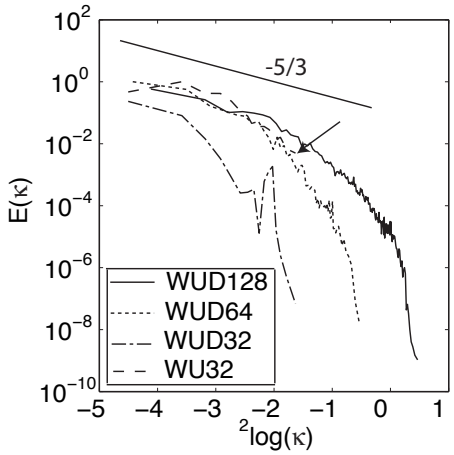

Figure 2.5. The energy spectrum of the $\overline{w}$-component for WUD128, WUD64 and WU(D)32. The straight solid line indicates $\kappa^{-5/3}$, arrow marks the end of the WU32 spectrum.

show a dissipation range. Such a dissipation range is seen for simulations WUD64 and WUD128. For the coarsest resolution, however, the picture is different. Firstly, the energy spectra for the simulations WUD32 and WU32 do not coincide. Consequently, at this resolution the buoyancy effect, which is included in the filter definition λ_{WU}, becomes important. Secondly, simulation WUD32 shows in the dissipation range a local maximum at ${}^2\log(\kappa) = -2$. This local maximum is likely caused by numerical diffusion. On the other hand, simulation WU32 does not show a clear dissipation range. The end of the WU32 energy spectrum is marked by an arrow. Based on the last two figures, we conclude that the 12.5 m resolution does not resolve much of the turbulence in this particular SBL, and will therefore not consider these simulations in the remainder of this chapter.

We conclude this section by showing the profiles of the wind speed $S = \left[\overline{u}^2 + \overline{v}^2\right]^{1/2}$ and potential temperature of WUD128 and WUD64. Simulations WU128 and WU64 give similar results and are therefore not plotted. The horizontal wind profiles, plotted in Figure 2.6(a), both show a low-level jet (LLJ), with a super-geostrophic wind speed, which is a characteristic of a geostrophically forced SBL. The profiles furthermore compare well with the results from the intercomparison study. The latter results (shaded area) show two maxima, and from the GABLS data set it is noted that half of the participating models have their LLJ at the first maximum, and one half have the LLJ at the second maximum.

The simulated potential temperature profiles are plotted in Figure 2.6(b). The

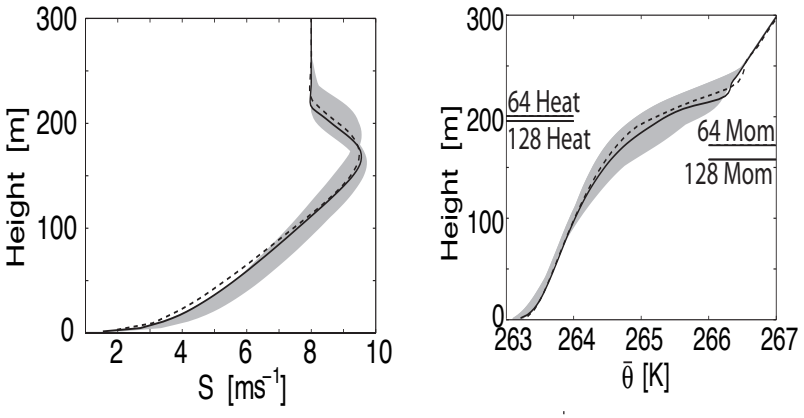

(a) Wind speed (b) Potential temperature

Figure 2.6. Wind speed (a), and potential temperature (b) for grid resolution of 3.125 m (solid) and 6.25 m (dashed). The latter figure also shows the boundary layer depth. The horizontal lines on the left indicate h based on the heat flux (see Equation 2.29), and on the right using the momentum flux (e.g. 2.28).

profiles coincide up to ≈ 150 m, whereas some small differences are noted further aloft. These differences, however, are much smaller compared to the range of the GABLS results.

There are different options to estimate the boundary layer depth h. Kosović and Curry (2000) calculated h as the height were the momentum fluxes go to zero, see Equation (2.28). Alternatively, we can define the top of the boundary layer to be the height at which the heat flux goes to zero, i.e.

$$\tilde{h} = \frac{z(F = 0.05F_s)}{0.95}, \tag{2.29}$$

where F is the *total* heat flux, and F_s is its surface value. Kosović and Curry (2000) argued against using the heat flux as a parameter for determining h, since the heat flux is often dominated by the effects of gravity waves near the stable ABL top. When determining the boundary layer depth from (2.28), h is found to be near the height of the wind maximum, e.g. Figure 2.6. However, the wind profile above this level is not yet adjusted to the geostrophic wind. Moreover, Figure 2.6(b) shows that the boundary layer heigt determined by the momentum flux falls below the height of the temperature inversion. On the other hand, the boundary layer depth derived from (2.29) better points out the locus of the temperature inversion, and is closer to the height at which the

free atmosphere no longer influences the boundary layer.

2.5.2 Filter width parameterization

In the LES intercomparison study, Beare *et al.* (2006) found that the differences in model results at a moderate resolution (3 - 6 m) could to a substantial degree be ascribed to the differences between the SFS models. Although we cannot change the SFS model itself, we will here present results obtained by using different filter parameterizations. These parameterizations are summarized in Table 2.1. We choose to only look at the simulations using a 3.125 m (128 gridpoints) resolution.
The first question that arises when simulating the SBL, is how stable the boundary layer really is. Figure 2.7(a) shows the non-dimensional stability parameter $\zeta = z/\Lambda$ versus the normalized height z/h. Here Λ is the local Obukhov length, which is given by (e.g. Nieuwstadt, 1984)

$$\Lambda = -\frac{\tau^{3/2}}{\kappa(g/T_0)F},$$

with $\kappa = 0.4$ being the von Karman constant. The figure shows that all profiles coincide below $z/h \sim 0.25$. For larger z/h, COMP128 is the most stable case whereas CST128 is the least stable. The stability profiles of WU128 and H128 vitually coincide at all heights. Near the inversion, the stability parameter is $\zeta \approx 8$. Below we will use this value as the upper limit for ζ when inspecting the normalized standard variances of velocity and heat.
The results presented in Figure 2.7(a) should be interpreted carefully. The profiles of ζ as functions of z/h show that simulaton COMP128 produces the most stably stratified boundary layer. However, when plotting ζ versus z (not shown), the opposite picture emerges: simulation COMP128 yields the least stable stratification while CST128 produces the most stable stratification. The scale factor h therefore plays an important role in Figure 2.7(a). The inversion heights calculated using Equation (2.28) range from 144 (CST128) to 177 m (COMP128).

In the LES code used by Wageningen University (simulations with labels WU), the dissipation of SFS TKE near the surface was increased in order to prevent laminarization. This was primarily done for the coarser resolutions, but for the sake of consistency, we kept the formulation unchanged. The model's capability of resolving the turbulent motions is seen from Figure 2.7(b), which shows the relative SFS contribution to the total TKE. In contrast to the 12.5 m resolution (Figure 2.4), no simulation becomes laminar when the grid distance is 3.125 m. The filter width parameterization COMP128 produces the largest SFS contributions to the total TKE. CST128, on the other hand, by definition does not produce any SFS TKE.
Laminarization can also be detected by comparing the SFS heat flux to the total heat flux. Figure 2.7(c) shows the total and SFS heat fluxes as functions of

height. The total surface heat flux F_s ranges from -0.011 to -0.013 $\mathrm{K\,ms^{-1}}$. H128 produces a total heat flux and SFS contribution similar to WU128, whereas COMP128 produces the largest total heat flux and also the largest SFS contribution. As expected, with its small, constant exchange coefficients, CST128 produces only a very small SFS contribution to F.

The energy budgets of the *resolved motions* are also important when judging how a filter parameterization performs. As argued in Section 2.3.4, the numerical diffusion will only be small if $\lambda > \Delta$. Since it is desirable in our point of view (the alternative view is discussed in e.g. Boris *et al.*, 1992) to model the dissipation, (see last term in Equation 2.21) it is desirable to minimize the residual energy. In an equilibrium, the left hand side of Equation (2.21) vanishes, and thus the terms on the right hand side must be in balance. In our simulations they do not balance due to numerical errors, which was discussed in Section 2.3.4. We call the imbalance the residual.

Figure 2.8 shows the TKE budgets of the *resolved* motions. We focus on the largest terms, which are the the shear production of TKE, the modelled dissipation, and the residual TKE. The remaining terms (buoyancy, transport, pressure redistribution and time rate of change of TKE) are small, and thus only their sum is plotted.

All simulations show that the shear production of TKE is the largest source term. A secondary production term is also noted near the surface, and at a height of ~ 10 m. However, this secondary production, which is caused by the pressure redistribution and turbulent transport terms exceeding the buoyancy destruction, is small compared to the shear production term. The production of TKE is balanced by the modelled or numerical dissipation. The modelled dissipation of TKE depends on the turbulence exchange coefficients, see Equation (2.22). In simulation CST128, these exchange coefficients are small, and the modelled dissipation cannot balance the shear production, whereby TKE is removed through numerical dissipation. The TKE budget for CST128 shows that the residual term exceeds the modelled dissipation at all heights. To further investigate the numerical dissipation versus the modelled dissipation, we have calculated the ratio of the residual term to the modelled dissipation. Averaged over the lowest 100 m of the boundary layer, simulation CST128 produces a ratio of 175%. The remaining three simulations show a different picture, simulations WU128 and H128 produce the ratios 58 and 68 %, respectively. The final simulation, for which $\lambda > \Delta$ in the bulk of the boundary layer, yields a ratio of 33%. In the latter simulation, the filter width close to the surface ($\lesssim 10$ m) is smaller than the grid distance, which is why the residual term increases near the ground.

We conclude this subsection by displaying the wind and potential temperature profiles. Figure 2.9(a) shows that all wind profiles have approximately the same form. The wind maxima are practically the same, but the heights of the wind maxima differ somewhat. The largest difference in the wind maximum heights is ≈ 20 m. It is also noted that all simulations are in agreement with

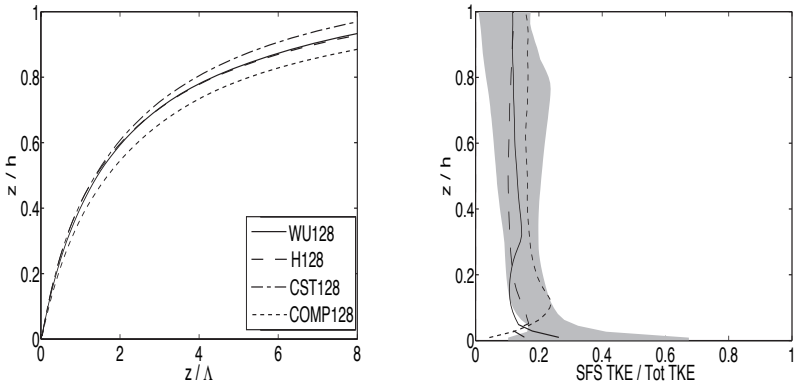

(a) Stability

(b) Heat flux

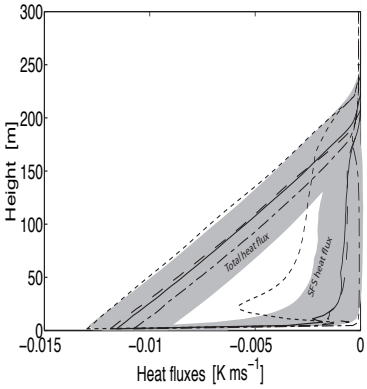

(c) Total and SFS heat fluxes

Figure 2.7. Stability parameter $\zeta = z/\Lambda$ (a), and ratio of SFS to total TKE (b) as functions of normalized height, whereas (c) shows the total and SFS heat fluxes as functions of height. The GABLS results with 3.125 m resolution are shown as shaded areas.

the GABLS results.

The difference in the wind maximum heights indicate that the simulations yield different values for the boundary layer height. This can also be deduced from Figure 2.9(b), which shows the potential temperature profiles. These profiles practically coincide up to $z \approx 150$ m, but thereafter they diverge, leading to different values for h. The largest difference is between the COMP128 and the CST128 simulations. Their results, however, are still in the range of the GABLS results.

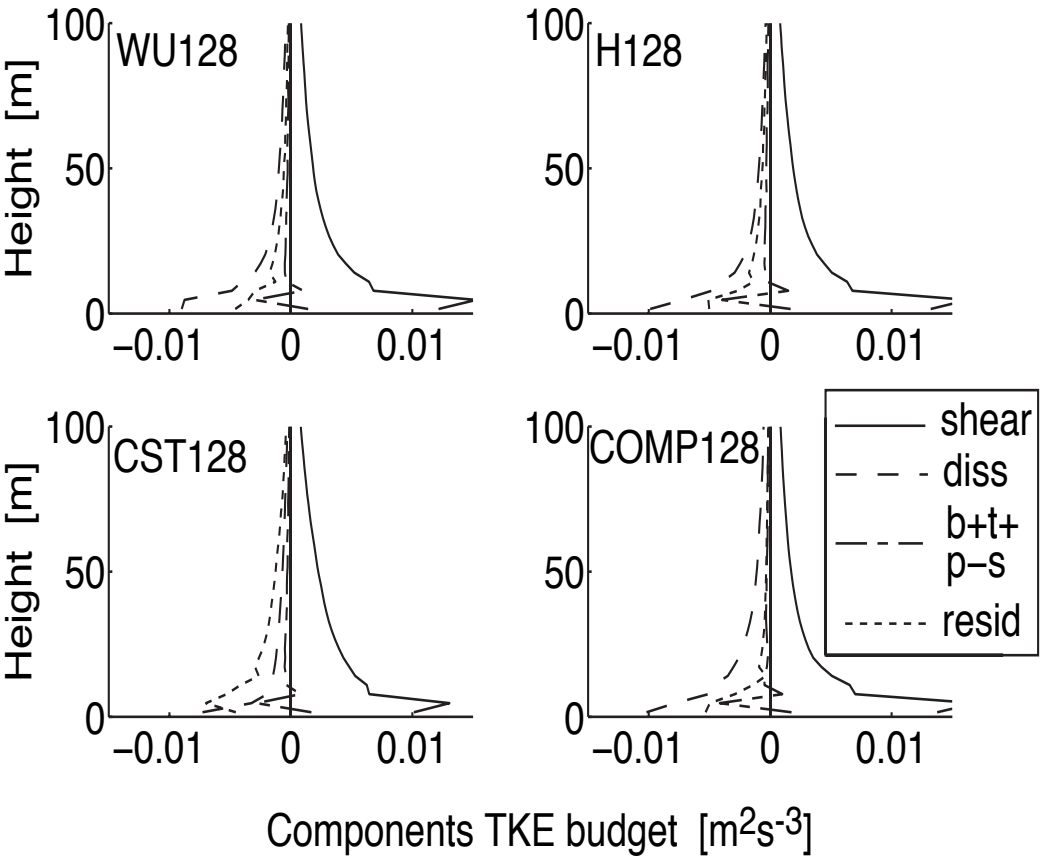

Figure 2.8. TKE budgets of the *resolved motions* as functions of filter parameterization. Only the largest terms are shown individually: shear production, dissipation and the residual term. The dotted line combines the remaining terms: buoyancy + transport + pressure redistribution - storage.

2.5.3 Comparison with observations

The results in the previous section indicate that our numerical model produces results in agreement with those of others. However, the results should also be in agreement with observations. Like Beare *et al.* (2006), we have compared our output with the observations compiled by Nieuwstadt (1984). A thorough discussion is given in Van Dop and Axelsen (2007), here we will only show the normalized standard deviations of the wind and temperature versus stability. Figure 2.10 shows our LES results of standard deviation of $\overline{u}$ and $\overline{v}$, (σ_u and

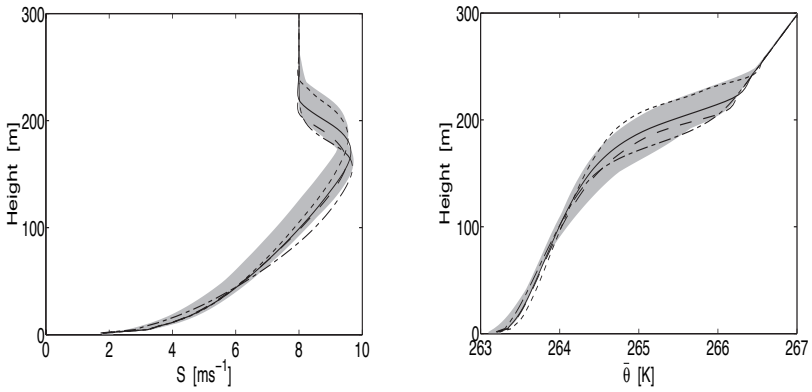

(a) Wind speed (b) Potential temperature

Figure 2.9. Wind speed (a), and potential temperature (b) as functions of height. Legend as in Figure 2.7, shaded area: GABLS.

σ_v, respectively) normalized by $\tau^{1/2}$ as functions of $\zeta = z/\Lambda$. The simulations suggest that $\sigma_u/\tau^{1/2}$ has an asymptotic value for large ζ. The average value of $\sigma_u/\tau^{1/2}$ over the interval $3 < \zeta < 8$ (limits are motivated below) is 2.25 whereas the observations by Nieuwstadt gave 2.0. On the other hand, the LES results of the normalized σ_v do not show any asymptotic value for large ζ, but rather increase with increasing ζ.

Figure 2.11 shows the normalized standard deviations of vertical velocity and potential temperature, $\sigma_w/\tau^{1/2}$ and $\sigma_\theta\tau^{1/2}/F$ respectively. The spread in Nieuwstadt's observations of normalized standard deviations are also shown. The LES results of the normalized σ_w are grouped closely together, and are seen to have an asymptotic limit of 1.43. The results are in agreement with the Nieuwstadt's observations, who found an asymptotic value of 1.4. The LES results of the normalized σ_θ, on the other hand, show notable differences between the simulations. Each simulation suggests that there is an asymptotic limit, but that these limits differ. The mean asymptotic value for $3 < \zeta < 8$ is 2.15, whereas Nieuwstadt's observations yield the the asymptotic limit 3.0.
We also compare the LES results to the results reported on in Basu *et al.* (2005), who compiled data of the normalized standard deviations from field observations, wind-tunnel experiments and LES studies. They divided the data into five classes depending on the stability parameter $\zeta = z/\Lambda$. Most LES results belonged to the class for which $\zeta > 3$. In Table 2.2 we have adopted their Table 3. Note that the values are medians of the normalized standard deviations. Basu *et al.* (2005) advocated using the median instead of the mean since outliers could strongly influence the mean value. Following this approach,

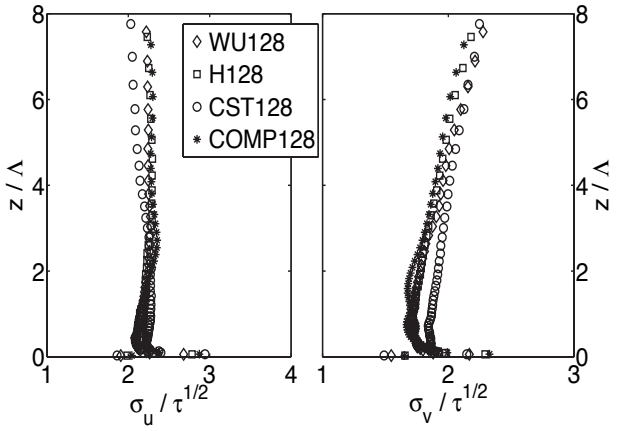

Figure 2.10. Standard deviations of $\overline{u}$ (left) and $\overline{v}$ (right) normalized by the stress. The results are from simulations using different filter parameterizations, and are averaged over the last hour of of the simulation.

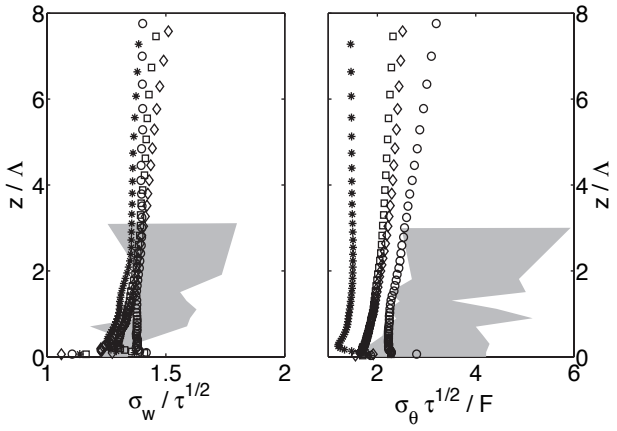

Figure 2.11. As in Figure 2.10 but for the normalized standard deviations of vertical velocity (left) and potential temperature (right). The shaded area indicates the standard deviations observed by Nieuwstadt (1984).

we have for each of our simulations determined the median of the normalized standard deviation, and subsequently averaged these medians. In our study the largest value for ζ is 8, hence the median values are based on results for which $3 < \zeta < 8$. Table 2.2 also includes the normalized standard deviations

Table 2.2. Column 2-4: Median of normalized standard deviations, adopted from Basu *et al.* (2005). Column 5: Our results: *Median* of the standard deviations averaged over all simulations. Column 6: Asymptotic values from Nieuwstadt's z-less scaling theory.

Turbulence statistics	Field observations	Wind tunnel	LES Basu *et al.*	LES	Nieuwstad
$\sigma_u/\tau^{1/2}$	2.7	2.5	2.3	2.23	2.0
$\sigma_v/\tau^{1/2}$	2.1	-	1.7	-	1.7
$\sigma_w/\tau^{1/2}$	1.6	1.5	1.4	1.40	1.4
$\sigma_\theta\tau^{1/2}/\lvert F\rvert$	2.4	2.7	2.4	2.20	3.0

predicted by Nieuwstadt's z-less scaling theory.
Our values for normalized σ_u and σ_w are in agreement with the LES values given by Basu *et al.* (2005). For the lateral velocity, however, we cannot compare the normalized σ_v to Basu *et al.* (2005) since our results show an increasing trend for large ζ. As noted above, the spread in our simulated profiles of normalized σ_θ is large. The medians vary from 1.5 to 2.8 and the averaged median is 2.20.
The field and wind tunnel observations from Basu *et al.* (2005) also qualitatively agree with our LES results. Their observations of normalized σ_u, σ_w, and σ_θ are somewhat larger than our results. However, the observed standard deviation of the potential temperature can only cautiously be compared to our LES results, which showed relatively large differences between the simulations.

2.6 Conclusion and discussion

We have briefly sketched the concept of LES, discussed the most commonly used SFS models, and given examples of successfully simulated convective and SBLs. In one recent LES study of the weakly SBL, Beare *et al.* (2006) performed an intercomparison of LES codes. The latter study has been the reference point of our research.
We have simulated the GABLS case using three different numerical resolutions, the grid distances being 12.5, 6.25 and 3.125 m, respectively.

- For the coarsest resolution, 12.5 m, we find:
  - The ratio of the SFS TKE to the total TKE is $\gtrsim 0.5$ in the bulk (mid) of the boundary layer, i.e. the SFS model is responsible for more than half of the total turbulence kinetic energy.
  - When the filter width equals the grid distance, $\lambda = \Delta$ (WUD32), the energy spectrum shows a local energy maximum in the dissipation

region. On the other hand, when permitting $\lambda < \Delta$ (WU32), the energy spectrum lacks a dissipation range.

- We conclude that the 12.5 m resolution does not resolve stable turbulence. If we *a priori* estimate values for u_* and the wind shear to be $0.2\,\mathrm{ms}^{-1}$ and $25\,\mathrm{s}^{-1}$ ($= 8\,\mathrm{ms}^{-1}/200$ m), respectively, the ratio $u_*/(du/dz) = 12.5\,\mathrm{m}$ gives a length scale of the turbulence. Certainly, the grid distance should be smaller than this value.

- For the 6.25 and 3.125 m resolutions we find:
  - The energy spectra have a dissipation range.
  - The mean profiles fall within the range of the GABLS results.
  - The estimate of the boundary layer height using the heat flux is larger compared to the estimate using the momentum flux.
- For the current weakly SBL, the numerical resolution should not exceed 6 m.

Using only the finest resolution, we have studied the effect of four filter parameterizations on the first- and second-order model results. One filter is conceptually correct (i.e. $\lambda \geq \Delta$) in the bulk of the boundary layer, while the other three filters allow for $\lambda < \Delta$. The findings are:

- The differences between the filters influence the mean profiles more than the numerical resolution.
- All simulations yield results that are in the range of the GABLS data.
- Inspection of the energy budgets shows that numerical diffusion becomes important when $\lambda < \Delta$. In principle, a filter width $\lambda > \Delta$ is required.

There is only a limited amount of observational data of the SBL, which makes it difficult to validate the LES study of the SBL. We have compared our results with the observations by Nieuwstadt (1984), which contained much scatter, and the experimental and LES results by Basu *et al.* (2005). We find:

- The agreement with measurements is satisfactory, though there is no strong evidence for z-less scaling.
- Due to the large scatter in the observations (Van Dop and Axelsen, 2007), we cannot decide which SFS parameterization is to be preferred.

One difficulty in performing LES studies of the (weakly) SBL, is that the characteristic length scale of the turbulence is small, requiring a fine numerical mesh. Even with a fine numerical grid, some models use a filter that is smaller than the grid distance if the flow is locally very stable. As a consequence hereof, numerical errors are introduced, which are furthermore responsible for

a numerical dissipation of TKE. The TKE budgets presented here (Figure 2.8) have revealed that the numerical dissipation of TKE becomes substantial if $\lambda < \Delta$. We therefore recommend using a filter that is larger or at least equal to the grid distance. In this study, only simulation COMP128 fulfils this requirement. A second way of reducing the numerical dissipation, is to use a higher-order spatial differencing scheme. In the next two chapters, the second-order scheme used to spatially discretize the advection terms is replaced by sixth-order scheme.

3

Large-eddy simulation and observations of slope winds

Steady-state quasi-one-dimensional large-eddy simulations of slope winds over simple terrain are presented. The model results of up-slope flow are compared to previous simulations by Schumann (1990), and good agreement is found. Modelled downslope winds are compared to meteorological observations from two glaciers. The vertical profiles of velocity and buoyancy agree with the observations, whereas larger discrepancies are found between the modelled and the observed momentum and buoyancy flux profiles. Despite some discrepancies, the model captures the main characteristics of the observed downslope winds fairly well. The numerical model is used in the next chapter to study how some external input parameters affect katabatic winds.

Chaper is based on Axelsen and Van Dop (2009a).

3.1 Introduction

Thermally driven winds are omnipresent over sloping topography and in mountainous terrain, and these up-slope (anabatic) and downslope (katabatic) winds are important to the local weather and climate (e.g. Oerlemans, 1998). They arise when an inclined surface in a stably stratified environment is heated (cooled), whereby the near-surface air becomes less dense (denser) than the air at the same altitude further away from the slope. This density difference yields the buoyancy of the near-surface air parcel. A positively buoyant air parcel will move up the slope, whereas a negatively buoyant parcel will start descending down the slope.
Slope winds are characterized by wind profiles persistently exhibiting a wind maximum. This maximum is frequently called a low-level jet, and is typically located a couple of metres to tens of metres above the surface. The velocity decreases towards the surface, yielding a large velocity gradient. In katabatic flows, the associated wind shear is the sole production term of turbulence, whereas in anabatic flows, turbulence is also produced through buoyancy. Turbulence in slope flows is responsible for the vertical mixing of momentum and buoyancy in the lowest part of the boundary layer.
Turbulent boundary layer flows are frequently studied using large-eddy simulation (LES). This technique was extensively described in the previous chapter, hence a summary of the concept is deemed sufficient. LES explicitly resolves the motions of the large, energy-containing turbulent eddies, and the motions of these large eddies are therefore called "resolved motions". The large eddies are distinguished from the small eddies by filtering the governing equations. The small eddies have an integral length scale smaller than the filter width, and their influence on the mean flow is parameterized in the so-called subfilter-scale (SFS) model.

During the last couple of decades, LES has been extensively used in numerical studies of the convective boundary layer (CBL), which is characterized by turbulent eddies whose integral length scales are of the same order as the boundary layer depth. In the stable boundary layer (SBL), on the other hand, the turbulent eddies are much smaller. LES studies of the SBL require the use of a fine numerical mesh, and were in the early days of LES not feasible due to high computational costs. During the last 10 - 15 years these computational resources have become available, and the number of LES studies of the SBL has steadily increased. However, only a small number of LES studies has addressed slope winds.
Schumann (1990) (hereafter S90) used LES to study anabatic flows over an infinitely long and wide sloping surface for a range of slope angles and surface roughnesses. He found that the velocity profiles had a maximum close to the surface, and that both the buoyancy and velocity profiles showed negative values in the upper part of the boundary layer. The buoyancy flux decreased linearly with height and became negative in a small portion of the vertical do-

main, similar to the buoyancy flux profiles observed in the horizontal CBL. The TKE budget showed that near the surface, turbulent transport was negative, and the buoyancy production of turbulence exceeded the shear production. Further aloft, the buoyancy became a sink term, and the turbulent transport was the largest production term of TKE.

LES of katabatic flows is a relatively uncharted terrain. To our knowledge, only two papers have reported on this subject. Skyllingstad (2003) simulated katabatic flows by imposing a constant surface cooling on a neutrally stratified ambient atmosphere. The initial and surface boundary conditions were set to mimic the observations by Horst and Doran (1986). Instead of using periodic boundary conditions like in S90, he applied periodicity only in the cross-slope direction, and open boundary conditions in the slope-parallel direction. His mean vertical profiles, which were calculated using data from a horizontal subdomain where the flow was fully turbulent, were found to be in agreement with the measured velocities and temperatures presented by Horst and Doran (1986).

In his analysis of the momentum budget, Skyllingstad (2003) found that the near-surface flow was maintained by a balance between the downslope buoyancy forcing, and the momentum divergence caused by the surface drag. Above the wind maximum, the flow acceleration due to buoyancy was retarded by the slope-parallel advection of lower momentum from further up the slope. Budgets of TKE were also presented. For a given cross-slope wind, he found that the TKE was mainly produced by shear, which was balanced by dissipation through friction and buoyancy. An increase in the (imposed) cross-slope wind would yield an increase in the shear production and in the balancing terms.

Many measurement campaigns of katabatic winds have taken place on a uniform slope. On the other hand, Haiden and Whiteman (2005) argued that a non-uniform slope may significantly influence the katabatic winds. Smith and Skyllingstad (2005) studied the effect of a decreasing slope angle using LES and a meso-scale model (the Advanced Regional Prediction System). They considered a slope consisting of two parts, the upper slope was steep (11.6 ^{o}), whereas the lower was shallow (1.6 ^{o}). A rapid acceleration was found over the upper (steep) slope, followed by a transition to a slower evolving flow characterized by an elevate jet over the lower slope.

Skyllingstad (2003) exemplifies how LES can be used to study katabatic winds. However, his study only considered a limited number of aspects concerning slope flows. Other aspects not yet studied using LES include the sensitivity of katabatic flows to changes in the ambient stratification and the surface buoyancy flux. The effects of these two parameters on steady-state katabatic winds are addressed in the next chapter. Prior to this sensitivity study, the model equations must be formulated and the results must be validated. The LES code builds on the numerical model described in the previous chapter. Modifications required to simulate slope winds are discussed in the next section, and the model is in Section 3.3 validated by comparing the numerical results to sim-

ulations of anabatic flow by S90, and to observations of katabatic winds. Some concerns regarding the SFS parameterization in LES studies of slope flows are discussed in Section 3.4. Based on our results, we discuss in Section 3.5 the ability of LES to simulate slope flow, and give concluding remarks.

3.2 Adjustment to the numerical code

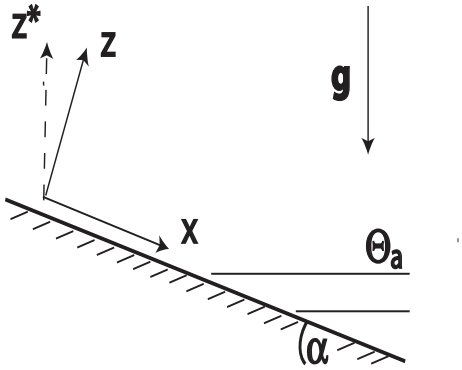

Figure 3.1. Alignment of slope-following coordinate system, rotated by the slope angle α (downslope flow $\alpha > 0$). x, y and z are, respectively, the slope-parallel, cross-slope (into page, not shown), and slope-normal coordinates. Isotherms of the stably stratified ambient atmosphere are denoted by Θ_a. The true vertical direction, i.e. parallel to the gravity vector $\mathbf{g}$, is denoted by an asterisk.

In the previous chapter, version 2.0 of DALES was used to simulate a turbulent flow in the horizontal SBL, whereas in the next two chapters we use version 3.0 to simulate flows over inclined surfaces. Here we sketch the major differences between version 2.0 and 3.0, and describe the modifications required to simulate slope winds. It is deemed unnecessary to repeat all model details, only modifications are addressed.
The governing equations of slope winds are described in a reference frame aligned with the slope. The reference frame is rotated by the slope angle α ($\alpha > 0$ for downslope winds) with respect to the z^* axis, which points in the opposite direction of the gravity vector $\mathbf{g}$, see Figure 3.1. The velocity components parallel and normal to the surface, i.e. in the x and z directions, are denoted by u and w, respectively. The ambient atmosphere is stably stratified, and its potential temperature is in the *non*-rotated coordinate system denoted

by $\Theta_a(z^*)$, with a corresponding lapse rate[1] $\Gamma \equiv \frac{\mathrm{d}\Theta_a}{\mathrm{d}z^*}$. The Brunt-Väisälä frequency is $N = (g\Gamma/T_0)^{1/2}$, where T_0 and g are a constant reference temperature and the constant of gravity, respectively. In the rotated coordinate system, the ambient potential temperature is $\Theta_a(x,z) = T_0 + \Gamma\,(-x\sin\alpha + z\cos\alpha)$. The potential temperature θ of an air parcel participating in the slope flow is the sum of the ambient potential temperature and a deviation, from which the parcel's buoyancy is derived: $b \approxeq \frac{g}{T_0}\,(\theta - \Theta_a)$.
There are two modifications to the momentum equation (2.5). First, the buoyancy term has a component in the the slope-parallel direction. Second, we only consider small-scale slope winds for which the Coriolis force can be neglected. The filtered momentum equation becomes

$$\frac{\partial \overline{u}_i}{\partial t} = -\frac{\partial \overline{u}_i \overline{u}_j}{\partial x_j} - \frac{\partial \overline{\pi}}{\partial x_i} - \overline{b}\,[\delta_{i1}\sin\alpha - \delta_{i3}\cos\alpha] - \frac{\partial \tau_{ij}^{\mathrm{SFS}}}{\partial x_j}, \tag{3.1}$$

where the modified pressure $\overline{\pi}$ and SFS stress tensor τ_{ij}^{SFS} are as in (2.9) and (2.7), respectively, with the latter being modelled as in (2.12). The buoyancy driving the slope flow is determined by the prognostic equation

$$\frac{\partial \overline{b}}{\partial t} = -\frac{\partial \overline{u}_j \overline{b}}{\partial x_j} + N^2\,[\overline{u}_1\sin\alpha - \overline{u}_3\cos\alpha] - \frac{\partial \tau_{bj}^{\mathrm{SFS}}}{\partial x_j}, \tag{3.2}$$

which replaces the thermodynamic energy equation (2.6). The terms including the slope angle α denote the change in buoyancy due to the motions of the air parcel in a stably stratified environment. The SFS heat flux is replaced by an SFS buoyancy flux $\tau_{bj}^{\mathrm{SFS}} = \overline{u_j b} - \overline{u}_j\overline{b}$, which is modelled according to (S90)

$$\tau_{bj}^{\mathrm{SFS}} = -K_b^{\mathrm{SFS}}\left(\frac{\partial \overline{b}}{\partial x_j} + \frac{g}{T_0}\frac{\partial \Theta_a}{\partial x_j}\right), \tag{3.3}$$

with $K_b^{\mathrm{SFS}} = K_m^{\mathrm{SFS}} = c_m\lambda\sqrt{\overline{e'}}$ as in Section 2.3.2. The choice of K_b^{SFS} is discussed in Section 3.4. In a rotated coordinate system, the buoyancy term in the prognostic equation for the SFS TKE (see 2.15) is slightly changed, whereas the other terms remain unchanged:

$$\begin{aligned}\frac{\partial \overline{e'}}{\partial t} &= -\overline{u}_j\frac{\partial \overline{e'}}{\partial x_j} + K_m^{\mathrm{SFS}}\frac{\partial \overline{u}_i}{\partial x_j}\left(\frac{\partial \overline{u}_i}{\partial x_j} + \frac{\partial \overline{u}_j}{\partial x_i}\right) + \frac{\partial}{\partial x_j}K_m^{\mathrm{SFS}}\frac{\partial \overline{e'}}{\partial x_j} - c_\epsilon\frac{\overline{e'}^{3/2}}{\lambda} \\ &- \underbrace{K_b^{\mathrm{SFS}}\left(\frac{\partial \overline{b}}{\partial x_j} + \frac{g}{T_0}\frac{\partial \Theta_a}{\partial x_j}\right)(\sin\alpha\,\delta_{j1} + \cos\alpha\,\delta_{j3})}_{\text{Buoyancy}}.\end{aligned} \tag{3.4}$$

[1]The lapse rate is usually defined as $\Gamma = -dT/dz$, where T is the temperature of the atmosphere (e.g. Holton, 1992). Since the atmospheric temperature decreases with height, Γ is positive. Here the lapse rate is defined as the vertical gradient of the potential temperature, which increases with height, hence in order to preserve the positiveness of the lapse rate we omit the negative sign.

In the previous chapter we argued that the filter width should be larger or equal to the grid distance, $\lambda \geq \Delta$. In this study we focus on shallow katabatic flow where the wind maximum is only a couple of metres above the surface. Consequently the vertical grid distance must be small. Due to high computational costs we must use $\lambda = \Delta$. Moreover, trial simulations became laminar unless the filter width was reduced close to the surface. We are therefore limited to using a filter similar to λ_{COMP}. Here we use that in the lowest 10% of the vertical domain λ decreases linearly to $\lambda = \Delta/2$ as $z \to 0$.
At the surface, a constant buoyancy flux is prescribed. In the wall layer, e.g. between the solid surface and the first model layer, the vertical gradients of velocity and buoyancy are determined by applying standard Monin-Obukhov (MO) theory. In the SBL, these gradients are derived using the non-dimensional gradients for momentum and buoyancy, e.g.

$$\phi_{m,b}(z/L) = 1 + \beta\frac{z}{L}, \tag{3.5}$$

where L is the MO length (e.g. Foken, 2006), and $\beta = 5$ is a constant derived from field measurements (Dyer, 1974). The MO theory was derived from observations in the horizontal boundary layer, where the turbulent fluxes are assumed constant in the lowest part, say $\sim 10\%$, of the boundary layer. The katabatic jet, however, is frequently observed at an altitude smaller than the MO length, hence L is an inadequate scale factor (e.g. Mahrt, 1998; Grisogono and Oerlemans, 2001a,b; Zilitinkevich and Esau, 2007). Grisogono *et al.* (2007) proposed using a modified MO length that was based on L and the height of the low-level jet z_j, i.e. $L_{\mathrm{MOD}}^{-1} = a_1 L^{-1} + a_2 z_j^{-1}$, with a_1, a_2 being unknown coefficients that should be derived from observational data. We have assessed the importance of the correction term $\beta(z/L)$ in (3.5) by comparing a simulation of katabatic flow (with lowest grid level at 20 cm) using the standard MO length to a simulation with $L_{\mathrm{MOD}} = L/2$, and found that the differences were negligible, hence with the chosen numerical resolution it is permissible to apply standard MO theory to the wall layer.
The boundary conditions in the horizontal directions require special attention. Several observations of katabatic winds have shown that the flow variables (velocity components, katabatic layer depth) do not vary significantly with downslope distance, provided the ambient atmosphere is strongly stratified, or the slope is steep (e.g. Haiden and Whiteman, 2005; Whiteman and Zhong, 2008). Under these circumstances, the katabatic flow can be considered one-dimensional, i.e. there is only a height dependence. This is an important assumption in our numerical model. In the horizontal directions, we apply periodic boundary conditions to the velocity components and the SFS TKE (this was also the case in the previous chapter), and to account for the fact that the potential temperatures at the top and bottom of the slope differ, the periodic boundary conditions are applied to the buoyancy $\overline{b}$ (S90).
The assumed invariance with downslope distance was implicitly used in Equa-

tion (3.1). Katabatic winds[2] are subject to a slope-parallel pressure gradient force, which arises due to the drop in elevation as the air descends down the slope. This 'large-scale' pressure gradient force is typically smaller than the buoyancy force (e.g. Mahrt, 1982), and has therefore not been included in the momentum equation. The pressure gradient force in (3.1), on the other hand, arises due to turbulence in the flow. Finally, the periodic boundary conditions affect the entrainment of environmental air into the katabatic layer. Due to the assumed periodicity of the flow, the entrainment zone must be parallel to the inclined surface.

In contrast to v2 of DALES, v3 facilitates the computation of the advection terms by a higher-order differences scheme. Here we apply a sixth-order spatial discretization to the advection term, and a third-order Runge-Kutta time integration scheme is used (e.g. Wicker and Skamarock, 2002). The spatial discretization of the diffusion terms remains unchanged (second-order central-difference scheme).

Lastly we summarise how the LES results are presented. In this study we focus on steady-state slope flows. Since the prescribed surface buoyancy flux continuously heats or cools the boundary layer, the term 'steady-state' may seem inappropriate. However, as in the classical Prandtl (1942) model (described in the next chapter), the buoyancy reaches a steady-state, i.e. the potential temperature difference between the katabatic (anabatic) layer and the ambient atmosphere becomes steady. Consequently, the downslope (up-slope) flow also reaches a steady-state.

Slope flows have an 'oscillating character', e.g. S90 showed that the vertically integrated downslope velocity and buoyancy would oscillate with the period $\tau_{\mathrm{osc}} = 2\pi/(N \sin\alpha)$, see also Fedorovich and Shapiro (2009). This oscillation has the characteristics of a gravity wave propagating in a stably stratified medium. Note that S90 did not consider friction terms, which are responsible for the oscillation amplitude to diminish with time (e.g Shapiro and Fedorovich, 2008). As will be discussed below, the vertically integrated buoyancy and downslope velocity become steady after $2-3$ oscillation periods. All simulations are therefore carried out up to $3\tau_{\mathrm{osc}}$, and the steady-state results have been averaged in time over the last oscillation period. Lastly, we only present slab-averaged quantities. Although the numerical model resolves three-dimensional turbulence, slab-averaging implies that the results are quasi-one-dimensional.

3.3 Model validation

As a first test of the model's ability to simulate slope winds, we perform some simulations of anabatic flow, and compare these with the results presented in S90. In his sensitivity study, the LES results were presented in a non-dimensionalized form. In the remainder we follow that approach and use his

[2]This argument also applies to anabatic winds.

Table 3.1. Summary of the input parameters: slope angle (α), surface buoyancy flux (F_s), and the ambient stratification N. The Brunt-Väisälä frequency and the background potential temperature Θ_a are derived from the balloon measurements in the height interval given in row 5. V, B and H are the scale factors given by Equation (3.6). τ_{osc} is the oscillation period of the slope flow. Abbreviations: A(nabatic), P(asterze), V(atnajökull) and J(ulian) D(ay).

Variable	Unit	A1 Anabatic	P1 JD 212	P2 JD 213	V1 JD 188	V2 JD 189
α	deg	10	5	5	4.5	4.5
F_s	$10^{-3}\,\mathrm{m^2 s^{-3}}$	+4.3	-1.2	-1.5	-0.6	-0.9
N	$10^{-2}\mathrm{s^{-1}}$	0.99	1.21	1.23	1.12	1.37
Height interval	m	-	70-550	110-530	130-260	140-530
V	$\mathrm{ms^{-1}}$	0.66	0.32	0.34	0.23	0.26
B	$10^{-3}\,\mathrm{ms^{-2}}$	6.5	3.8	4.2	2.5	3.5
H	m	66	26	28	20	19
τ_{osc}	10^3s	3.7	6.6	6.5	7.2	5.8

scale factors for velocity, buoyancy and height. They are, respectively

$$V = (|F_s|/N)^{1/2}\,, \quad B = |F_s|/V, \quad \text{and} \quad H = V/N, \tag{3.6}$$

where F_s is the total (i.e. resolved plus SFS) surface buoyancy flux[3]. The model input parameters and scale factors V, B, and H are summarized in Table 3.1. We compare our model results to S90's simulation D10. The domain size is $1700\,\mathrm{m} \times 850\,\mathrm{m} \times 600\,\mathrm{m}$ in, respectively, the along-slope, cross-slope, and slope-normal directions, and is discretized on a $128 \times 64 \times 60$ mesh[4]. The surface roughness length is $z_0 = 0.2\,\mathrm{m}$. At start-up of the simulation, the model requires an initial SFS TKE. Following S90, we use $\overline{e'}|_{t=0} = 0.5V^2 \exp(-20z \sin\alpha/H)$.

Figure 3.2(a) shows our LES results of velocity and buoyancy together with the results presented in S90. The velocity profiles coincide reasonably up to $z/H \approx 3$. The wiggles near the surface are a numerical artefact. The counter flows observed at $z/H \gtrsim 4$ differ to some degree. The magnitude of the counter flow maxima are the same, but whereas S90 found the height of the maximum counter flow to be $z/H \approx 4.5$, we find $z/H \approx 6$. The buoyancy profiles also coincide to a good degree. Both profiles show a decrease in buoyancy with height, and the profiles become negative at $z/H \sim 2$. The model results differ near the surface, where our model shows a larger vertical gradient of buoyancy compared to S90.

[3]This symbol was used for the total heat flux in the previous chapter.

[4]Note that S90's vertical resolution (12.5 m) is slightly coarser than ours (10 m).

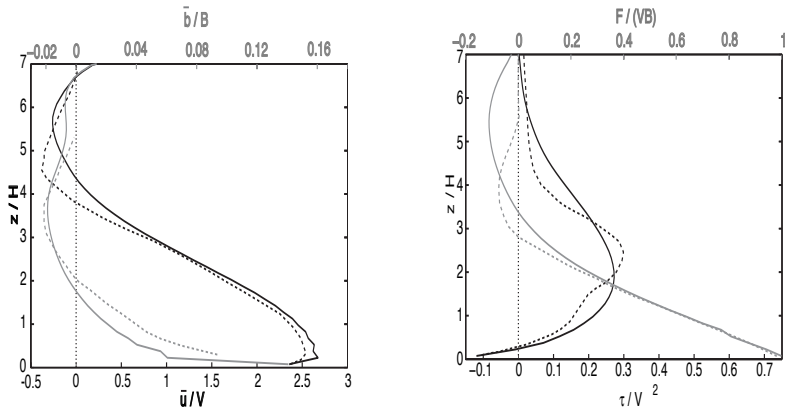

(a) (b)

Figure 3.2. LES (solid) and S90 (dashed) simulated profiles of (a) downslope velocity $\overline{u}$ (black) and buoyancy $\overline{b}$ (grey), and (b) momentum flux τ (black) and buoyancy flux F (grey) versus height.

The vertical fluxes of momentum and buoyancy are shown in Figure 3.2(b). The profiles are the sum of the resolved fluxes and the SFS contributions, i.e. the momentum flux is $\tau \equiv \overline{u}\,\overline{w} + \overline{uw}^{\mathrm{SFS}}$, and the buoyancy flux is $F \equiv \overline{w}\,\overline{b} + \overline{wb}^{\mathrm{SFS}}$. The shapes of the momentum flux profiles qualitatively agree, but we find the maximum to be a bit smaller than in S90, and at a smaller z/H. A relatively good agreement is found for the buoyancy flux profiles. In the lowest part of the vertical domain, up to $z/H \sim 2$, the profiles coincide, but the regions of negative buoyancy flux differ. S90 found the minimum buoyancy flux to be at $z/H \approx 3.5$, which in our simulation is at $z/H \approx 5.5$.
The discrepancies between S90's and our results are likely caused by two factors. First, S90 used a second-order advection scheme, whereas we use a sixth-order scheme. This difference plays an important role in regions where the buoyancy gradient is large, e.g. near the surface and the inversion. With our higher-order scheme, the buoyancy gradient is more accurately determined, which influences the buoyancy flux profile ($\propto \partial\overline{b}/\partial z$). Second, the most important reason is likely related to the filter width λ. S90 used a filter width that was a function of the stability, and his formulation also permitted $\lambda < \Delta$. This is an important parameter in the SFS model, which is the most active near the surface and near the inversion. Although allowing $\lambda < \Delta$ is common practice in LES studies of the CBL, the filter width should not be smaller than the numerical grid distance (e.g. Geurts, 2004). We prefer to use a conceptually correct filter, hence on a relatively low resolution, as in this case, differences between the two models are expected.

3.3.1 Katabatic flow

In order to validate the model's capability to simulate katabatic winds, we compare model results to observations from two glaciers, the Pasterze glacier in Austria, and the Vatnajökull glacier, Iceland. In all simulations, the numerical domain is 250 m in both horizontal directions, and 51 m in the vertical. The number of grid points is $96 \times 96 \times 128$, yielding a grid spacing of 2.6 and 0.4 m in the horizontal and vertical directions, respectively. The choice of the numerical mesh, and its implications, is discussed on Page 61. Lastly, the initial SFS TKE, which is needed to make the flow turbulent in the spin-up phase of the simulation, is in the lowest 25 m of the vertical domain prescribed according to $\overline{e'}(z) = \left[0.4(1 - z/25)^3\right]^{1/2}$ m^{2}s^{-2} (similar to Beare *et al.*, 2006), and zero above.
Prior to comparing model results with observations, we present a short summary of the observations, from which we derive the model input parameters N, F_s, and α.

Pasterze

In the summer of 1994, a glacio-meteorological experiment on the valley glacier Pasterze in Austria was performed (PASTEX). The experiment consisted of instantaneous balloon soundings, and half-hourly averaged mast measurements at six different locations. Details on the measurement sites and instrumentation are given in Van den Broeke (1997a). For the model validation we have used data from the site located at ~ 2100 m above mean sea level. In literature on PASTEX, the site is labelled A1. The glacier surface was fairly uniform from ~ 4 km upstream of the observation site, the glacier tongue was some ~ 800 m downstream, and the distance to each opposing valley wall was ~ 400 m (e.g. Van den Broeke, 1997a). It is therefore reasonable to assume that the observed katabatic flow at this site, averaged over a suitable period of time (we use 30 min), can be considered close to stationary. Implications of these assumptions are discussed in Section 3.5.
Mast measurements of wind and temperature were made at eight levels (0.25, 0.5, 1, 2, 4, 6, 8, and 13 m), whereas the wind direction and the fluxes of momentum and buoyancy were measured at two levels (2.5 and 10.3 m).

For our model validation we have chosen to compare simulations with data from two balloon soundings and the mast measurements conducted at the same time. Capturing the detailed vertical structure of the velocity and temperature profiles with a balloon sounding is usually difficult near the surface. On Julian days 212 and 213, the balloon soundings corresponded well with the mast measurements, and in the lowest 100 - 200 m the balloon data showed only a relatively small spread around the mean velocity and potential temperature profiles. These profiles for Julian days 212 and 213 are plotted in Figures 3.3(a,b), respectively. Only the velocity in the downslope direction is

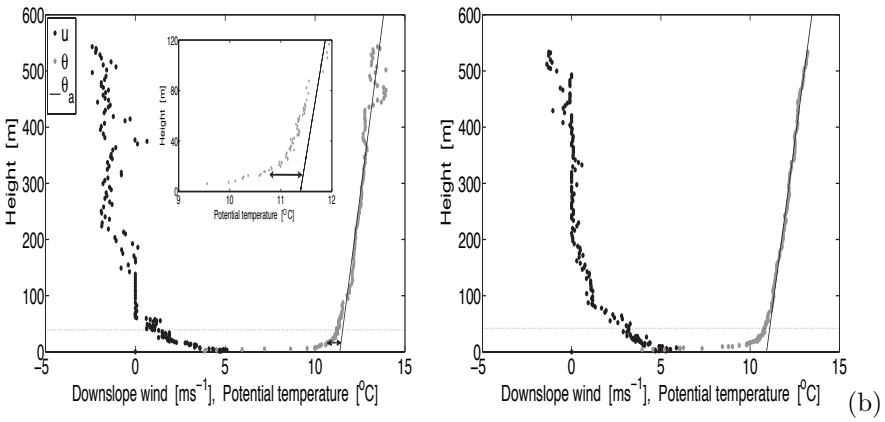

(a) Julian day 212 (b) Julian day 212

Figure 3.3. Wind speed and potential temperature retrieved from balloon soundings on Julian days 212 at 10:30 (a), and 213 at 07:30 (b). Solid line represents estimated background potential temperature. The near-surface potential temperature in (a) has been enlarged, and the arrow shows the potential temperature difference used to calculate the buoyancy, see text for details. Dotted line indicates the height $z/H = 1.5$, which is the maximum height shown in Figures 3.7 and 3.8.

shown. Both soundings show that the maximum downslope velocity is close to the surface. The negative velocities seen at $Z \gtrsim 150$ and $Z \gtrsim 400$ on, respectively, Julian days 212 and 213, indicate an up-slope flow. The figures further show the potential temperature θ. The ambient potential temperature Θ_a is calculated as the linear fit of the top $\sim 40\%$ of the balloon measurements. Table 3.1 shows the height interval over which the linear fit is based.
The simulations of the observed katabatic winds on Julian days 212 and 213 are labelled P1 and P2, respectively. In addition to a prescribed ambient potential temperature field, the simulations require information on the slope angle and the surface roughness length, which are $\alpha = 5\,^{\circ}$ and $z_0 = 4.4$ mm, respectively (Van den Broeke, 1997a). The last required input parameter is the surface buoyancy flux, which is derived from a linear extrapolation of the mast measurements.

Time evolution of the katabatic flow

Before discussing the mean profiles of the katabatic winds, we first look at the time evolution of the flow. In Section 3.2, we introduced $\tau_{\rm osc}$ as an oscillation period for slope flows, and it is also used as a time-averaging period. The oscillation of katabatic flows is inspected in Figures 3.4(a,b). The former shows the oscillatory behaviour of the vertically-integrated, time-dependent downslope

velocity *UD* and buoyancy *BD*, which are defined as (S90)

$$UD(t) = \int_0^\infty \overline{u}(z,t)\mathrm{d}z, \quad \text{and} \quad BD(t) = \int_0^\infty \overline{b}(z,t)\mathrm{d}z.$$

UD and *BD* are calculated using the output from simulation P1. At first the buoyancy increases, i.e. the surface cools, whereby the flow accelerates. With increasing wind speeds, more potentially warm air is advected downslope, which reduces the buoyancy. The flow is retarded as the buoyancy decreases, but with a weak flow, the surface cooling increases again.

Figure 3.4(b) shows the downslope velocity at four different non-dimensional

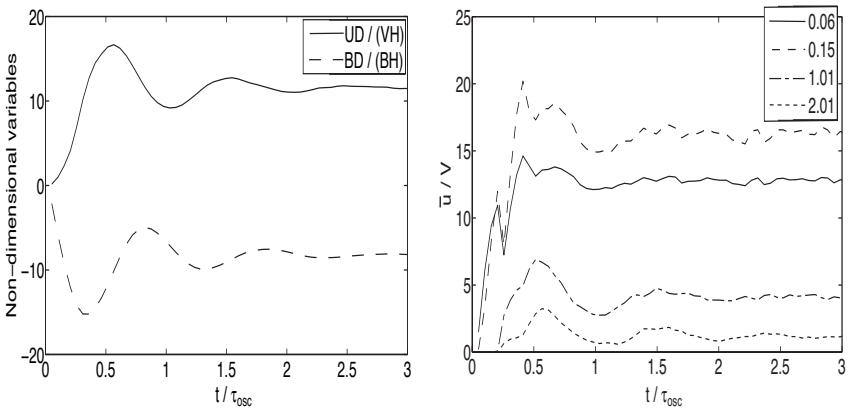

(a) Evolution of vertically integrated downslope velocity and buoyancy

(b) Evolution of downslope velocity at four heights

Figure 3.4. (a) Normalized, vertically-integrated downslope velocity and buoyancy as functions of non-dimensional time, and (b) the time evolution of the downslope velocity at different non-dimensional heights. The normalized height of the wind maximum reaches a steady value of $z_j/H = 0.15$ after $t/\tau_{\mathrm{osc}} \approx 1.5$. Data are from simulation P1.

heights. The velocity starts increasing near the surface before it starts increasing further aloft. At $z/H = 0.06$ (≈ 1.5 m), the velocity becomes more or less constant after $t/\tau_{\mathrm{osc}} = 1$, whereas at other heights the oscillation continues for a longer period of time. The velocities at $z/H = 0.06$ and 0.15 show a sudden drop around $t/\tau_{\mathrm{osc}} \sim 0.2$. Numerical instability is a possible cause of this drop, but we have not found a more concrete explanation.

A simulation whereby the vertical domain size was increased from 51 to 102 m, has shown that the damping in both Figures 3.4(a) and (b) is partly a result of the limited vertical domain size, implying that the sponge layer filling the top 25% of the domain influences the prognostic variables. The damping influences foremost the variables near the domain top, and it diminishes closer

to the surface. The differences are only slightly notable for $z/H \lesssim 1.6$.
The simulation with extended vertical domain has revealed a weak return flow at $z/H \approx 3.5$. The analytical Prandtl model also predicts a return flow, but at a lower height. However, our model results for the downslope velocity are comparable to those of Denby (1999). He compared results from a second-order closure model to the Pasterze observations, and also did not find a return flow below 30 m ($z/H \approx 1$, note that since he used different input parameters, the scale factor H is not fully justified), see his figure 3.

The data from simulation P1 are also used to study the time evolution of

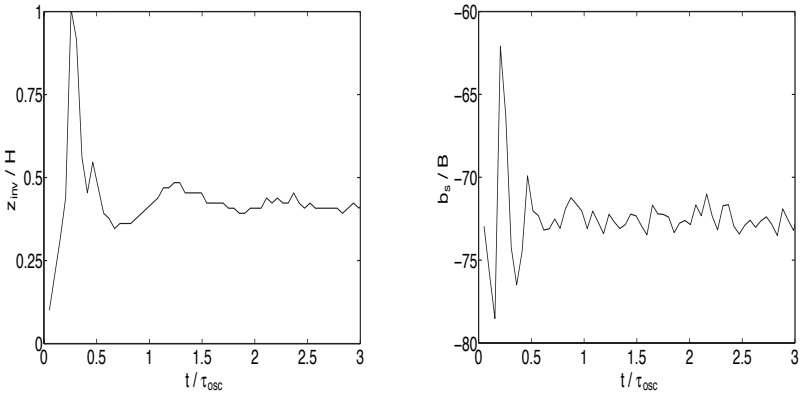

(a) Evolution of the boundary layer depth (b) Evolution of the surface buoyancy

Figure 3.5. Evolution of (a) the normalized inversion height z_{inv} (height where the buoyancy first becomes positive), and (b) the surface buoyancy $\overline{b}_s$. Data are from simulation P1.

the inversion height z_{inv}, which is defined as the height where the buoyancy becomes positive. Figure 3.5(a) shows that at first the imposed surface buoyancy flux rapidly cools the air, whereby z_{inv} increases sharply. The initial SFS TKE is responsible for the vertical mixing of the negative buoyancy throughout the boundary layer. The cooling induces a katabatic wind, which is fully developed at $t/\tau_{\text{osc}} \gtrsim 0.5$ (see also Figure 3.4b). The downslope advection of warm air counters the surface cooling, and consequently reduces z_{inv}. After $t/\tau_{\text{osc}} \sim 0.5$, the inversion height has reached a steady-state.
The time evolution of the surface buoyancy $\overline{b}_s$ is plotted in Figure 3.5(b). The surface buoyancy increases sharply at the beginning of the simulation, thereafter a development of the downslope velocity close to the surface induces a vertical mixing, which reduces $\overline{b}_s$. The relatively large fluctuations in $\overline{b}_s$ for $t/\tau_{\text{osc}} \lesssim 0.75$ are a result of the fluctuations in the near-surface downslope velocity (see Figure 3.4b). For larger t/τ_{osc}, the downslope wind is fairly

constant, and the surface buoyancy fluctuations are small.

Lastly, we address an instantaneous velocity field from simulation P1 at

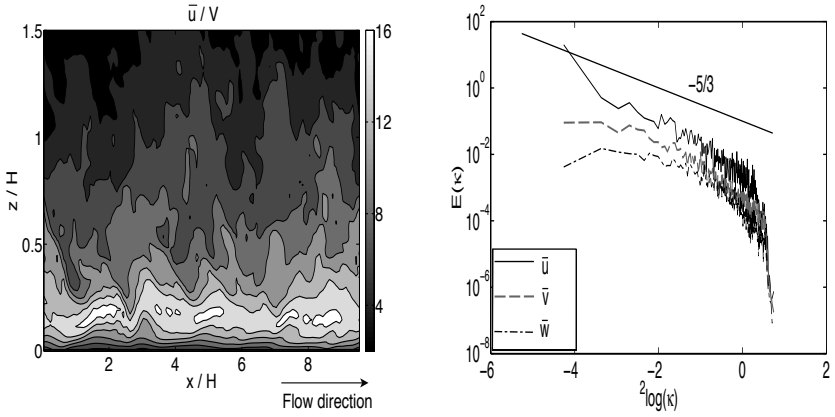

(a) Velocity field (b) TKE spectra

Figure 3.6. Instantaneous downslope velocity field as function of normalized downslope distance and height (a), and TKE spectra as functions of wave number κ (b). Data are from simulation P1 at time $t/\tau_{\text{osc}} = 3$. The energy spectra are evaluated at the height of the wind maximum.

$\tau/\tau_{\text{osc}} = 3$. Figure 3.6(a) shows a contour plot of the downslope velocity as a function of the scaled height and downslope distance, where the latter has for convenience been non-dimensionalized by the height scale H. The velocity increases rapidly from a small value at the lowest grid level, to a maximum at $z/H \approx 0.15$. The wind maximum is in a prominent band of fast and slower moving eddies, which accelerate the slower moving air above the wind maximum. The downslope advection of this elevated slower moving air in turn retards the maximum speed. This interaction between fast and slower moving air at two heights is a first approximation of the momentum budget, which is in agreement with the momentum budgets presented by Skyllingstad (2003). The decrease in $\overline{u}$ above z_j is manifested by the contour lines slanting in the direction opposite to the flow. A movie of subsequent contour plots has shown that most of these disturbances, superimposed on the flow moving toward the right, start slanting more toward the left and finally break, whereas some detach from the low-level jet and propagate upwards, where they eventually mix with the ambient air.

The instantaneous velocity field nicely confirms the model's capability of simulating a turbulent flow despite the relatively coarse horizontal resolution (2.6 m). This is also verified by inspecting the energy spectra of the velocity components, which in Figure 3.6(b) are plotted as functions of the wave

number κ. The data are from simulation P1, and are evaluated at the wind maximum height. All spectra show that there are several scales of turbulent eddies in the simulated katabatic flow, and that the model resolves eddies in the inertial range ($-5/3$ curve). Furthermore, the spectra of both $\overline{v}$ and $\overline{w}$ show a maximum, indicating that the numerical model resolves the largest eddies in the flow. The absence of a maximum in the spectrum of $\overline{u}$, on the other hand, is a result of how the Fourier transformed data were post-processed. Moreover, we do not expect the presence of turbulence eddies with length scales exceeding the horizontal domain size, indicating that the numerical domain is sufficiently large to study quasi-one-dimensional katabatic winds.

Julian day 212

The first balloon sounding and corresponding mast measurements that we use to validate the model's capability of simulating katabatic winds took place on Julian day 212 at approximately 10:30 local time. The background stratification and the surface buoyancy flux were $N = 0.0121\,\mathrm{s}^{-1}$ and $F_s = -0.0012\,\mathrm{m}^2\mathrm{s}^{-3}$ ($\approx$ -32 Wm^{-2}), respectively. Figure 3.7 shows the model profiles together with the observations of the downslope wind speed, buoyancy, and the vertical fluxes of momentum and buoyancy. The standard deviation of the half-hourly averaged mast data of velocity and buoyancy were also stored, and are shown as error bars. Moreover, the measurements at $z = 0.25\,\mathrm{m}$ are omitted due to low quality (Smeets *et al.*, 1998).

Figure 3.7(a) shows that the numerical model captures the height of the observed wind maximum rather well, whereas the wind maximum u_m itself is somewhat overestimated. Although the modelled u_m is not within the standard deviation provided by the mast measurements, the balloon sounding shows that the instantaneously measured velocity may attain values as predicted by the model. Above the wind maximum, the drop in the modelled wind speed is larger than the drop given by the mast measurements. Most data from the sounding also indicate that the drop in observed wind speed is more gradual than the model predicts.

The modelled momentum flux also fits the observations to a good degree, see Figure 3.7(b). Near the surface, the modelled τ is slightly overestimated. At the height of the wind maximum, $z/H \approx 0.15$, the momentum flux vanishes.

Figure 3.7(c) shows that the model captures the mast measurements of buoyancy quite well. The shape of the modelled buoyancy profile also agrees with the balloon measurements, but the values disagree. The modelled buoyancy becomes positive for $z/H \approx 0.75$, whereas the observed buoyancy is only positive around $z/H \sim 4$ ($z \sim 100\,\mathrm{m}$), see Figure 3.3(a). However, it should be noted that determining the background potential temperature from the balloon sounding is not straightforward. To ensure an objective evaluation of Θ_a we selected the $\sim 40\%$ uppermost observations, depending on the number of data points available. Some of these observations may be influenced by large-scale dynamical processes, which are not considered in the katabatic flow. Also,

small errors in the estimation of background potential temperature may change the value of Θ_a at the surface, and thus change the magnitude of the observed buoyancy profile, but not its shape.
Lastly, the surface buoyancy flux was one of the input parameters to the numerical model, which is why the modelled and observed buoyancy fluxes at $z/H \sim 0.1$ should be the same. This is confirmed in Figure 3.7(d), which also shows that the model slightly underestimates the magnitude of F at $z/H \sim 0.3$.

Julian day 213
On the following day, the balloon sounding at approximately 07:30 showed that the background stratification had not changed much, $N = 0.0123\,\mathrm{s}^{-1}$. The surface buoyancy flux was $F_s = -0.0015\,\mathrm{m}^2\mathrm{s}^{-3}$ ($\approx -40\,\mathrm{Wm}^{-2}$). The observations and model results are shown in Figure 3.8.
The magnitude of the modelled wind maximum agrees with the observations, but z_j is slightly underestimated, e.g. Figure 3.8(a). The largest discrepancies between the model and the observations are found above the wind maximum height. As in simulation P1, the modelled wind speed drops faster with height than the observations suggest, but these particular observations show a substantial background downslope wind of $u/V \sim 10$ ($\sim 3\,\mathrm{ms}^{-1}$). The model's ability to capture the shape of the velocity profile near the wind maximum is addressed in Section 3.5.
The observations show a blunt wind maximum, which may be indicative of mixing of momentum, and is supported by the small momentum flux observed above the wind maximum. The modelled momentum flux, however, reaches a substantially larger value, see Figure 3.8(b). Only at the lowest measurement level does the modelled momentum flux match the observations.
The modelled buoyancy, plotted in Figure 3.8(c), agrees rather well with the mast measurements, though some discrepancies are noted at the lowest and highest mast levels. As noted for simulation P1, the model overestimates the buoyancy compared to the balloon measurements. At $z/H \approx 0.6$, the modelled buoyancy changes sign whereas the observed buoyancy only becomes slightly positive at $z/H \sim 7$ ($z \sim 200\,\mathrm{m}$), see Figure 3.3(b). Possible reasons for the discrepancies were discussed above.
The surface buoyancy flux is a model input parameter, and is derived by extrapolating the measured buoyancy flux to the surface. The agreement between the modelled and observed buoyancy fluxes, however, is poor, see Figure 3.8(d). The modelled buoyancy is too large at both measurement levels, and its vertical gradient is too small. The latter suggests that the model produces too much vertical mixing of buoyancy. That, however, is unlikely since the buoyancy profiles agree reasonably well with the observations. Possible reasons for the discrepancies are errors in the observations, or dynamical processes not accounted for in the numerical model, e.g. lateral inhomogenieties and synoptic disturbances.

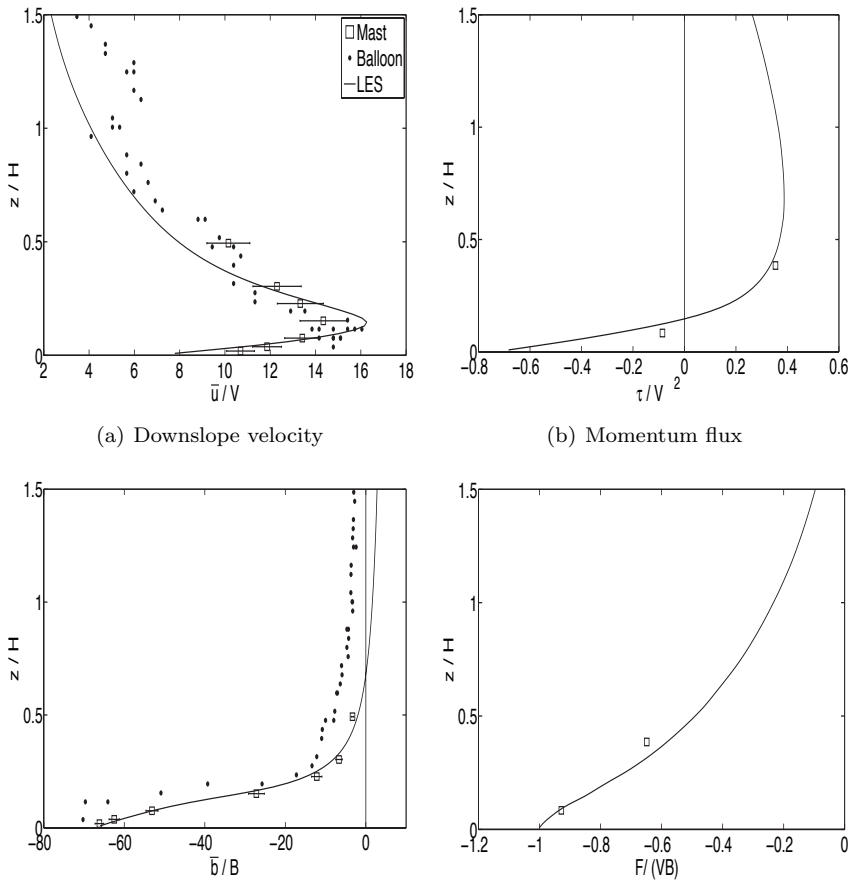

(a) Downslope velocity

(b) Momentum flux

(c) Buoyancy

(d) Buoyancy flux

Figure 3.7. Comparison of the model results to the Pasterze observations from Julian day 212: (a) Downslope velocity, (b) momentum flux, (c) buoyancy, and (d) buoyancy flux. Balloon data are instantaneous, mast observations are half-hourly averaged. The standard deviations of the downslope velocity and bouyancy are shown as error bars. In (c) the markers may be wider than the error bars due to plotting issues.

Vatnajökull

In addition to the Pasterze observations, we have compared our results with observations from the Vatnajökull glacier, Iceland. During the field experiment in summer 1996, measurements were made at 11 different sites. Detailed descriptions of the observational sites and instruments are presented in Oerlemans *et al.* (1999) and Van der Avoird and Duynkerke (1999). We use data from the site referred to as U3, which is situated at $\sim 170\,\mathrm{m}$ above mean sea level.

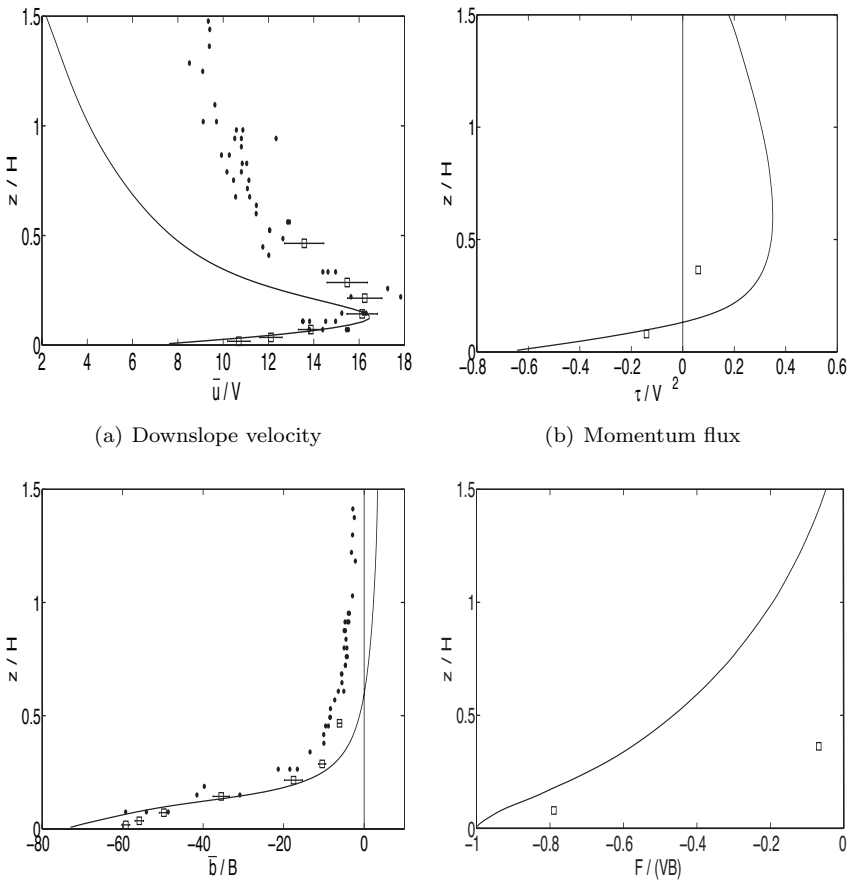

(a) Downslope velocity

(b) Momentum flux

(c) Buoyancy

(d) Buoyancy flux

Figure 3.8. As Figure 3.7 but for Julian day 213.

The glacier extended ~ 10 km upstream of the site, and was located a couple of hundred metres from the terminus and also a couple of hundred metres from a moraine. We have not been able to find better estimates for these distances, but are confident that the surrounding topography does not significantly influence the katabatic winds. At U3, measurements of wind, wind direction and temperature were made at five levels (1, 2, 3, 6 and 9 m) and supplemented by balloon soundings. The measurements of momentum and buoyancy fluxes were made at 3 m, but could unfortunately not be retrieved. Since we cannot estimate the surface buoyancy flux based on the flux observations, we use the F_s that minimizes the discrepancies between the modelled and observed wind and buoyancy profiles. The last LES input parameters are the slope angle and

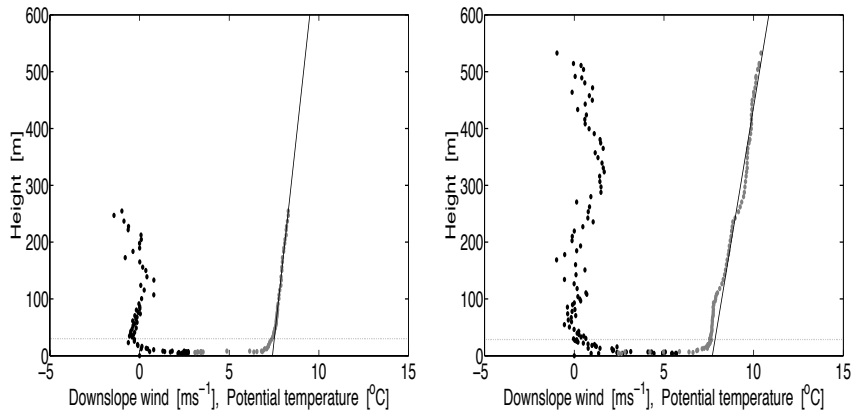

(a) Julian day 188 (b) Julian day 189

Figure 3.9. As Figure 3.3 but for the observations at Vatnajökull on Julian days 188 at 13:15 (a), and 189 at 02:45 (b).

the surface roughness length, which have the values $\alpha = 4.5\,^{\circ}$ and $z_0 = 2.0\,\mathrm{cm}$, respectively.

Two balloon soundings and corresponding mast measurements have been chosen for the model validation. On Julian day 188, the balloon sounding at approximately 13:15 ascended to $\sim 260\,\mathrm{m}$, see Figure 3.9(a). Throughout the ascent, the potential temperature increases monotonically with height. The observations further show a pronounced wind profile with little scatter up to $z \sim 100\,\mathrm{m}$. At $z \approx 25\,\mathrm{m}$, there is a (local) maximum up-slope flow of $u \sim -0.5\,\mathrm{ms}^{-1}$, which is caused by an up-slope ambient wind.

The sounding on Julian day 189 at approximately 02:45 ascended up to $\sim 530\,\mathrm{m}$, Figure 3.9(b). The downslope velocity decreases monotonically up to $z \sim 100\,\mathrm{m}$, and thereafter it remains relatively constant. The potential temperature range can be divided in three regions. Up to $z \approx 15\,\mathrm{m}$, the potential temperature increases sharply, capped by a layer up to $z \sim 100\,\mathrm{m}$, which shows only a weak increase in potential temperature. On top of the second layer is a region with a stronger stratification.

Julian day 188

The sounding gave the background stratification $N = 1.12 \cdot 10^{-2}\,\mathrm{s}^{-1}$, and we estimate the surface buoyancy flux at $F_s = -5.7 \cdot 10^{-4}\,\mathrm{m}^2\mathrm{s}^{-3}$ (corresponding to a heat flux of -20 Wm^{-2}). The modelled and observed velocity and buoyancy profiles are shown in Figure 3.10. The figure, as in Figures 3.7 and 3.8, shows instantaneous balloon measurements and half-hourly averaged mast observations. However, standard deviations of the mast data were not available, hence

error bars are not included in the figure.
Figure 3.10(a) shows that the balloon sounding exhibits a weaker wind maximum and a sharper drop in velocity compared to the mast measurements. The differences are likely a result of the half-hourly averaging of the mast data. The modelled wind maximum is a bit stronger than the mast measurements, and z_j is slightly overestimated. Above the wind maximum, the drop in observed velocity is larger than the model predicts. For $z/H \gtrsim 1$, the observations show an up-slope flow, which is not captured by the model. This up-slope flow is caused by a large-scale forcing, which has not been modelled.
The modelled buoyancy, plotted in Figure 3.10(b), shows a relatively good agreement with the mast data. Near the surface, the modelled buoyancy decrease with height is slightly weaker than in the observations, but for $z/H \gtrsim 0.5$, the modelled and observed buoyancy profiles show the same trend. The shape of the simulated and observed buoyancy profiles agree for $z \gtrsim 0.75$. However, the observations do not attain positive values. This discrepancy was also noted for simulations P1 and P2.

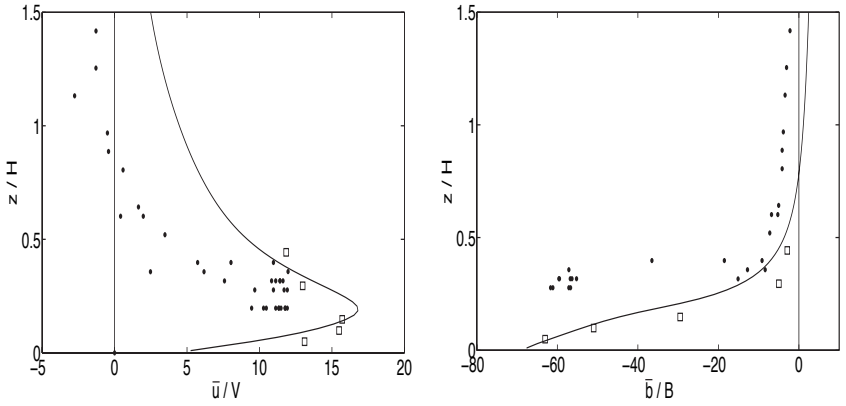

(a) Downslope velocity (b) Buoyancy

Figure 3.10. Comparison of model results to Vatnajökull observations of downslope velocity (a) and buoyancy (b) for Julian day 188. Legends as in Figure 3.7. Note that the standard deviations of the half-hourly averaged mast measurements were not available, hence there are no error bars.

Julian day 189

The last model validation uses data collected on Julian day 189. The background stratification determined from the balloon sounding was $N = 1.37 \cdot 10^{-2}\ \mathrm{s}^{-1}$, and the estimated surface buoyancy flux was $F_s = -9.0 \cdot 10^{-4}\ \mathrm{m}^2\mathrm{s}^{-3}$ (corresponding to a heat flux of $\sim$ -31 Wm^{-2}).
Figure 3.11(a) shows that the balloon sounding did not clearly capture the

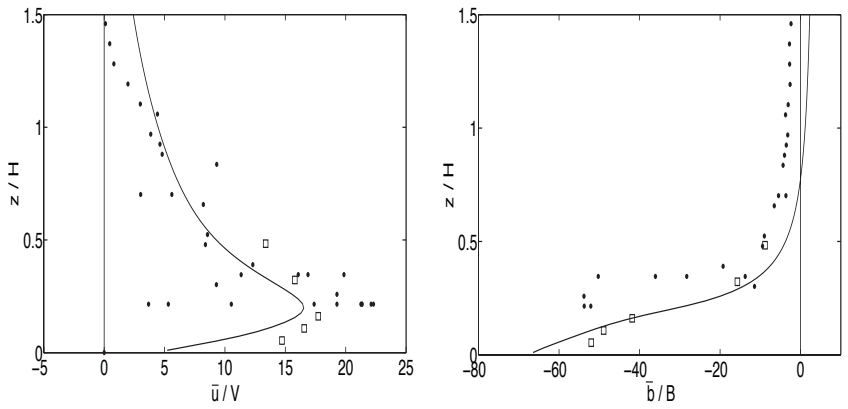

(a) Downslope velocity (b) Buoyancy

Figure 3.11. As Figure 3.10 but for Julian day 189.

wind maximum, and the sounding does not show a clear wind profile close to the surface. However, when comparing the modelled wind speed to the mast measurements, we see that the model slightly underestimates the wind maximum, but successfully predicts its height. As noted above, the modelled wind maximum is too sharp compared to the observations. At larger altitudes, the modelled velocity profile qualitatively agrees with the balloon sounding. Lastly, the shapes of the observed and modelled buoyancy profiles also qualitatively agree, see Figure 3.11(b). Only small differences are noted near the surface, where the modelled buoyancy is slightly larger than the observations.

3.4 Effect of the SFS Prandtl number

In LES studies of the SBL, the SFS contribution to the total TKE is not negligible, and it increases towards the surface. Figure 3.12(a) shows the ratio of SFS TKE to total TKE for simulation P1. At the lowest model level, the SFS contribution to the total TKE dominates. At the height of the wind maximum, $z_j/H \sim 0.15$, the ratio is approximately 10%, and at greater altitudes the ratio remains between 5 and 10%. The other simulations of katabatic winds show similar ratios of SFS to total TKE, whereas the simulation of anabatic flow shows that the SFS TKE is negligible in the entire vertical domain except at the lowest model level.

The SFS exchange coefficients for momentum and buoyancy, K_m^{SFS} and K_b^{SFS}, respectively, are partly determined by the SFS TKE, see Section 3.2. As a consequence of the results presented in Figure 3.12(a), these coefficients will likely play a relatively important role near the surface. In most SFS models,

ours included, the SFS turbulence exchange coefficient for buoyancy is directly related to K_m^{SFS}. It is therefore appropriate to discuss the effect of the SFS Prandtl number, $Pr^{\mathrm{SFS}} \equiv K_m^{\mathrm{SFS}}/K_b^{\mathrm{SFS}}$, on the mean flow.
In several simulations of the CBL, different authors have applied

$$K_b^{\mathrm{SFS}} = (1 + 2l/\Delta)\, K_m^{\mathrm{SFS}}, \tag{3.7}$$

(e.g. Deardorff, 1980; Cuijpers, 1990, 1994; Raasch and Etling, 1991), with l being an SFS mixing length scale that should not exceed the grid scale. Deardorff (1980) argued that in the stably stratified regions of the CBL, l could become much smaller than the grid interval. He therefore proposed using $l = \min\left[\Delta, 0.76\sqrt{\overline{e'}}/N\right]$ in the stably stratified regions. Hence, from (3.7) the SFS Prandtl number becomes unity for very stable conditions, and 1/3 in neutral and unstable conditions. Although this formulation works well in LES studies of the CBL, Equation (3.7) should only cautiously be applied to the SBL. In simulations of the SBL, the grid spacing is much smaller compared to the mesh used in the CBL, and consequently the value 1/3 is unintentionally used for Pr^{SFS}. This value, however, is not representative for the SBL.
A value for the SFS Prandtl number cannot be derived directly from observations. In measurement campaigns of the SBL over flat and sloping surfaces, the vertical separation of the measurement equipment is typically larger than the vertical grid distance used in this LES study (40 cm). The turbulent Prandtl

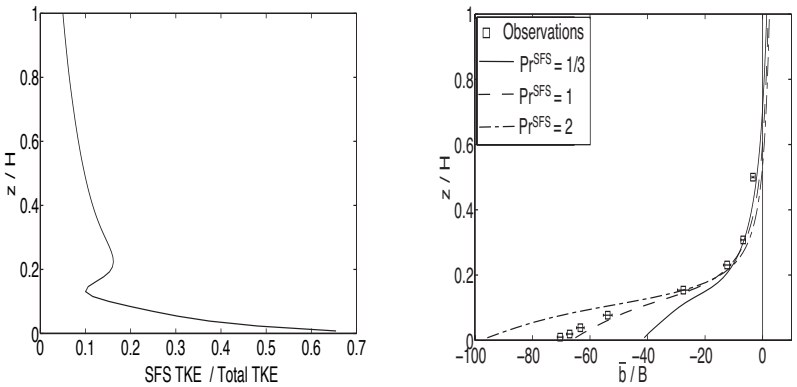

(a) (b)

Figure 3.12. Ratio of SFS to total TKE (a), and buoyancy dependency on SFS turbulent Prandtl number (b). Data are from simulation P1.

number derived from observations,

$$Pr = \frac{\tau/(\frac{\partial u}{\partial z})}{F/(\frac{\partial b}{\partial z})}, \tag{3.8}$$

is therefore likely associated with turbulent eddies whose length scales are larger than the filter width (Note the difference in notation, the superscript 'SFS', does not apply here. The quantities are also not filtered, i.e. no overbars).
Several field studies have focussed on the turbulent Prandtl number as a function of the gradient Richardson number, which is defined as

$$Ri_g = \left(\frac{\partial b}{\partial z}\right) / \left(\frac{\partial u}{\partial z}\right)^2.$$

In some studies, $Pr \sim 1$ for $Ri_g \lessapprox 0.25$ (e.g. Grachev *et al.*, 2007, and references herein), whereas Zilitinkevich *et al.* (2008) in a recent paper proposed $Pr \approx 0.8 + 5Ri_g$. For a gradient Richardson number close to the critical value[5] $Ri_{g,crit} = 0.25$, the Prandtl number becomes $Pr \approx 2$.
In order to study the influence of the SFS Prandtl number on the katabatic flow, we carry out simulation P1 with $Pr^{\mathrm{SFS}} = 1/3$ (a value typically adopted in LES studies of the CBL), 1 (value representing the weakly stratified SBL) and 2 (value used for the moderately stratified SBL). The results have shown that the magnitude of the wind maximum, as well as the vertical gradient of $\overline{u}$ just above z_j, increase with increasing Pr^{SFS}. The best fit to the observations is with $Pr^{\mathrm{SFS}} = 1$, which is the value that we applied in the simulations presented in the previous section. The largest differences between the three simulations are found in the buoyancy profiles. Figure 3.12(b) shows that the simulation with $Pr^{\mathrm{SFS}} = 1$ is the closest to the observations. $Pr^{\mathrm{SFS}} = 1/3$ underestimates the surface buoyancy, whereas $Pr^{\mathrm{SFS}} = 2$ produces too much cooling near the surface. Further aloft, the SFS model becomes less important, and the buoyancy profiles converge. Consequently, the influence of the SFS Prandtl number on the near-surface buoyancy is not negligible, and should be further studied.

3.5 Discussion and summary

LES has proven to help our understanding of the CBL and SBL above flat surfaces, but as of yet, little attention has been paid to simulating the boundary layer over inclined surfaces. A difference between boundary layer flows over a horizontal and an inclined surface is that in the latter, gravity has a component in the direction of the slope. Also, the potential temperature of the ambient

[5]The existence of a critical Ri_g has been questioned in literature (e.g. Zilitinkevich *et al.*, 2007), but this is not directly relevant to this study.

atmosphere varies along the flow direction. In this paper, we have presented an LES code that was designed for simulating the horizontal boundary layer, and the modifications that permit the simulation of slope winds. A test of the model consisted of a simulation of anabatic flow, which was compared to the LES results by S90. We have found similar results for the vertical profiles of velocity, buoyancy, and fluxes of momentum and buoyancy, especially close to the surface.

The model's ability to simulate katabatic winds has been analysed using four sets of selected observations, two from the Pasterze glacier (Austria), and two from the Vatnajökull glacier (Iceland). The former site provided observations of momentum, buoyancy, and fluxes of momentum and buoyancy. The observations on Vatnajökull only provided data on the momentum and buoyancy profiles.

Since the surface buoyancy flux could not be determined from the Vatnajökull observations, we chose F_s such that the velocity and buoyancy profiles would agree with the observations. The values that we used are in the range $-6 \cdot 10^{-4}$ to $-9 \cdot 10^{-4}\,\mathrm{m^2 s^{-3}}$ (the corresponding heat flux is in the range -20 to -30 $\mathrm{Wm^{-2}}$), which are similar to values found by Parmhed *et al.* (2004). We have also used the bulk method (described in e.g Denby and Greuell, 1999) to estimate the surface buoyancy fluxes from the mast measurements. This method estimates F_s by (arguably) applying MO theory to the temperature difference between a specific height and the surface. Here the temperature difference is derived from the mast measurements at 1 m, and the fact that the ice is at the melting temperature. For Julian day 188, the bulk method yields $F_s = -9.2 \cdot 10^{-4}\,\mathrm{m^2 s^{-3}}$, whereas we used a value that was approximately 37% smaller, e.g. $F_s = -6.0 \cdot 10^{-4}\,\mathrm{m^2 s^{-3}}$. On this day, however, a significant upslope ambient wind was observed, see Figures 3.9(a) and 3.10(a). Since we made no effort to model this ambient wind, we had to use a smaller surface buoyancy flux in order to capture the magnitude of the wind maximum. On Julian day 189, on the other hand, the surface buoyancy flux estimate from the bulk method, $F_s = -9.9 \cdot 10^{-4}\,\mathrm{m^2 s^{-3}}$, was much closer to the value used in the simulation, e.g. $F_s = -9.0 \cdot 10^{-4}\,\mathrm{m^2 s^{-3}}$.

The Pasterze observations did give an estimate of the surface buoyancy flux. In both simulations P1 and P2, the model slightly overestimated u_m, and the modelled vertical gradients of velocity were too large near z_j, i.e. the wind maximum was too sharp. The sharpness of the modelled wind maximum suggests that the model underestimates the mixing of momentum at that height. Some factors responsible for mixing or transporting momentum are not incorporated into the numerical model. The SBL can sustain internal waves, which can transport momentum. Based on observations of katabatic flow, Monti *et al.* (2002) found that the effective eddy diffusivity of momentum increases with increasing gradient Richardson numbers. Since the largest gradient Richardson numbers in katabatic flow are found near the wind maximum, we cannot exclude the possibility that waves are important in the vertical redistribution of

momentum around the wind maximum height z_j.
The observed wind profiles may also be affected by any inhomogeneity in the along- and cross-slope directions. For instance, whereas the Pasterze glacier is embedded in a valley with a limited width and length, the numerical model assumes an infinite wide and long surface. Also, the solar heating at Pasterze is unevenly distributed over the valley sides. This differential heating, which has a diurnal cycle, produces an additional circulation that the model does not account for. A cross-slope flow influences the sharpness of the wind maximum. The LES study by Skyllingstad (2003) showed that the sharpness decreased with increasing (imposed) cross-slope wind: An increase in the cross-slope wind will increase the turbulence, whereby the wind maximum is smoothened out.
Whereas observations of the downslope velocity in katabatic winds often show a blunt wind maximum, numerical models tend to predict a sharp maximum. Denby (1999) argued that 1 and 1.5-order closure models predict a decoupling of the katabatic flow below and above z_j, but his second-order closure model also predicted a strong decrease in wind speed above the wind maximum height. Apparently, in reality, usually more forcings are present in slope flows than just the katabatic forcing.
In the model validation of katabatic winds we have looked at buoyancy profiles. All simulations show that the shape of the simulated buoyancy profiles qualitatively agree with the observations, but the magnitude of the simulated profiles is slightly larger than the observations. However, we have noted that determining the background potential temperature gradient is not straightforward, and that small errors in Θ_a may influence the magnitude of the observed buoyancy.
Lastly, the Pasterze observations further provided data on the momentum and buoyancy fluxes. Simulation P1 shows that the modelled fluxes agree with the observations, whereas for simulation P2 the agreement is rather poor.
Although there are certain discrepancies between the model results and the observations, we must stress that our numerical simulations have captured the main features of slope winds. It should further be noted that we have not tried to model all details of the observations. For instance, we have not considered any large-scale forcing nor a time variability, and the geometries of the observational sites have been simplified, i.e. the surface buoyancy, surface roughness and slope angle are assumed to be homogeneous. Any inhomogeneity in these parameters will affect the steady-state flow. It must therefore be stressed that we have simulated idealized flows.
In this chapter we have focussed on validating the numerical model's ability to simulate katabatic winds. We are confident that the numerical model can be used to study katabatic flows subject to different external factors. In the next chapter, we report on the influence of the ambient stratification and surface buoyancy flux on katabatic winds over moderately steep slopes.

4

Large-eddy simulation of katabatic winds. A sensitivity study and comparison with analytical models

The effects of the slope angle, surface buoyancy flux, and background stratification on steady-state katabatic winds are studied using large-eddy simulation (LES). Our numerical results are interpreted in light of the analytical Prandtl model, and we find that our vertical profiles of the downslope velocity, buoyancy, and the momentum and buoyancy fluxes exhibit many of the features from the analytical solution. On the other hand, there are also differences between the analytical and numerical results due to the assumptions in the analytical model. One of the assumptions is that the Prandtl number is constant throughout the boundary layer. However, the simulations show that this number varies with height, and also that the Prandtl number increases with increasing gradient Richardson number. The immediate benefit of LES over analytical models is its capability of resolving turbulent motions. In our study of the turbulence kinetic energy budgets, we find that the wind shear is the largest production term, and that it is mainly balanced by turbulence dissipation. Near the wind maximum, where the shear vanishes, turbulence transport is the only production term. The turbulence transport of buoyancy throughout the boundary layer is related to the surface buoyancy flux. Two linear expressions for estimating the surface buoyancy flux from mean quantities are derived from the Prandtl model, which has some degrees of freedom, hence the slopes of these linear relations can be fitted to observations. Both relations are verified by the LES results, though the linear regression coefficients based on the numerical results yield different slopes. However, these analytical and LES relations show a less satisfactory agreement with observations, which is likely caused by uncertainties in the observational data set. One of the relations is also compared to a more idealized data set (consisting of e.g. time-averaged observations and numerical simulations), yielding promising results.

Chaper is based on Axelsen and Van Dop (2009b).

4.1 Introduction

When the surface is colder than the overlying atmosphere, the boundary layer becomes stably stratified. A stable boundary layers (SBL) is formed by e.g. radiative cooling of the surface during the night or the polar winter. SBLs are in summer also common over the ablation zones of glaciers since the temperature of the ice cannot exceed the melting point while the near-surface air temperature typically does. These conditions are favourable for the formation of katabatic flows. They arise when the air adjacent to a sloping surface cools more than the air at the same elevation, but away from the surface. The differential cooling in the horizontal direction causes the near-surface air to become negatively buoyant with respect to its environment, triggering a downslope flow. This katabatic wind typically has a persistent wind profile exhibiting a wind maximum close to the surface. There a substantial wind shear generates turbulence, which is responsible for the exchange of buoyancy (heat) and momentum between the surface and the free atmosphere.
Though steady katabatic winds occur only in a stratified environment, they are often moderated by external factors. The potential temperature field of the ambient atmosphere is one factor. First, its stratification plays an important role in how large speeds the flow can attain, i.e. the maximum downslope velocity is inhibited by a large stratification. Second, the ambient potential temperature does, in combination with the temperature of the surface, determine the surface buoyancy, which drives the flow. Katabatic winds are furthermore moderated by the slope angle, the roughness of the surface, ambient winds, etc.
Several analytical models have been used to study the mean profiles of katabatic winds. One of the first was presented by Prandtl (1942). His analytical model is valuable in studies of one-dimensional katabatic flows, e.g. what Mahrt (1982) calls 'equilibrium flow' (see also Chapter 1). It considers local equilibria in in terms of the momentum and thermodynamic energy equations (the latter being expressed in terms of buoyancy, and is thus also called the buoyancy equation). In the former, acceleration by gravity is opposed by a momentum flux divergence, whereas in the latter, the downslope advection of warm air balances the cooling by the slope-normal buoyancy flux divergence. By applying first-order closure, and assuming constant turbulence exchange coefficients, vertical profiles of the downslope velocity and the buoyancy are found.
In observations of katabatic winds, the profiles of velocity and buoyancy show steep gradients near the surface. The Prandtl model underestimates theses gradients because of the constant turbulence exchange coefficients. Grisogono and Oerlemans (2001a) (hereafter GO01a) extended the classical Prandtl model to solve the katabatic flow problem using gradually varying, height-dependent turbulence exchange coefficients, and constant but arbitrary Prandtl number. Despite having to prescribe the turbulence exchange coefficients, it was found that their analytical model (hereafter GO model) better fits the observations than the classical Prandtl model. In subsequent studies, Grisogono and Oer-

lemans (2001b) (hereafter GO01b) and Parmhed *et al.* (2004) used the GO model to estimate the surface fluxes of momentum and buoyancy, and a good comparison with observations was found. Grisogono (2003) later extended the GO model to include time dependence, and Stiperski *et al.* (2007) and Kavcic and Grisogono (2007) more recently included the effect of the earth's rotation. Gutman and Malbakhov (1964), and Shapiro and Fedorovich (2008) also describe analytical models including the Coriolis force, which over the large ice sheets of Greenland and Antarctica becomes important (e.g. Van den Broeke *et al.*, 2002).

Although analytical models have advanced the general knowledge on katabatic flows, they are limited by several assumptions, and can only approximate the effect of turbulence on these downslope winds. Large-eddy simulation (LES), on the other hand, is a technique that is well suited for studying turbulent flows, and was in the previous chapter introduced as a tool to simulating slope winds. In LES, the motions of large turbulent eddies are explicitly resolved ("resolved motion"). These large eddies are distinguished from small eddies by filtering the governing equations. The small eddies have a characteristic length scale smaller than the filter, and their effect on the mean flow is parameterized in the so-called subfilter-scale (SFS) model. The reader is referred to Chapters 2 and 3 for a detailed discussion on the model equations and assumptions, here we only recapitulate on two important assumptions: It is assumed that the katabatic winds are in a steady-state, and that the flow is a function of height only. As such, the results must be considered quasi one-dimensional, although the numerical model is capable of resolving three-dimensional turbulence.

LES allows us to examine how steady-state katabatic winds are affected by changes to several external parameters. Here we use LES to study the influence of the ambient stratification, the slope angle, and the surface forcing on katabatic flows. The Prandtl model, described in Section 4.2, is extensively used to explain the model results, which are presented in Section 4.3. In Section 4.4 we compare the Prandtl and GO models to our LES results. Two parameterizations for estimating the surface buoyancy flux are derived from the analytical models, and are compared to the LES results in Section 4.5, and contrasted to observations in Section 4.6.

4.2 Analytical models

The analytical Prandtl and GO models present a simple way of studying steady-state katabatic winds over an infinite surface. In this section, we summarize these two models, and derive two analytical expressions for estimating the surface buoyancy flux. These expressions are compared to our LES results in Section 4.5, and in Section 4.6 to observations of katabatic winds.

4.2.1 The Prandtl model

The analytical model describes a katabatic flow in a slope-following coordinate system, which is inclined at an angle α (downslope: $\alpha > 0$) to the horizontal. The flow variables are only functions of the slope-normal distance to the surface, z, hereafter called height. In the simplified downslope momentum equation (full equation given in 3.1), the along-slope component of buoyancy accelerates the flow, and is opposed by the momentum flux divergence. In the buoyancy equation, the downslope advection of warm air balances the slope-normal buoyancy flux divergence (see also 3.2)

$$b \sin\alpha = \mathrm{d}\tau/\mathrm{d}z, \quad \text{and} \tag{4.1}$$

$$uN^2 \sin\alpha = -\mathrm{d}F/\mathrm{d}z. \tag{4.2}$$

Here u is the downslope velocity, b the buoyancy, $N = (g\Gamma/T_0)^{1/2}$ is the Brunt-Väisälä frequency with g and T_0 being, respectively, the gravitational acceleration and a constant reference potential temperature, and Γ is the (constant) lapse rate[1] of the ambient atmosphere. τ and F are the fluxes of momentum and buoyancy, respectively. These fluxes are normally modelled using first-order closure yielding (e.g. Oerlemans, 1998)

$$b \sin\alpha = -\mathrm{d}\left(K_m \mathrm{d}u/\mathrm{d}z\right)/\mathrm{d}z, \quad \text{and} \tag{4.3}$$

$$uN^2 \sin\alpha = \mathrm{d}\left(K_b \mathrm{d}b/\mathrm{d}z\right)/\mathrm{d}z, \tag{4.4}$$

where K_m and K_b are the turbulence exchange coefficients for momentum and buoyancy, respectively. According to the Prandtl model, K_m and K_b are assumed to be constant. The ratio K_m/K_b is a model parameter to the Prandtl model, and is denoted as the Prandtl number Pr[2].

For boundary conditions, we require the velocity and buoyancy to vanish as $z \to \infty$. At the surface, the no-slip condition is applied to u, and the buoyancy is prescribed, its value being b_s. Following GO01a,b one obtains the solution

$$b = b_s \exp\left(-\sigma_c z\right) \cos\left(\sigma_c z\right), \tag{4.5}$$

$$u = -\frac{b_s}{N\sqrt{Pr}} \exp\left(-\sigma_c z\right) \sin\left(\sigma_c z\right), \tag{4.6}$$

where

$$\sigma_c^2 = \frac{\sigma_0}{2K_b} \quad \text{and} \quad \sigma_0^2 = \frac{N^2 \sin^2\alpha}{Pr}. \tag{4.7}$$

[1] For our definition of the lapse rate see footnote on page 51.

[2] In this thesis, three different Prandtl numbers are used. We distinguish between the Prandtl number of the resolved motions, the Prandtl number of the subfilter-scale model (only Chapter 3), and an overall (turbulent) Prandtl number (e.g. the sum of the former two) . In the analytical model, Pr is an overall number. For the sake of simplicity we do not markedly distinguish between the overall Prandl number and the Prandtl number of the resolved motions since the subfilter-scale model in the bulk of the boundary layer only plays a minor role.

The surface buoyancy flux is given by $F_s = -K_b \mathrm{d}b/\mathrm{d}z|_{z=0}$, or

$$F_s = K_b b_s \sigma_c. \tag{4.8}$$

This relation may be used to reformulate the solution (4.5) and (4.6) in terms of a flux boundary condition (F_s). Substituting Equation (4.7) in (4.8) yields

$$K_b = 2\left(\frac{F_s}{b_s}\right)^2 \frac{\sqrt{Pr}}{N \sin\alpha}. \tag{4.9}$$

The height of the wind maximum follows from (4.6), $z_j = \pi/(4\sigma_c)$, which can be rewritten using (4.9):

$$z_j = \frac{\pi\sqrt{Pr}}{2} \frac{F_s}{b_s N \sin\alpha}. \tag{4.10}$$

F_s, N, and α are input parameters in our numerical model. Collecting these parameters on one side of the equality yields

$$b_s z_j = \frac{\pi\sqrt{Pr}}{2} \frac{F_s}{N \sin\alpha} = c_1^{\mathrm{Pr}} \frac{F_s}{N \sin\alpha}. \tag{4.11}$$

The constant c_1^{Pr} is discussed below.
The magnitude of the wind maximum is

$$u_m = -\frac{\sqrt{2}}{2} \frac{e^{-\pi/4}}{\sqrt{Pr}} \frac{b_s}{N}, \tag{4.12}$$

or, on a rearranged form such that LES output and input parameters are separated,

$$b_s u_m^{-1} = -\sqrt{2Pr}\, e^{\pi/4}\, N = -c_2^{\mathrm{Pr}}\, N, \tag{4.13}$$

where c_2^{Pr} is a constant that is addressed below.
In the analysis hereafter we shall also use the product of u_m and z_j:

$$u_m z_j = -\frac{\sqrt{2}}{4}\, \pi e^{-\pi/4} \frac{F_s}{N^2 \sin\alpha} = -c_3^{\mathrm{Pr}} \frac{F_s}{N^2 \sin\alpha}. \tag{4.14}$$

The left hand sides of Equations (4.11, 4.13, 4.14) include the LES output parameters only. According to these relations, they are proportional to the LES input parameters (F_s, N, and α), where the proportionality constants are denoted by c_i^{Pr}. It is interesting to note that in the Prandtl formulation these constants do not explicitly depend on the numerical value of K_b. However, there is an implicit dependence since these relations were derived using (4.8). c_i^{Pr} therefore have one degree of freedom due to the fact that K_b can be arbitrarily chosen. The constants c_1^{Pr} and c_2^{Pr} furthermore explicitly depend on the Prandtl number, which is a second degree of freedom.

4.2.2 Grisogono's approach

Shortcomings in the Prandtl model are the use of first-order closure and the assumption of constant eddy viscosity/diffusively. In turbulence theory, it is common practice to reduce K near the surface, letting it be proportional to z, resulting in (experimentally confirmed) logarithmic behaviour of the mean profiles in the neutral surface-layer. GO01a,b show that also katabatic flows profiles of temperature and velocity tend to be steeper than predicted by the Prandtl model (see Figure 3 in GO01a). In the GO model, the assumptions (4.3, 4.4) are retained, and K_b is a height-dependent function with the proper limiting behaviour for $z \to 0$. Assuming that $K_b(z)$ is a slowly varying function, Grisogono was able to obtain 'Prandtl-like' analytic solutions which indeed show steeper gradients for $z \to 0$. Without derivation we give the expressions (see GO01b) for the height and magnitude of the wind maximum

$$z_j = \frac{\pi^2}{32}\sqrt{e\ Pr}\,\frac{K_{b,max}}{hN\sin\alpha}, \tag{4.15}$$

$$u_m = -\frac{\sqrt{2}}{2}\ \frac{e^{-\pi/4}}{\sqrt{Pr}}\ \frac{b_s}{N}. \tag{4.16}$$

The expression for u_m is identical to that of Prandtl. On the other hand, the expression for z_j contains two extra parameters, which are the maximum value of the $K_b(z)$-profile ($K_{b,max}$), and the height h where $K_b(z)$ attains its maximum value. (Note that in his approximate calculations he assumes $z_j/h \ll 1$). These parameters offer somewhat more freedom to fit the theoretical profiles to experimental data. In combination with the steeper gradients near the surface, a better agreement with observations may be found, though there are still discrepancies.

Using relation (4.4) in GO01b, we may relate the value of $K_b(z_j)$ to $K_{b,max}$ according to $K_b(z_j) \approx \sqrt{e}\ z_j/h\ K_{b,max}$, and combined with their relation (4.8a) rewrite the expression for z_j as

$$z_j = \sqrt{\frac{Pr}{32}}\ \pi e^{\pi/4}\ \frac{F_s}{b_s N\sin\alpha}, \quad \text{which re-arranged yields}$$

$$b_s z_j = \sqrt{\frac{Pr}{32}}\ \pi e^{\pi/4}\ \frac{F_s}{N\sin\alpha} = c_1^{\mathrm{GO}}\ \frac{F_s}{N\sin\alpha}. \tag{4.17}$$

The latter expression is similar to that of Prandtl (Equation 4.11), they differ in the proportionality constants c_1^{GO} and c_1^{Pr}.

The expression for the wind maximum, Equation (4.16), is identical to (4.12), and can thus be put in a form similar to (4.13):

$$b_s u_m^{-1} = -c_2^{\mathrm{GO}}\ N, \tag{4.18}$$

with $c_2^{\mathrm{GO}} = c_2^{\mathrm{Pr}}$. Lastly, the product $u_m z_j$ becomes

$$u_m z_j = -\frac{\pi}{8}\ \frac{F_s}{N^2\sin\alpha} = -c_3^{\mathrm{GO}}\ \frac{F_s}{N^2\sin\alpha}. \tag{4.19}$$

The constants c_i^{GO} have two degrees of freedom since they implicitly depend on the height-dependent buoyancy exchange coefficient $K_b(z)$, which is a function of h and $K_{b,max}$. c_1^{GO} has one more degree of freedom since it also depends on the Prandtl number.

4.3 Large-eddy simulations

4.3.1 Model input

In this section, we use LES to study the influence of F_s, N, and α on the katabatic flow structure. The employed numerical model was described in Section 3.2. Since we in the previous chapter used two different numerical domains (e.g. for simulating up-slope and downslope flows), it is worth clarifying which numerical mesh we use, and how the model output is treated.

The extent of the numerical grid is 256 m in the horizontal directions, and 51 m in the vertical direction. We use 128 grid points in each direction, yielding a grid spacings of 2.0 and 0.4 m in the horizontal[3] and vertical directions, respectively. In contrast to the previous chapter, we have raised the surface roughness length from 4 mm to 10 mm.

The sensitivity study includes 12 simulations, which differ in the combinations of the three input parameters F_s, N, and α. We use three different surface buoyancy fluxes, ranging from -1.08 to $-2.15 \cdot 10^{-3}\mathrm{m^2 s^{-3}}$, which corresponds to surface heat flux values in the range -35 to -70 $\mathrm{Wm^{-2}}$. Three stratifications of the ambient atmosphere are used, with the value for N ranging from 0.99 to $1.41{\cdot}10^{-2}\mathrm{s^{-1}}$ (corresponding lapse rate: 3 to 6 K $\mathrm{km^{-1}}$). The last parameter in the sensitivity study, the slope angle α, ranges from 3 to 6 °. The simulation input parameters and some key results are summarized in Table 4.1.

All numerical simulations have been carried out up to $3\tau_{\mathrm{osc}}$, where $\tau_{\mathrm{osc}} = 2\pi \left(N \sin\alpha\right)^{-1}$ is the oscillation period of the katabatic flow (e.g. Schumann, 1990; Shapiro and Fedorovich, 2008; Fedorovich and Shapiro, 2009, and Chapter 3). In the remainder, we present slab-averaged profiles of first- and higher-order moments, which have been averaged in time over the last oscillation period.

Lastly, a remark should be made with respect to the notation. In the previous chapter we distinguished between resolved (denoted by an overbar) and SFS scale turbulent eddies (denoted by the superscript 'SFS'). However, since we in this paper mostly present total fields, i.e. resolved motion plus SFS contribution, this distinction is discontinued.

[3] In Chapter 3, the number of grid points in the horizontal directions was 96, and the horizontal grid distance was 2.6 m.

Table 4.1. Summary of input parameters: stratification of the ambient atmosphere N, the surface buoyancy flux F_s, and the slope angle α. The results for the wind maximum u_m, the wind maximum height z_j, and the surface buoyancy b_s are also included. Note that the latter is evaluated at the surface and not at lowest model level, which explains the difference between values in this table and Figure 4.2.

Simulation	N	F_s	α	u_m	z_j	b_s
Unit	10^{-2} s^{-1}	10^{-3}m^{2}s^{-3}	deg	ms^{-1}	m	ms^{-2}
N1F1A1	0.99	-1.08	3.0	7.42	5.0	-0.40
N1F1A2	0.99	-1.08	4.5	6.02	3.8	-0.33
N1F1A3	0.99	-1.08	6.0	5.14	3.4	-0.29
N1F2A3	0.99	-1.61	6.0	6.64	3.4	-0.38
N1F3A3	0.99	-2.15	6.0	7.91	3.8	-0.46
N2F1A1	1.22	-1.08	3.0	6.34	3.2	-0.39
N2F1A3	1.22	-1.08	6.0	4.35	3.0	-0.28
N2F2A2	1.22	-1.61	4.5	6.51	3.8	-0.43
N2F3A3	1.22	-2.15	6.0	6.60	3.4	-0.45
N3F1A1	1.41	-1.08	3.0	5.61	3.8	-0.38
N3F2A1	1.41	-1.61	3.0	7.24	4.2	-0.51
N3F3A3	1.41	-2.15	6.0	5.84	3.0	-0.44

4.3.2 Results

Mean flow

We begin by looking at the mean flow, and focus on the simulations, which illustrate the effects of the background stratification, surface forcing, and slope angle. We are interested in the flow near the wind maximum, and show therefore only data for the lowermost 30 m of the vertical domain.

Using a closure model, Nappo and Rao (1987) studied the effect of the ambient stratification on steady-state katabatic winds. Two simulations with stratifications[4] $N = 0.2$ and $1.9 \cdot 10^{-2}$ s^{-1} showed that the flow became considerably weaker and shallower with increasing background stratification. This result is also predicted by the Prandtl model. In the relations for the magnitude and height of the wind maximum, Equations (4.12) and (4.10), respectively, N appears in the denominators. By increasing N, both u_m and z_j decrease. Our simulations collaborate these findings. Figure 4.1(a) shows that by increasing N from 0.99 to $1.41{\cdot}10^{-2}$s^{-1} (simulations N1F3A3 and N3F3A3), the magnitude and height of the wind maximum decrease markedly.

The surface buoyancy flux also influences the katabatic wind profiles by increasing the negative buoyancy near the surface (see below), which accelerates

[4]The authors presented the stratification in terms of the lapse rate, e.g. 0.1 and 10 K km^{-1}. Here N is calculated using the reference temperature $T_0 = 273.15$ K.

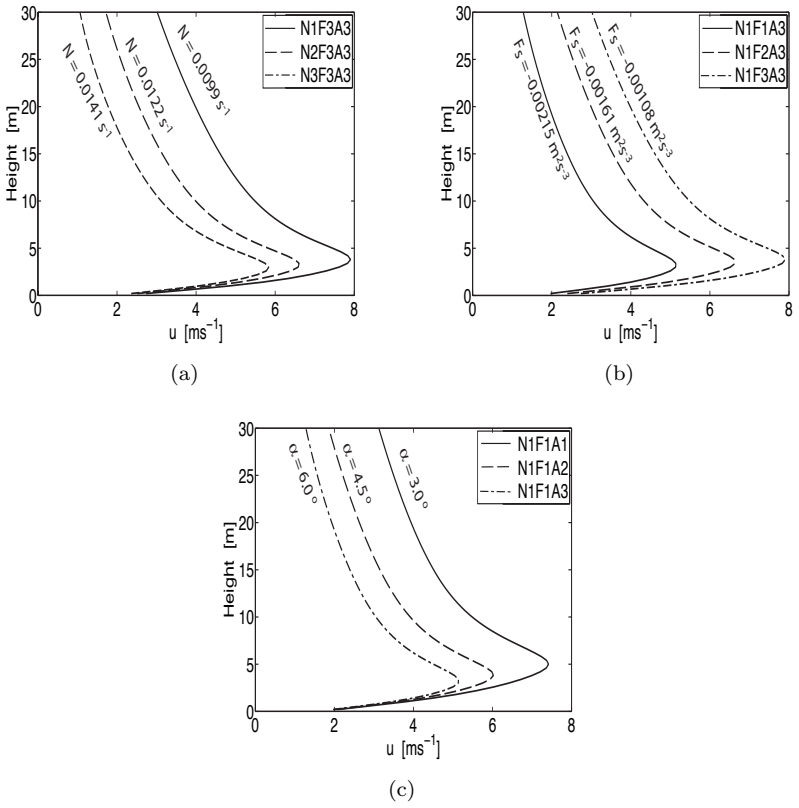

Figure 4.1. Vertical profiles of downslope velocity as functions of the background stratification (a), the surface buoyancy flux (b), and the slope angle (c). Figures show only the lowest 30 m of the vertical domain (51 m). Profiles have been averaged over the last oscillation period, see text for details.

the flow. Figure 4.1(b) shows the simulated profiles of downslope velocity as functions of the surface buoyancy flux. A doubling of F_s (simulations N1F1A3 and N1F3A3) leads to an approximate doubling of u_m. Changing F_s also influences z_j. According to the Prandtl model, $z_j \propto F_s/b_s$, provided the ambient stratification and slope angle remain constant, e.g. (4.10). As will be shown below, increasing F_s leads to an increase in the ratio F_s/b_s, and consequently z_j increases for larger F_s.

Next we turn to the effect of the slope angle. According to (4.10), the wind maximum height should decrease for larger α, which is confirmed by our numerical results, e.g. Figure 4.1(c). On the other hand, (4.12) states that the magnitude of the wind maximum does not depend on α. Prandtl argued that

for ever smaller slopes, the downslope component of buoyancy becomes smaller, and that the opposing momentum flux divergence is reduced accordingly. Rao and Snodgrass (1981) gave a similar argument for explaining their numerical results, which showed that the maximum downslope velocity was not very sensitive to the slope angle. However, this argument cannot be applied to our numerical results, which clearly show that $u_m \propto 1/\alpha$. The explanation for the difference between our numerical results and those of Prandtl, and Rao and Snodgrass (1981) is that we prescribe a constant surface buoyancy flux, and not the surface buoyancy. As will be shown below, the buoyancy increases with decreasing α, hence u_m increases accordingly. Our result can also be obtained by inspecting Equation (4.2), which states that $uN^2 \sin\alpha = -\mathrm{d}F/\mathrm{d}z$. The right hand side can be approximated by $-\mathrm{d}F/\mathrm{d}z \simeq -\Delta F/\Delta z \simeq F_s/z_{\mathrm{inv}}$, where z_{inv} is the boundary layer depth. Provided F_s, N, and z_{inv} are constant, the downslope velocity must be $u \propto (\sin\alpha)^{-1}$.

The buoyancy profiles are plotted in Figure 4.2. Whereas all the profiles are practically identical for $z \gtrsim 25$ m, larger differences between the simulated buoyancy values are found near the surface. The surface buoyancy can be deduced from (4.9), e.g. on a rearranged form: $b_s \propto F_s\,(N \sin\alpha)^{-1/2}$ (the constant Prandtl number and K_b are here included in a proportionality constant). Figure 4.2 confirms that b_s decreases for larger N and α, increases for larger F_s, and that F_s is responsible for the largest changes in b_s.
All buoyancy profiles furthermore show for $z \lesssim 2.5$ a linear decrease with respect to height, and they have an inflection point at the height of the wind maximum. This is clearly seen for simulation N1F1A1, whereas the other simulations have a less pronounced inflection point. According to the Prandtl model, however, this inflection point should be further aloft; from (4.4) it is seen that the inflection point is at the height where u changes sign, e.g. at $4z_j$. A similar result is found for the GO model. The difference between the analytical models and the numerical results is caused by the simplified balance in the buoyancy equation (4.4), and the use of a simple K_b. The Prandtl and GO buoyancy profile are therefore expected to differ from our numerical results. This is further examined in Section 4.4.
The temperature gradient near a wind maximum has also been studied by Cuxart and Jiménez (2007). They performed an LES study of the nocturnal jets observed over a horizontal surface, and found in both the observations and the LES results a change in the temperature gradient at the height of the wind maximum. However, they did not observe an inflection point, but rather a transition from a strong gradient to a weaker gradient.

Turbulence fluxes

Next we turn to the momentum flux τ, see Figure 4.3. From the Prandtl model we have $\tau = -K_m\,(\mathrm{d}u/\mathrm{d}z)$. Below the wind maximum, the velocity gradient is positive, hence τ should be negative. The same feature is observed

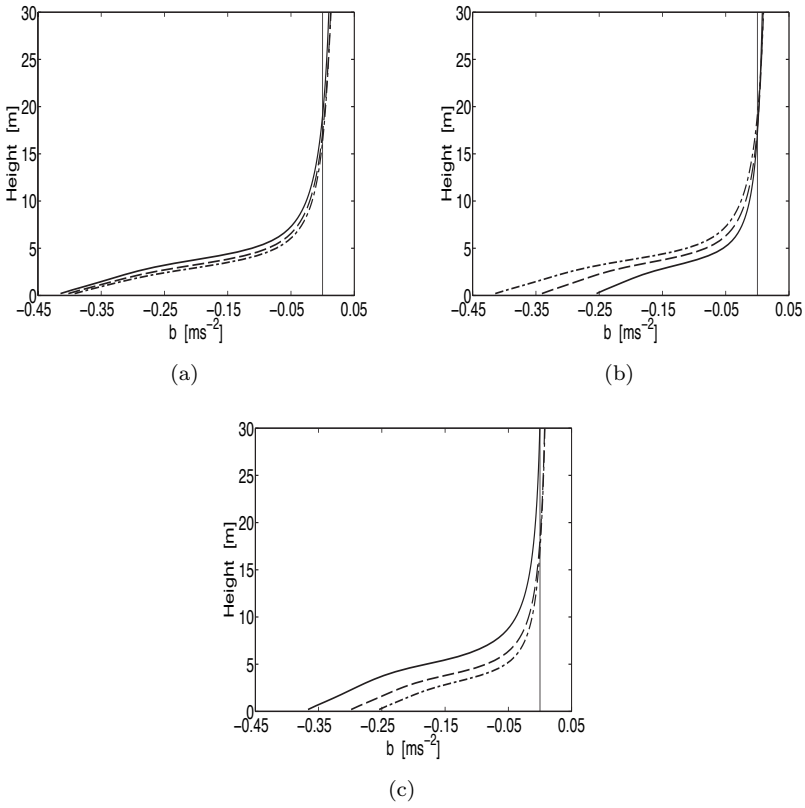

Figure 4.2. As Figure 4.1, but for the buoyancy.

in the numerical results. The momentum flux goes to zero at z_j, and above it increase until $z \sim 15 - 25$ m. Further aloft, the momentum flux slowly approaches zero. The Prandtl model predicts a more rapid decrease in τ above the wind maximum due to a larger velocity gradient. This (Prandtl) gradient can be estimated from (4.6), which indicates a return flow at $4z_j$. As was noted in Chapter 3, the LES results only show a return flow far above the wind maximum, and consequently the simulated momentum flux is positive in a larger region above z_j compared to the Prandtl prediction.

The profiles of the buoyancy flux F are shown in Figure 4.4. They decrease monotonically from F_s at the surface to zero. The decrease in F is the largest near the surface, and is smaller further aloft, i.e. the buoyancy flux profiles curve with respect to height. From Figure 4.4(a) it is seen that this curvature depends foremost on the background stratification. Such a curvature in F was also noted in the numerical results by Denby (1999), and it is furthermore a

feature of the Prandtl model. The latter is readily obtained by differentiating (4.5) with respect to z, e.g. $F = -K_b \mathrm{d}b/\mathrm{d}z$. However, in the analytical model, F changes sign at the height where u becomes negative, see (4.2). The analytical velocity profile changes sign at a much lower altitude compared to the LES results, likely explaining why the LES profiles of F do not change sign. The curvature in F is in contrast to the linear decrease found in the SBL over horizontal surfaces (e.g. Nieuwstadt, 1984). The physical explanation behind this difference can be found in Equation (4.2), i.e. katabatic winds are responsible for a downslope advection of warm air. For the plane SBL, however, Nieuwstadt (1984) assumed a horizontally homogeneous buoyancy field, and thus the horizontal advection terms in the buoyancy equation could be neglected.

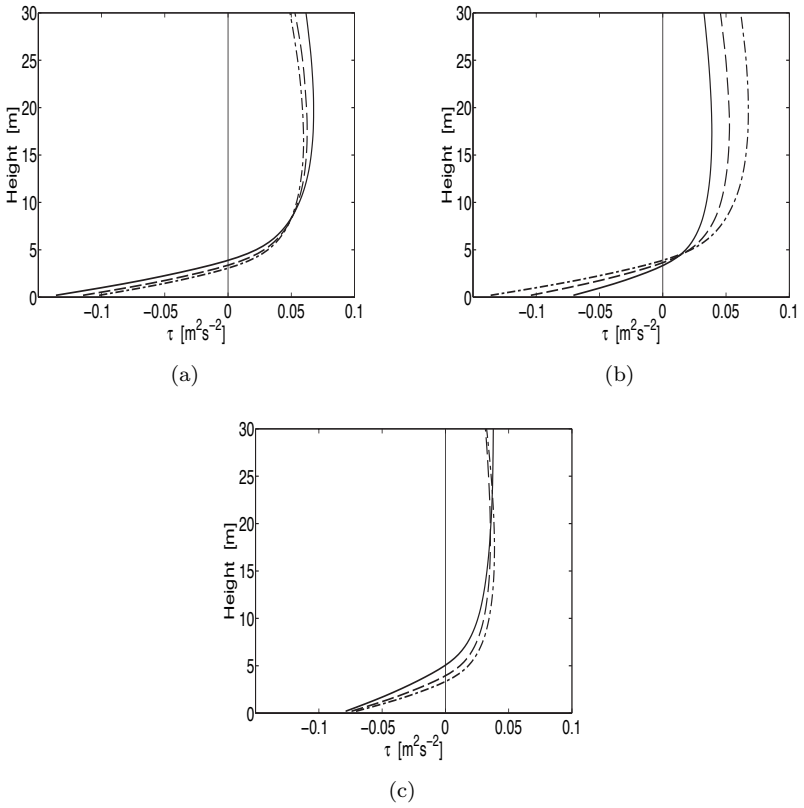

Figure 4.3. As Figure 4.1, but for the momentum flux.

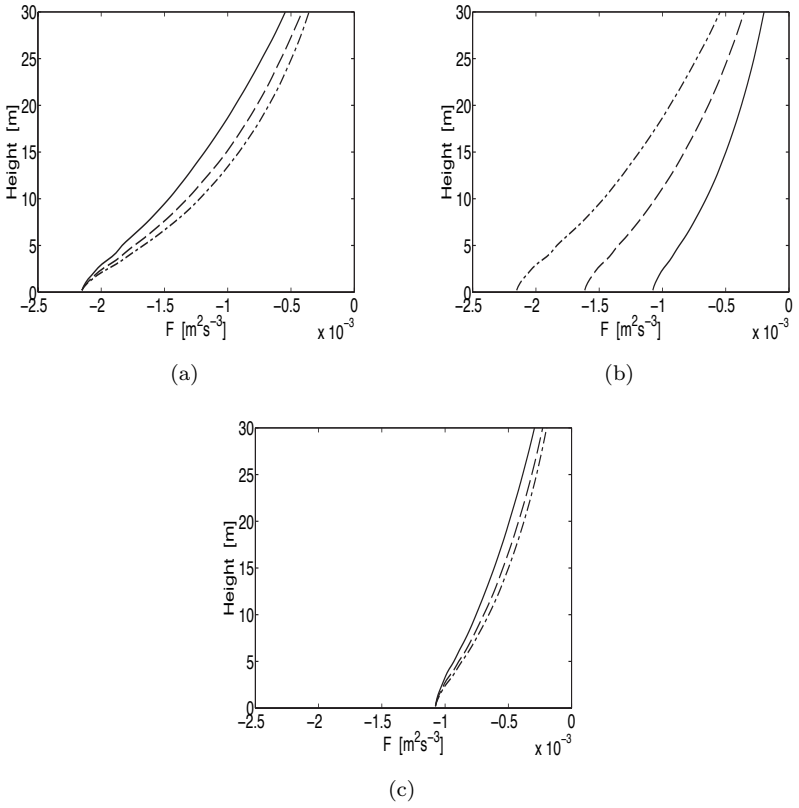

Figure 4.4. As Figure 4.1, but for the buoyancy flux.

TKE budget

The mean profiles of slope winds have in several measurement campaigns been measured at multiple levels, whereas second-order moments are often only measured at 1 or 2 levels. Numerical simulations, on the other hand, may provide more detailed profiles of higher-order moments.
The benefit of LES over closure models (see e.g. Chapter 3), is that it provides direct estimates of the TKE budget of the resolved motion. The TKE budget[5]

[5]We have discovered, in retrospect, that the modelled shear and buoyancy terms do not include along-flow components of turbulent fluxes. These fluxes, which are proportional to $\sin\alpha$, are in this study probably small, and it is therefore not likely that they discredit the results.

of the *resolved motions* is given in symbolic notation by

$$\frac{\partial E}{\partial t} = MP + BP + TR + PR + DIS - \mathcal{R},$$

where E is the resolved TKE, MP and BP are, respectively, the shear and buoyancy production terms, TR and PR are the transport and pressure redistribution terms, respectively, and DIS is the TKE viscous dissipation rate. In the model code, various assumptions are made in the evaluation of these terms, and they therefore do not exactly balance. The imbalance is represented by $\mathcal{R}$. A formal derivation of the TKE budget is found in Stull (1988), and Sagaut (1998) describes how this budget is evaluated in LES.

Figure 4.5 shows the terms in the TKE budgets of four simulations, which illustrate how the TKE budgets are influenced by changes in F_s, N, and α. Since the profiles have reached a steady-state, the temporal change in E is small, and thus not shown. We first consider general characteristics of the budgets before turning to the differences between the simulations.

LES of turbulent flow in the surface region is problematic since the eddy scales very close to the surface are smaller than the filter scales, i.e. the resolved TKE becomes smaller than the SFS TKE, see also the previous chapter. Starting at the surface, Figure 4.5 shows that all terms in the resolved TKE budget tend to zero as $z \to 0$. The profiles of shear production and turbulence dissipation increase with height up to $z_j/2$ where they show a maximum. A second maximum in the shear production and turbulence dissipation profiles is observed above the wind maximum.

All simulations show that the shear production is roughly balanced by the turbulence dissipation, and that the buoyancy is a small sink term. Below the wind maximum, the pressure redistribution term is a secondary production term, whereas the turbulence transport term removes TKE. At z_j, the shear and the pressure redistribution terms vanish, and the transport term is positive and balances the turbulence dissipation (due to plotting reasons this is not shown well for N1F1A1). The turbulence transport term TR remains positive in a small region immediately above z_j, and further aloft, TR attains a small negative value.

Skyllingstad (2003) also presented LES results of TKE budgets for katabatic winds (see also introduction Chapter 3). Similar to our results, he found shear to be the largest production term, and it was mainly balanced by the turbulence dissipation. Skyllingstad (2003) did not show the transport and pressure redistribution terms separately, but rather combined them. This sum, e.g. $TR + PR$, is the total turbulent transport of TKE, which we here label TP. He found the sum to be positive below z_j, and negative above. We find similar results for TP. However, there are also differences between his and our results. Skyllingstad's shear production term did not go to zero at the height of the wind maximum, which is unexpected since the velocity gradient vanishes at z_j. He attributed this result to the effects of averaging in the downstream direction

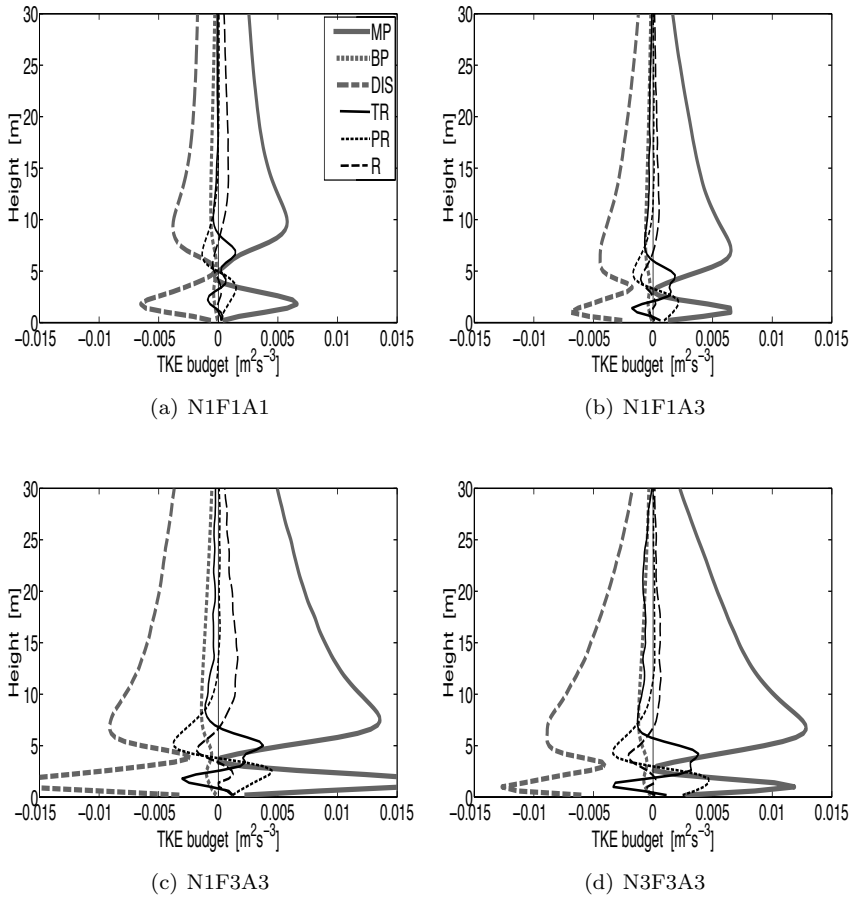

(a) N1F1A1

(b) N1F1A3

(c) N1F3A3

(d) N3F3A3

Figure 4.5. TKE budgets of the resolved motions.

(note that he did not use periodic boundary conditions as we do, i.e. his results can not be considered one-dimensional), and to the model resolution.
As was described in Section 1.4.1, the vanishing of the shear production at z_j can in some closure models (depending on the order of closure) result in a decoupling of the katabatic flow around the wind maximum. Using a second-order closure model, Denby (1999) studied the total turbulent transport of TKE, *TP*, and found that it was important around z_j. However, for a moderately steep slope (6 °), his maximum (positive) transport term was significantly larger than in our study. For example, Denby's maximum *TP* was equal in magnitude to the maximum elevated *MP* term. In our study, the maximum *TR* at

z_j (remember, pressure redistribution is zero) is only $\sim 30\,\%$ of the maximum shear production. There are several possible explanations for the discrepancies between Denby's and our results: At the height of the wind maximum, it is possible that the turbulent eddies are smaller than the filter width, i.e. our model may not be capable of explicitly resolving the motions of the small eddies near z_j. On the other hand, one of the assumptions in Denby's parameterization of the *TP* term is debatable. He assumed that the pressure redistribution term could be either ignored, or parameterized on a form similar to the turbulence transport term. However, our model results have shown that *TR* and *PR* can attain equal magnitudes, and that their vertical profiles are different, hence questioning the assumption that these two terms can be parameterized as one term.

Next we turn to the differences between the simulations. Figures 4.5(a,b) show that the largest terms in the TKE budget are not sensitive to a doubling of the slope angle. Although case N1F1A1 has a larger wind maximum compared to N1F1A3, z_j was also larger (Figure 4.1c), hence the shear production is practically the same in both cases. The turbulence dissipation term is also only slightly sensitive to changes in α, N1F1A3 shows a bit larger value at z_j. The magnitude of the turbulence transport term *TR*, and to some degree the pressure redistribution term *PR*, is slightly increased by a doubling of the slop angle. The increase in TR indicates that there is a larger turbulence mixing across the wind maximum for steeper slopes.

The budgets are more sensitive to changes in F_s. The surface buoyancy flux determines the buoyancy destruction of TKE at the surface. Figures 4.5(b,c) show that by doubling F_s the buoyancy term *BP* increases roughly by a factor 2. Simulation N1F3A3 further shows that all the remaining terms in the TKE budget increase in magnitude compared to simulation N1F1A3. The largest changes are found in the *MP* and *DIS* profiles. The local maxima of the latter two profiles at $z \approx 7$ m increase by a factor 2 compared to simulation N1F1A3. The residual $\mathcal{R}$ also increases, probably caused by increasing numerical errors in the evaluation of the mechanical production term *MP*.

A change in the background stratification produces only small changes to the TKE budget. The largest differences between simulations N1F3A3 and N3F3A3 are near the surface, see Figures 4.5(c) and (d). By increasing N, the velocity gradient near the surface is reduced, (Figure 4.1a), whereas the momentum flux (Figure 4.3a) is only slightly changed, hence the *MP* term, which is the product of the momentum flux and the velocity gradient, is reduced below the wind maximum. As a result of the smaller shear production, the turbulence dissipation term also becomes smaller near the surface.

The Prandtl number

In the analytical models introduced in Section 4.2, the (turbulent) Prandtl number is a constant but arbitrary number, which can be used to fit the mod-

elled profiles of downslope velocity and buoyancy to e.g. observations. On the other hand, the observations should dictate the value of Pr. The Prandtl number in the horizontal boundary layer can be derived from observations by considering the relation

$$Pr = \frac{\phi_b}{\phi_m}. \tag{4.20}$$

$\phi_m(z/L)$ and $\phi_b(z/L)$ are the non-dimensional gradients of momentum and buoyancy, respectively, and follow from the Monin-Obukhov (MO) theory (e.g. Foken, 2006). They are valid in the surface layer, and are functions of the non-dimensional height z/L, where the (local) MO length L (e.g. Stull, 1988) depends on the stability of the atmosphere.

Data sets from several measurement campaigns have been used to study the non-dimensional gradients. For example, for the SBL Businger *et al.* (1971) found $\phi_m = 1 + 4.7z/L$ and $\phi_b = 0.74 + 4.7z/L$, yielding 0.74 as a lower limit for the Prandtl number, and 1 for very stable conditions. Some studies have shown that these relatively simple formulations should not be applied to the very stably stratified boundary layer. Beljaars and Holtslag (1991) proposed more complex parameterizations of the non-dimensional gradients, for which the ratio ϕ_b/ϕ_m increased with increasing z/L. Their formulations have gained support from e.g. Foken (1997), and Hartogenisis and De Bruin (2005), whereas Howell and Sun (1999) found support for both the simple and the more complex functions.

In the SBL, which typically exhibits a low-level jet (e.g. katabatic or inertial jet), the MO theory should not be applied if L is larger than the jet height (see e.g. Zilitinkevich and Esau, 2007; Grisogono *et al.*, 2007, and references herein). Instead of relating the Prandtl number to z/L, it can be derived from the turbulence exchange coefficients of momentum and buoyancy

$$Pr = \frac{K_m}{K_b} = \frac{\tau / \left(\frac{\partial u}{\partial z}\right)}{F / \left(\frac{\partial b}{\partial z}\right)}. \tag{4.21}$$

These exchange coefficients are frequently investigated in terms of the gradients of corresponding mean variables, which may be combined into the gradient Richardson number as $Ri_g = (\partial b/\partial z) / (\partial u/\partial z)^2$. Several measurement campaigns have shown that Pr increases with increasing Ri_g (e.g. Bange and Roth, 1999; Ohya, 2001; Strang and Fernando, 2001), which has also been found in observations of katabatic winds (e.g. Monti *et al.*, 2002). In a recent paper, Zilitinkevich *et al.* (2008) plotted Pr as a function of Ri_g using data from several measurement campaigns, supplemented by LES results, and found the empirical relation

$$Pr \approx 0.8 + 5Ri_g. \tag{4.22}$$

Using our LES results of katabatic winds, we here explore how the Prandtl number of the *resolved motions* varies with height and with Ri_g. Figure 4.6(a)

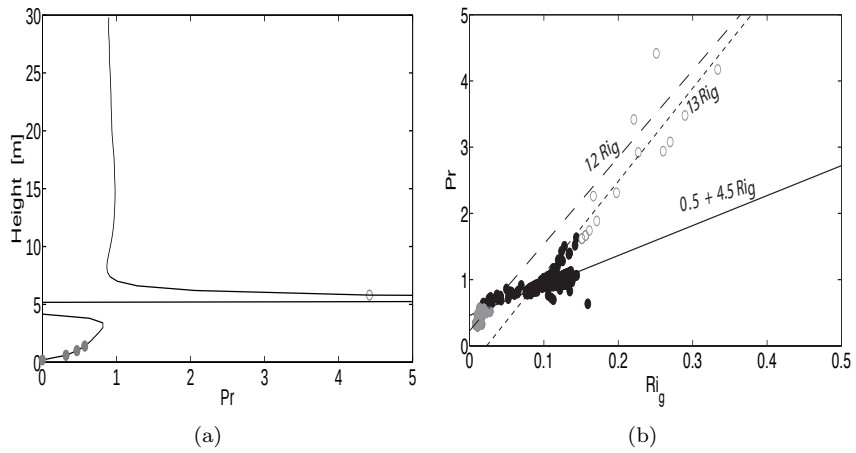

(a) (b)

Figure 4.6. (a) The Prandtl number Pr as a function of height (simulation N1F1A1), and (b) as a function of the gradient Richardson number Ri_g, values based on the resolved motions. Filled grey circles denote values obtained below $z \leq 0.4 z_j$, whereas open grey circles are the Pr values at the two grid levels immediately above z_j. The black filled circles are the remaining Pr values.

shows Pr as a function of height. Only one simulation (N1F1A1) is shown, the other simulations yield similar results. Near the surface, which is where the SFS model plays an important role (see Chapter 3), the resolved fluxes of momentum are apparently smaller than the buoyancy fluxes, hence the low values for Pr. The Prandtl numbers derived from grid levels below $\sim 40\%$ of the wind maximum are denoted by filled circles. Closer to the wind maximum, e.g. $z \lessapprox 5\,\mathrm{m}$, the Prandtl number is close to unity. At the wind maximum height, the velocity gradient vanishes, and consequently K_m and Pr tend to infinitely large values. Immediately above z_j, the large values for Pr (denoted by open circles) are due to a small velocity gradient. It is therefore unlikely that they have physical meaning. Lastly, we find that the Prandtl number is close to unity further aloft. Some of the other simulations show a slight increase in Pr near the inversion.

In Figure 4.6(b), the Prandtl number is plotted as a function of Ri_g. We distinguish between Pr close to the surface (grey filled circles), immediately above z_j (open grey circles), and the remaining grid levels (filled black circles). The Prandtl numbers are calculated on grid levels below the height at which the buoyancy becomes positive, e.g. for $z|_{b<0}$. Linear regressions of the Prandtl numbers' dependence on Ri_g have been included in the figure.
Close to the surface, Pr increases as $\sim 12 Ri_g$. This result may not be reliable due to the fact that the SFS model plays a paramount role close to the surface.

A similar dependency of Pr on Ri_g is found immediately above z_j, and it is likely that these Prandtl numbers are inaccurate due to the small velocity gradient. The only way to determine how Pr varies with Ri_g close to the surface and immediately above z_j is to use a (much) higher numerical resolution.
In the bulk of the boundary layer, most points follow the line $Pr \approx 0.5 + 4.5 Ri_g$. This linear regression is close to (4.22), except our lower limit is a bit smaller. From (4.22) one derives the minimum value $Pr = 0.8$, which is similar to the value Businger *et al.* (1971) found for the near-neutral boundary layer. In our numerical study, the low Prandtl numbers are derived close to $z \approx 0.4 z_j$ (lower limit of what we characterized as the bulk of the boundary layer), or close to the inversion. In these regions, the momentum fluxes are smaller than the buoyancy fluxes, hence the Prandtl number of the (resolved) motions decreases.
Most of the Prandtl numbers displayed in Figures 4.6(a,b) are close to unity, whereas larger values have been suggested by some observations (e.g. Zilitinkevich *et al.*, 2008). However, turbulent flows are frequently subject to multiple forcings that we have not attempted to model (e.g. inhomogeneity, non-steady state), which hampers the comparison of LES results to observations. On the other hand, other LES studies have also found $Pr \lesssim 1$ (e.g. Beare *et al.*, 2006; Basu and Porté-Agel, 2006), which might support our numerical results.

Several papers have noted that there may be a spurious correlation (also called self-correlation) between the Prandtl and the gradient Richardson numbers (e.g. Grachev *et al.*, 2007; Baas *et al.*, 2006; Anderson, 2009) due to the fact that the vertical gradients of buoyancy and velocity are used to calculate both Pr and Ri_g. Similarly, a self-correlation between Pr and z/L is expected since the MO length is a function of the momentum and buoyancy fluxes, which are also used to calculate Pr. However, as argued by Zilitinkevich *et al.* (2008), the relation between the Prandtl number and the gradient Richardson number does not suffer from the drawback of a spurious correlation for low Ri_g. Since our Ri_g are typically smaller than 0.25, we do not expect self-correlation to diminish the credibility of our results.

4.4 A comparison of analytical and numerical results

In the previous section, we used the Prandtl solution to explain several of our LES results, and also pointed out some differences between the analytical and numerical results. In this section, these differences are examined by comparing the LES profiles of velocity and buoyancy to the Prandtl and GO solutions. Below we only show simulation N1A1F1, the other simulations give qualitatively similar results.
We run the analytical models using the surface buoyancy derived from the LES data, e.g. $b_s = 0.40\,\mathrm{ms}^{-2}$. The background stratification is $N = 0.0099\ \mathrm{s}^{-1}$,

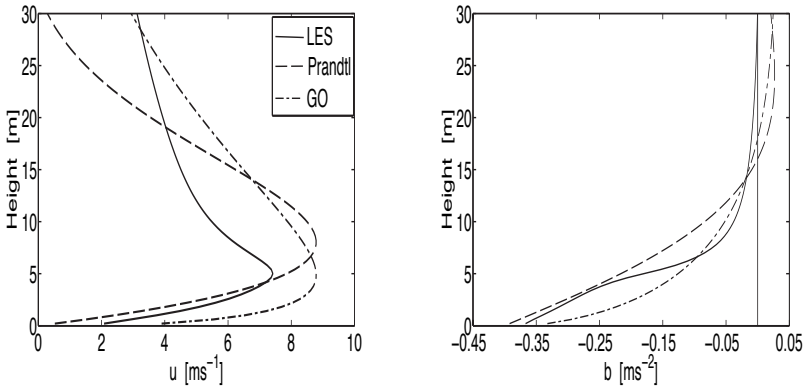

Figure 4.7. LES (simulation N1F1A1) and analytical profiles of downslope velocity (a) and buoyancy (b).

and the slope angle is $\alpha = 3.0\,^{\circ}$. The Prandtl number and the (height-dependent) buoyancy exchange coefficient, which depend on the flow, are normally used to fit the analytical models to observations (e.g. GO01a,b). Here we choose these variables such that the differences between the analytical and LES results are minimized (e.g. determined by trial and error). In the Prandtl model we use $K_b = 0.02\,\mathrm{m^2 s^{-1}}$, and in the GO model we use, similar to GO01b, $K_b(z) = cz\exp\left[-0.5(z/h)^2\right]$, where c is a constant, $h = 39\,\mathrm{m}$, and $\max(K_b) = 0.125\,\mathrm{m^2 s^{-1}}$. Lastly, the Prandtl number is $Pr = 2$ in both analytical models.

Figures 4.7(a,b) present the LES profiles of, respectively, the downslope velocity and the buoyancy for simulation N1F1A1 together with the analytical Prandtl and GO solutions. Near the surface, the LES and Prandtl profiles show similar velocity gradients, whereas the gradient of the GO velocity profile is steeper. Due to this large gradient, the wind maximum height of the GO model corresponds well with that derived from the LES results, while the Prandtl model yields a larger value for z_j. Both analytical models show a wind maximum that is too large compared to the LES results. Moreover, the sharpness of the wind maximum is a notable difference between the analytical and numerical velocity profiles. Above z_j, the GO model predicts a slower decrease in u than the Prandtl model, which is in line with the LES results.

There are several reasons for the differences between the three velocity profiles. First, in the downslope momentum equation (4.1), the acceleration by buoyancy is retard by the vertical momentum flux divergence (the only term retained from the advection terms), whereas diffusion is neglected.

Skyllingstad (2003) showed that below the wind maximum, the diffusion term is larger than the advection term, hence neglecting the diffusion term in (4.1) is a limitation in the analytical models. Second, in the subsequent derivation, Equation (4.3) and onward, the advection terms in the momentum and buoyancy equations are modelled as diffusion terms by applying first-order closure. The exchange coefficients K_m and K_b are related to each other through the constant Prandtl number. In light of the previous section, we did not consider $Pr > 2$. However, by choosing a larger value for the Prandtl number, the downslope velocity would decrease, e.g. Equation (4.6). Third, K_b depends on height. Only the GO model accommodates such a height-dependence, which is the reason why it predicts a lower z_j compared to the Prandtl model. Lastly, K_b could have been chosen such that the analytical velocity profiles would have been in better agreement with the LES data, but the comparison of the buoyancy profiles would have been influenced in a negative sense.
The LES and analytically derived buoyancy profiles are shown in Figure 4.7(b), where a quantitatively good agreement between them may be noted. At $z = 0$ (0.2 m below lowest model level), all profiles attain the same value, but due to steep gradients, they diverge immediately above the surface. The Prandtl and LES profiles agree up to $\sim z_j$, whereas the GO profile is in better agreement with the LES results further aloft.

4.5 An analysis of numerical and analytical flow characteristics

In Section 1.4.1 we gave a short review on how meso-scale modelling of katabatic flows has developed over the last decades. These models are capable of using real atmospheric forcings and realistic topography. On the other hand, one disadvantage is the need for parameterizations of the planetary boundary layer (with increased resolution this parameterization may in the future become redundant) and the surface layer (see e.g. Zilitinkevich and Esau, 2007, and references herein for more elaborated comments on the problems concerning the surface parameterizations used in meso-scale models). For example, the regional climate model RACMO[6] parameterizes the surface buoyancy flux based on the velocity at the lowest grid level, the temperature difference between the surface and the lowest grid level, and a transfer coefficient that depends on the MO length L (e.g. White, 2003). LES, on the other hand, does not rely on such parameterizations, but is rather a tool with which one can study the quality of parameterizations in meso-scale models, and derive new ones. In this section, we use our LES results to study how F_s can be derived from Equations (4.11) and (4.14), and their GO counterparts. In the next sections, these relations

[6]Regional Atmospheric Climate MOdel

Table 4.2. Regression coefficients of the Prandtl relations (4.11), (4.13) and (4.14), as well as the GO and LES counterparts. In the analytical models $Pr = 2$.

Relation	(4.11)	(4.13)	(4.14)
LES	$c_1^{\mathrm{LES}} = 0.96$	$c_2^{\mathrm{LES}} = 5.10$	$c_3^{\mathrm{LES}} = 0.18$
Prandtl	$c_1^{\mathrm{Pr}} = 2.22$	$c_2^{\mathrm{Pr}} = 4.38$	$c_3^{\mathrm{Pr}} = 0.51$
GO	$c_1^{\mathrm{GO}} = 1.72$	$c_2^{\mathrm{GO}} = 4.38$	$c_3^{\mathrm{GO}} = 0.39$

are compared to observations and to results from other numerical models.

Equation (4.11) suggests a linear relation for estimating F_s based on the slope angle, the background stratification, the wind maximum height, and the surface buoyancy. Figure 4.8(a) shows the LES results with a linear regression, and the linear Prandtl and GO relations. Note that the LES input and output parameters are plotted along the first and second axes, respectively, and that we only use absolute values. The numerical results fit nicely onto a straight line. The linear regression coefficient is $c_1^{\mathrm{LES}} = 0.96$, which is the LES counterpart of the constants c_1^{Pr} and c_1^{GO} from the Prandtl (4.11) and GO (4.17) models, respectively. The latter two have the values 2.22 (Prandtl) and 1.72 (GO), where we have assumed $Pr = 2$, which was the value used in the previous section. These coefficients are summarized in Table 4.2.

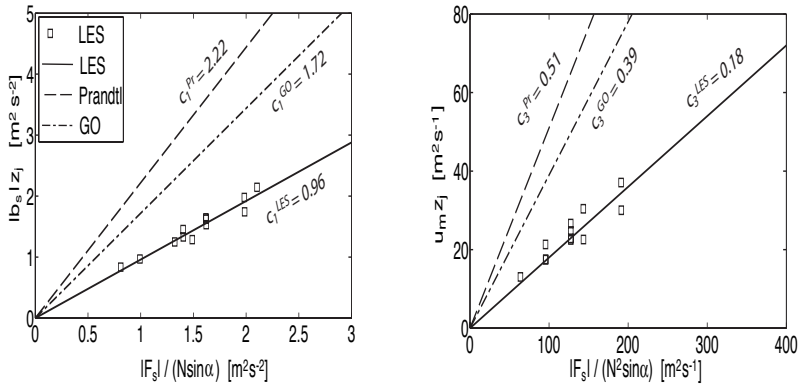

(a) (b)

Figure 4.8. Prandtl relations (4.11) (a) and (4.14) (b) with GO counterparts (4.17, 4.19) and LES results (squares). The linear regression based on the LES results is plotted as a solid line. The linear regression coefficient of the LES results and the coefficients from the Prandtl and GO models are summarized in Table 4.2.

Equation (4.14) provides an optional way of estimating the surface buoyancy flux. In contrast to the discussion above, the latter relation requires information on the magnitude of the wind maximum, but not the surface buoyancy. The LES results fall onto a line with coefficient $c_3^{\mathrm{LES}} = 0.18$, see Figure 4.8(b). From the Prandtl and GO relations one derives the coefficients $c_3^{\mathrm{Pr}} = 0.51$ and $c_3^{\mathrm{GO}} = 0.39$, respectively.
Equation (4.14) was derived from (4.11) by using (4.13). The latter states that the ratio of the surface buoyancy to the wind maximum, $|b_s|/u_m$, is determined by the stability of the ambient atmosphere N. The LES results show larger ratios $|b_s|/u_m$ compared to the analytical models, see Figure 4.9. The linear regression coefficient inferred from the LES results is $c_2^{\mathrm{LES}} = 5.10$, whereas its Prandtl and GO counterparts are $c_2^{\mathrm{Pr}} = c_2^{\mathrm{GO}} = 4.38$.
Figures 4.8 and 4.9 show that the analytical models deviate from the LES results. This difference can be minimized by optimizing the values for c_i^{Pr} and c_i^{GO}. We noted in Section 4.2 that these constants have several degrees of freedom, i.e. they depend on the Prandtl number and indirectly on the buoyancy exchange coefficient. Since these parameters can be tuned to fit observations (in this case LES data), it is permissible to optimize c_i^{Pr} and c_i^{GO} such that the Prandtl and GO models coincide with the LES results.
It should be noted that the LES results used to verify the linear Prandtl relations are from a set of simulations whose input domain is narrow. It is therefore possible that the linearity of the relations will not hold if the values of the input parameters change substantially. In a LES study of anabatic flows, Schumann (1990) explored how the maximum wind speed and inversion height varied with a slope angle ranging from 2 to 90 °. He found that the magnitude of the wind maximum decreased exponentially when α increased from 2 to 30 °, but an increase in the wind maximum was noted when α increased beyond 45 °. Our results may therefore only be appropriate for a small input parameter domain. However, we have chosen to regard a realistic parameter space, i.e. the observations presented in the next section are within the input domain that we have applied in this chapter.

4.6 Comparison with observations

The linear relations (4.11) and (4.14) can be used to estimate the surface buoyancy flux from mean quantities, and can thus be regarded as parameterization relations. Above we presented LES parameterizations[7] of these equations, and found encouraging results. However, these parameterizations should also be verified using observational data. Here we compare them to the observations from the Pasterze glacier, Austria, and the Vatnajökull glacier, Iceland (the same observations were used in the model validation presented in the previous

[7] Terminology remark: the term "LES parameterization" does not refer to parameterizations in the numerical model, but to the linear regressions derived from the LES results.

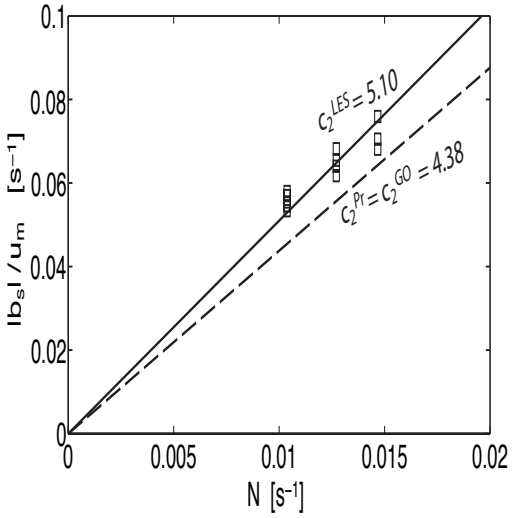

Figure 4.9. LES results verified against the Prandtl relation (4.13), legends as in Figure 4.8. The GO relation (4.18) is identical to its Prandtl counterpart.

chapter). Whereas the Vatnajökull observations provide data on velocity, temperature, and the background stratification, the Pasterze observations also included an estimate of the surface buoyancy flux. The reader is referred to Chapter 3 for details on the measurement sites and data treatment, here we only summarize which observations were selected for comparison with the proposed parameterizations.

We consider balloon soundings that provided an unambiguous background stratification, and the mast profiles that were performed within an half-hour interval of the sounding. The velocity profiles, derived from the mast measurements, are first smoothened using a quadratic interpolation, and subsequently used to estimate u_m and z_j. We require that the wind maximum is below the highest mast level, and discard the velocity profile if the wind direction at the lowest measurement level is not within 20 degrees of the fall line. For the Pasterze data, this criterion could not be satisfied at the uppermost wind vane level (wind direction measured at two levels). At Vatnajökull, on the other hand, this criterion was practically always fulfilled at all mast levels.

Supplementary to our observations, we also consider data from Zhong and Whiteman (2004)[8] (hereafter ZW04), who captured the profiles of velocity and buoyancy in a katabatic flow over a low-angle slope. During the measurement campaign, which took place in October 2000 in the Salt Lake Valley, Utah,

[8]Results are discussed in more details in Whiteman and Zhong (2008).

U.S., observations were obtained using tethered balloon soundings at multiple locations, and provide information on u_m, z_j, and b_s, but unfortunately not the surface buoyancy flux.

In Figure 4.10(a) we validate relation (4.11) using the Pasterze observa-

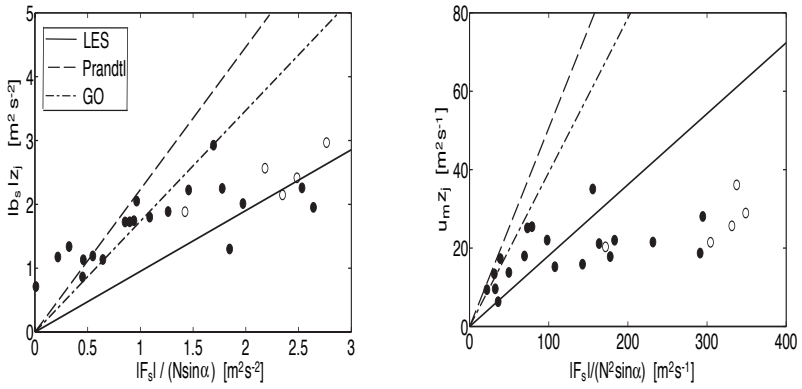

(a) (b)

Figure 4.10. Comparison of analytical and LES relations with observations from Pasterze: (a) Equation (4.11), (b) Equation (4.14). Observations with small N are shown as open circles, see text for details.

tions. The figure includes the parameterizations based on the LES, Prandtl, and GO results. The observations confirm that $|b_s|z_j$ increases for larger $|F_s|(N\sin\alpha)^{-1}$, and the figure indicates that the analytical models yield a better estimate for $|b_s|z_j$ than the LES parameterization does. This result may seem surprising since LES includes more terms in the governing equations than the analytical models do. However, the result is not unreasonable because we use a Prandtl number and height-dependent buoyancy exchange coefficient very similar to what GO01a used when fitting the analytical models to the Pasterze observations. The figure furthermore shows some discrepancies between the observational data, and the analytical and numerical model results. First, the observations indicate that the increase in $|b_s|z_j$ with $|F_s|(N\sin\alpha)^{-1}$ is slower compared to the parameterizations, implying that the constants $c_1^{\mathrm{LES,Pr,GO}}$ are too large. Second, the observations do not fall onto one line, but rather show a considerable amount of scatter. This may be caused by uncertainties in the observations, or low-quality data, which is discussed at the end of this section. Third, for small $|F_s|(N\sin\alpha)^{-1}$, the product $|b_s|z_j$ should according to (4.11) go to zero, but instead the observations approach a value $\sim 1\,\mathrm{m^2 s^{-2}}$. In these cases, we found N to be similar to in the remaining cases, whereas the observed F_s is small, typically an order 3 smaller than

the remaining observations. Despite a small F_s, the velocity profiles show clear wind maxima, which is likely due to uncertainties in the estimate of F_s. Whereas these uncertainties are discussed below, a limitation of (4.11) should also be pointed out. This relation is based on the assumption of a stationary flow. However, numerical simulations (e.g. Nappo and Rao, 1987) and observations (e.g. Whiteman and Zhong, 2008) have shown that katabatic winds can only be considered stationary for sufficiently large N. Observations for which N is small ($N < 0.0085$ s^{-1} or $\Gamma < 0.002$ Km^{-1}) are shown as open circles.

In Figure 4.10(b) the relation (4.14) is applied to the Pasterze data. The observations confirm that the product $u_m z_j$ increases with increasing $|F_s|(N^2 \sin\alpha)^{-1}$. The parameterizations based on the LES and analytical results work reasonably well for small ratios ($\lesssim 100\,\mathrm{m^2 s^{-1}}$), but for larger values ($100 - 300\,\mathrm{m^2 s^{-1}}$) the analytical expressions overestimate the product $u_m z_j$. For ratios $\gtrsim 300\,\mathrm{m^2 s^{-1}}$, the parameterizations compare poorly to the observations. As above, the observations are subject to uncertainties, and some observations are possibly of non-steady flow (indicated by open circles in the figure), for which this simple relation is not expected to hold.

The two LES parameterizations of (4.11) and (4.14) can be validated by comparing the observed surface buoyancy fluxes to the calculated ones. In Figure 4.11(a), the observed F_s is contrasted to the estimate derived from Equation (4.11). For small $|F_s|$ ($\leq 10^{-3}\,\mathrm{m^2 s^{-3}}$), the calculated values increase at the same rate as the observations. The results correlate reasonably well, the correlation coefficients being 0.7. For larger observed surface buoyancy fluxes, the agreement between the estimated and observed fluxes deteriorates. For observed $|F_s| \leq 1.5 \cdot 10^{-3}\,\mathrm{m^2 s^{-3}}$, the correlation coefficient decreases to 0.45, and is further reduced to 0.3 when including all observations. Moreover, for small $|F_s|$ a systematical offset from the indicated 1:1 line is noted. This offset is related to Figure 4.10(a); in the discussion of the latter we noted that typical katabatic velocity profiles existed even for (very) small F_s. This does to some degree discredit the relatively high correlation coefficient presented above.

In Figure 4.11(b), we compare the surface buoyancy flux calculated by the LES relation (4.14) to the observations. The data show a considerable amount of scatter with respect to the 1:1 line, and the correlation coefficient is small. We therefore conclude that (4.11) should be preferred to (4.14).

Lastly, we turn to relation (4.13). In addition to the Pasterze data, we tested this relation using observations from Vatnajökull and ZW04, see Figure 4.12. The Pasterze and Vatnajökull data hardly show any increasing trend in $|b_s|/u_m$ with increasing N, and the proposed parameterization does not fit the observations well. However, this somewhat dissatisfactory result may explain why the parameterization of (4.14) did not correlate well with the Pasterze observations. Equation (11), which is lent some credence from Figure 4.11(a), is combined with (4.13) to obtain (4.14), hence a non-satisfactory result in

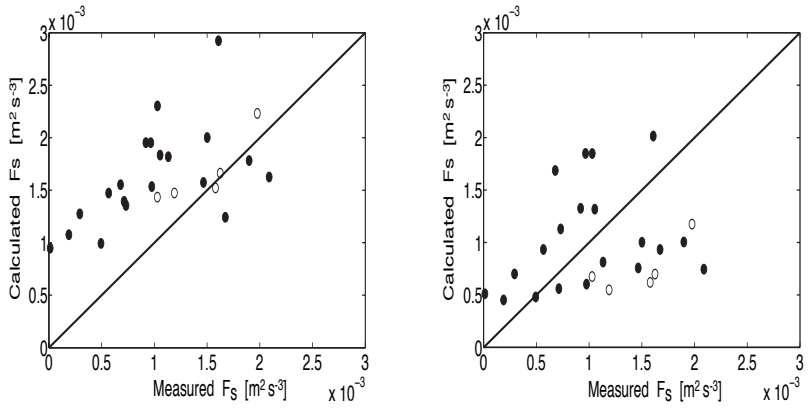

Figure 4.11. Comparison of observed to calculated surface buoyancy flux using Equations (4.11) (a) and (4.14) (b) to the Pasterze observations. The solid lines is the 1:1 relation, open circles denote observations with small N. All values are absolute.

Figure 4.12 is expected to influence the result in Figures 4.10(b) and 4.11(b).

Despite the discrepancies between the parameterizations and the Pasterze and Vatnajökull data, Figure 4.12 also shows some encouraging results. According to the ZW04 data, $|b_s|/u_m$ does increase with increasing N. It should be noted though, that the number of ZW04 observations is limited, hence it is not meaningful to calculate a correlation coefficient as we did for Figure 4.11.

The above comparisons of parameterizations to observations do not yield definitive results. The discrepancies may likely be caused by uncertainties in the observations or low-quality data. The largest uncertainty is probably related to how the surface buoyancy flux was obtained (Pasterze data only). The buoyancy fluxes were measured at two levels, and stored as half-hourly averaged values. F_s was obtained by linearly extrapolating these data to the surface. Uncertainties and/or errors in the half-hourly averaged observations are thus included (and probably increased) in the observed surface buoyancy flux. Second, the Pasterze glacier is a valley glacier. Its surrounding orography may induce a secondary circulation. Although we omitted velocity profiles for which the wind direction at the lowest measurement level was not within 20 degrees of the fall line, all remaining observations showed a veering with height. The change in wind direction with height increases the shear production of turbulence (e.g. Skyllingstad, 2003), and consequently influences the height and magnitude of the wind maximum, as well as the buoyancy in the layer between the surface and the wind maximum. Third,

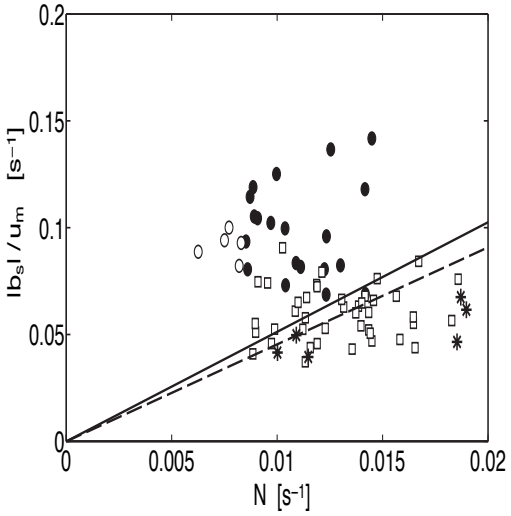

Figure 4.12. Comparison of Equation (4.13) with observations from Pasterze (circles), Vatnajökull (squares) and ZW04 (asterisk). The solid line is a linear regression of the LES results. The Prandtl and GO models (dashed) are identical.

in the previous chapter we pointed out that determining the background potential temperature from the balloon soundings is not straightforward, i.e. for both the Pasterze and Vatnajökull data there are uncertainties in N and b_s.

4.6.1 Comparison with other numerical model results

The comparison of (4.14) to the observations was rather poor, and was therefore rejected. The LES parameterization of (4.11), on the other hand, showed better agreement with the observations, but the correlation was weakened by the uncertainties and possible errors in the observational data. It is therefore reasonable to think that a comparison to more idealized data will yield better results. Here we consider the model results of ZW04 and Denby (1999) as idealized data, and test the LES parameterization of (4.11).
In their figure 3, ZW04 presented profiles of downslope velocity and potential temperature derived from balloon soundings at three different locations. We use the average of these soundings as input parameters. On Oct 2, at 21:30 LST, the stratification of the ambient atmosphere was $N = 0.011\,\mathrm{s}^{-1}$, the wind maximum height was at 12.8 m, and the surface buoyancy was -0.27 ms^{-2}. With a slope angle 1.58 °, Equation (4.11) yields the surface buoyancy flux

$F_s = -0.0011\,\mathrm{m^2 s^{-3}}$ (corresponding heat flux[9]: -33 $\mathrm{Wm^{-2}}$). This estimate is somewhat larger than the simulation results by Zhong and Whiteman (2008), who found $F_s \approx -0.0007\,\mathrm{m^2 s^{-3}}$; an assessment of our estimate is given at the end of this section.

On Oct 8, at 21:00 LST, the stratification was $N = 0.019\ \mathrm{s^{-1}}$, the wind maximum height was $z_j = 7.6\,\mathrm{m}$, and the surface buoyancy was $b_s = -0.26\,\mathrm{ms^{-2}}$. The estimated surface buoyancy flux is $F_s = -0.0011\,\mathrm{m^2 s^{-3}}$, which is larger than the value presented by Zhong and Whiteman (2008), $F_s = -0.0008\,\mathrm{m^2 s^{-3}}$. We must stress that our input parameters are derived from figures in ZW04, hence these values may be uncertain.

In the previous section, we presented instantaneous (i.e. no time averaging) observations from Pasterze. By averaging Pasterze data over a 24 h period, Denby (1999) obtained a more idealized data set to which he compared his numerical simulation. Based on his idealized data, we here estimate F_s using (4.11). From his Figure 3 and Table 4, we get $N = 0.01\,\mathrm{s^{-1}}, b_s = 0.43\,\mathrm{ms^{-2}}$, $z_j = 4\,\mathrm{m}$, and $\alpha = 4\,^{\mathrm{o}}$, yielding the estimate $F_s = -0.0013\,\mathrm{m^2 s^{-3}}$. The result compares fairly well to Denby's simulation result, e.g. $F_s = -0.0017\,\mathrm{m^2 s^{-3}}$. It should be noted that there are discrepancies between the observations and his simulated buoyancy flux profile. A linear extrapolation of the observed buoyancy flux (see his Figure 3) yields $F_s = -0.001\,\mathrm{m^2 s^{-3}}$, which is somewhat closer to our estimate.

Denby (1999) also compared model results to idealized observations at Vatnajökull. Using $N = 0.013\,\mathrm{s^{-1}}, b_s = 0.36\,\mathrm{ms^{-2}}$, $z_j = 5.8\,\mathrm{m}$, and $\alpha = 4.5\,^{\mathrm{o}}$ (obtained from Denby's Figure 4 and Table 4), we obtain the estimate $F_s = -0.0022\,\mathrm{m^2 s^{-3}}$, which compares fairly well to Denby's estimate: $F_s = -0.0018\,\mathrm{m^2 s^{-3}}$.

The four examples of estimating F_s from idealized observations appear to yield better results than in the comparison to instantaneous measurements (previous section). However, some of these idealized observations are obtained from numerical simulations, which also rely on parameterizations, hence making it difficult to asses how well (4.11) actually works. A second remark concerning the results presented in this section, is that the surface buoyancy estimates are practically always larger than the observations. These discrepancies can be mitigated by choosing a larger value for c_1^{LES}, see e.g. Equation (4.11), but there is no clear justification for doing so.

Despite some discrepancies between our LES parameterization and the idealized observations presented here, it appears that (4.11) can be used to derive a first estimate of F_s. However, the parameterization should be further improved, e.g. by performing more simulations subject to more complex forcings than in this study.

[9]This result is obtained by using the air density 1.05 $\mathrm{kgm^{-3}}$, which was derived from a balloon soundings at 12Z, Oct 3, 2000. Source: http://weather.uwyo.edu.

4.7 Conclusions

We have used LES to study the influence of the slope angle, the surface buoyancy flux, and the stability of the ambient atmosphere on quasi one-dimensional, steady-state katabatic winds. The model results are interpreted using the classical Prandtl model. We find that the downslope velocity and wind maximum height increase with increasing surface buoyancy flux, but decrease with increasing stratification. For smaller inclinations the wind maximum increases due to a larger near-surface buoyancy. This buoyancy also depends on F_s, but is rather insensitive to changes in N. The simulations have further shown that the momentum fluxes are negative below the wind maximum, become zero at z_j, and continue to increase up to 3-4 times the height of the wind maximum, and thereafter they start diminishing again. The buoyancy flux profiles resemble the profiles observed in the SBL over plane surfaces. However, instead of decreasing linearly with height as in the horizontal SBL, in the katabatic layer F shows a larger decrease near the surface than further aloft, i.e. the buoyancy flux profile is curved with respect to height.
Turbulence is essential to the mixing process of momentum and buoyancy in the boundary layer. The TKE budgets of the resolved motions have shown that turbulence is mainly produced by wind shear, and destroyed by turbulence dissipation. The buoyancy is also a sink term, but plays only a secondary role. Near the wind maximum, the shear production goes to zero, and turbulence is produced by the transport term. The simulations have further showed that the TKE budget is affected the most by changes to the surface buoyancy flux. The turbulence mixing of momentum and buoyancy is frequently characterized by exchange coefficients. These exchange coefficients differ, i.e. momentum and buoyancy do not mix at the same rate. This difference is studied by considering the Prandtl number. We find that Pr increases with increasing stability, similar to previous studies. However, due to model limitations we cannot quantitatively determine the Prandtl number close to the surface and immediately above the wind maximum.
From the analytical Prandtl and GO models, we derive two linear relations (e.g. 4.11 and 4.14) for estimating the surface buoyancy flux from mean quantities. These relations, which can be regarded as parameterizations rules for F_s, are confirmed by the LES results. However, a comparison with field measurements show a considerable discrepancy between the parameterizations and the observations, the discrepancies most likely being caused by uncertainties in the observations. Nonetheless, one of the relations (4.11) yields promising results. The latter relation has also been compared to more idealized observations, and reasonable results are found, though the parameterization overestimates F_s. Further studying and improving this relation may help advancing parameterizations in meso-scale models.

5

Analytical solution for katabatic flow induced by an isolated cold strip

An analytical model for katabatic flow induced by cold strip of finite width in the cross-slope direction but of infinite extent in the downslope direction is presented. The fluid is assumed to have a constant (eddy) viscosity, and the Coriolis force is neglected. A numerical simulation has been used to verify the model, which is shown to revert to the classical Prandtl model if the strip width goes to infinity. The effects of the strip width and slope angle on the katabatic flow are studied. The buoyancy and downslope velocity reach maximum values at the centre of the strip, and spread outwards in the cross-slope direction. The downslope wind maximum weakens for narrow strips and shallow slopes. In contrast to the Prandtl solution, which shows a counter flow above the wind maximum, our model predicts the counter flow to occur outside the strip. The cross-slope variation in the surface forcing induces cross-slope and slope-normal velocities, which are manifested in vortices at the strip edges. Below the wind maximum, the fluid above the cooling surface descends and moves toward the strip edge where it is detrained from the strip region. Replenishment of fluid into the strip region takes place above the wind maximum.

Chaper is based on Axelsen *et al.* (2009).

5.1 Introduction

Downslope winds, also referred to as katabatic winds, are common in nature. When an inclined surface is cooled, a temperature difference is set up between the surface layer and the environmental air at the same altitude. The associate density difference gives rise to a negative buoyancy force, which induces a downslope flow.

Katabatic winds are subject to several forcings. In the previous chapter, we discussed the effects that the stratification of the atmosphere, the surface forcing, and the slope angle have on steady-state katabatic winds. While these forcings are homogeneous, downslope winds are also subject to inhomogeneous forcings of various types. For instance, inhomogeneous surface buoyancy fields arise due to partial cloud cover, differential solar heating, difference in surface cover (e.g. snow/soil/water) and variations in the vegetation types. Katabatic flows over glaciers, also called glacier winds, are in the ablation zone affected by a downslope variation in the surface buoyancy. While the temperature of the ice is constant at 0 °C, the corresponding potential temperature decreases down the slope, typically at a rate exceeding the rate of change of the environmental potential temperature.

In addition to inhomogeneous surface buoyancy fields, katabatic winds in mountainous terrain are affected by the ubiquitously changing orography. The downslope flow over a valley glacier may be influenced by a narrowing/widening of the valley and changes in the valley direction. The valley walls form (ice-free) impenetrable boundaries for the glacier wind. When they are heated, the temperature difference between the walls and the centre of the valley generates a cross-slope circulation (e.g. Whiteman, 2000).

The katabatic flow over a sufficiently long slope is close to one-dimensional, i.e. the flow depth, speed and buoyancy are invariant with downslope distance (e.g. Nappo and Rao, 1987; Papadopoulos *et al.*, 1997; Haiden and Whiteman, 2005). This invariance simplifies the governing equations, permitting the vertical structure to be analytically described. One of the first analytical models addressing this issue was presented by Prandtl (1942). This model, which was discussed in the previous chapter, describes the katabatic flow along a uniformly cooled sloping planar surface in a stably stratified fluid. The solution yields a vertical profile of buoyancy, which shows a layer of negative buoyancy near the surface, capped by a layer of positively buoyant air (further aloft the oscillation in the profile around zero buoyancy quickly dampens out). The associated profile of downslope velocity exhibits a low-level wind maximum, topped by a weak reverse flow. Observations of katabatic flow show that an appropriately tuned Prandtl model qualitatively reproduces the observed profiles of downslope velocity and buoyancy rather well (e.g. Papadopoulos *et al.*, 1997; Grisogono and Oerlemans, 2001a).

Other related models have made provision for the Coriolis force (e.g. Gutman and Malbakhov, 1964; Lykosov and Gutman, 1972; Gutman and Melgarejo,

1981; Egger, 1985; Stiperski *et al.*, 2007; Kavcic and Grisogono, 2007), some in combination with external winds, radiative damping and time dependence. All these models apply first-order closure to the turbulence flux terms, but treat the turbulence exchange coefficients differently, from constants to more complex height-dependent functions. As shown by Gutman and Malbakhov (1964), the buoyancy and cross-slope velocity fields tend to spread inexorably upward when the Coriolis force is included. Egger (1985) argued that these fields vanish away from the slope when either a geostrophic wind or a radiative damping is taken into account. However, in the case of an imposed geostrophic wind, unrealistically large values of those winds were required to prevent the continued upward growth of the buoyancy and cross-slope velocity fields. Kavcic and Grisogono (2007) more recently argued that the upward growth would diminish if the turbulence exchange coefficients are chosen appropriately, a result questioned in the review by Shapiro and Fedorovich (2008).

The effect of topography on slope flows was studied by Egger (1990), who looked at the linkage of the flow in a main valley and the circulation in side-valleys. Slope winds induced by differential surface buoyancy fields have been studied in e.g. Egger (1981), and Kondo (1984). In a recent paper, Shapiro and Fedorovich (2007) considered katabatic flows in which the surface buoyancy increased/decreased linearly with downslope distance. They presented an analysis of the along-slope and slope-normal velocities at the top of the katabatic layer, shedding light on how the entrainment rate at the top of the katabatic layer may depend on the downslope change of the surface buoyancy. More recently, Shapiro and Fedorovich (2008) (hereafter SF08) looked at the katabatic flow induced by an along-slope cold strip of limited width. The flow problem additionally included the Coriolis force. The qualitative behaviour of the cross-slope velocity and buoyancy fields far above the surface were investigated analytically. However, closer to the surface the buoyancy and velocity fields were inferred from numerical simulations. Numerical results showed two counter-rotating circulations on either side of the strip, centred on baroclinic zones of strong cross-slope surface buoyancy gradient. A broad region of descending fluid was found between the two circulation centres. Throughout the lower part of the domain a pronounced cross-slope flow was observed.

In contrast to one-dimensional studies, SF08 found that for katabatic winds induced by an isolated strip, the cross-slope velocity and the buoyancy did not diffuse upward indefinitely. They found also that the downslope and slope-normal velocities would not vanish far above the surface. Instead, the far-above-slope downslope and slope-normal velocities combined into a purely horizontal streaming motion along environmental isentropes. It was argued in SF08 that secondary processes not included in the equations may, if persistent, be vital in controlling the structure of the steady-state flow.

To our knowledge, no analytical solution has yet been obtained for the katabatic flow induced by a surface buoyancy forcing that is inhomogeneous in the cross-slope direction. In this paper we extend the Prandtl model to include

such an inhomogeneous surface forcing. The work builds on the considerations by SF08, except that we consider glaciers winds (characterized by short time scales and shallow boundary layer depths) for which the Coriolis force plays only a minor role.
The flow problem and solution are formulated in the next section. In Section 5.3 we verify the analytical model by comparing model results to results obtained from a numerical simulation. The effects of the strip width and slope angle on the spatial structure of the buoyancy and velocity fields are discussed in Section 5.4. We limit the consideration to slope angles typical of glaciers (e.g. 1 - 10 degrees). Finally, in Section 5.5 we present a summary and suggestions for future work.

5.2 Analytical model

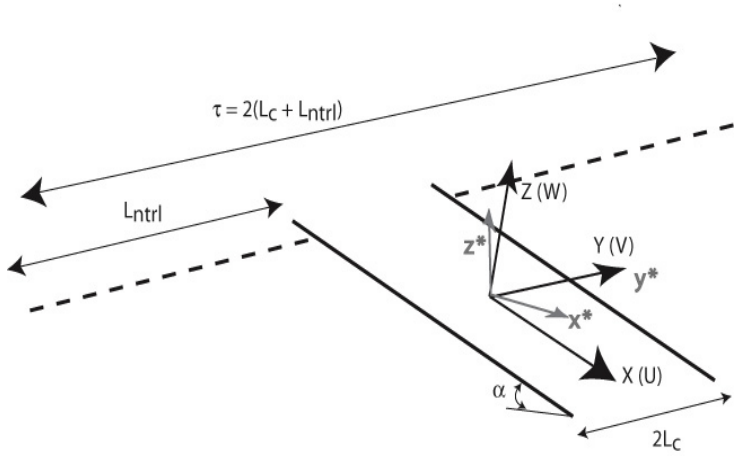

Figure 5.1. The slope-following Cartesian coordinate system is rotated by the slope angle α (> 0) from the horizontal, non-rotated Cartesian coordinate system denoted by asterisk. The downslope flow, induced by an isolated cold strip with width $2L_c$, is in the X-direction. The surface buoyancy field is inhomogeneous in the cross-slope (Y) direction: adjacent to the strip is a neutrally buoyant surface with width L_{ntrl} ($L_{ntrl} \rightarrow \infty$ for an isolated strip). All quantities are dimensionless, see text for further details.

The katabatic flow is described in a Cartesian coordinate system aligned with the slope, which is inclined at an angle α (> 0) to the horizontal. The x, y and z axes point respectively along the direction of the slope, the cross-slope direction, and the slope-normal direction, see Figure 5.1.
In the rotated coordinate system, the Boussinesq equation of thermodynamic

energy is

$$\frac{\partial b}{\partial t} + (\mathbf{v}\cdot\nabla)b = N^2\left(u\sin\alpha - w\cos\alpha\right) + \kappa\nabla^2 b. \tag{5.1}$$

Here b is the buoyancy, the Laplace operator is $\nabla^2 = \partial^2/\partial x^2 + \partial^2/\partial y^2 + \partial^2/\partial z^2$, κ is the thermal diffusivity coefficient, $N = (g\Gamma/\theta_r)^{1/2}$ is the Brunt-Väisälä frequency with g and θ_r being, respectively, the acceleration due to gravity and a reference potential temperature, and $\Gamma \equiv \mathrm{d}\Theta_a/\mathrm{d}z^*$ is the uniform lapse rate[1] of the ambient potential temperature, Θ_a, in the non-rotated coordinate system, denoted by an asterisk. The velocity vector $\mathbf{v}$ has the components u, v and w in the x, y and z directions, respectively. The momentum balance and continuity equations are

$$\frac{\partial u}{\partial t} + (\mathbf{v}\cdot\nabla)u = \frac{-1}{\rho_r}\frac{\partial p'}{\partial x} - b\sin\alpha + \nu\nabla^2 u, \tag{5.2}$$

$$\frac{\partial v}{\partial t} + (\mathbf{v}\cdot\nabla)v = \frac{-1}{\rho_r}\frac{\partial p'}{\partial y} + \nu\nabla^2 v, \tag{5.3}$$

$$\frac{\partial w}{\partial t} + (\mathbf{v}\cdot\nabla)w = \frac{-1}{\rho_r}\frac{\partial p'}{\partial z} + b\cos\alpha + \nu\nabla^2 w, \tag{5.4}$$

$$\nabla\cdot\mathbf{v} = 0, \tag{5.5}$$

where ν is the diffusion coefficient of momentum, and ρ_r is a constant reference density. The perturbation pressure $p' = p - p_a$ is the pressure p minus the hydrostatic pressure p_a, which is dependent only on z^*.
In the remainder we use the non-dimensionalized variables introduced in SF08, repeated here for convenience:

$$(X,Y,Z) \equiv \frac{(x,y,z)}{l_s}, \quad (U,V,W) \equiv \frac{(u,v,w)}{u_s}, \quad \Pi \equiv \frac{p'}{p_s}, \quad B = \frac{b}{b_s},$$

where the length, pressure, velocity and buoyancy scales are given by, respectively,

$$l_s \equiv \left(\frac{\nu}{N\sin\alpha}\right)^{1/2}, \quad p_s \equiv \rho_r l_s b_s \cos\alpha, \quad u_s \equiv \frac{b_s}{N}, \quad b_s \equiv |b_0| = |b(z=0)|.$$

Following SF08, we consider a stationary flow that is homogeneous in the downslope direction (all derivatives with respect to X drop out, e.g. the Lapla-

[1] For our definition of the lapse rate see footnote on page 51.

cian becomes $\nabla^2 = \partial^2/\partial Y^2 + \partial^2/\partial Z^2$). Linearizing (5.1) - (5.5) yields

$$\begin{aligned} 0 &= U - W\cot\alpha + Pr^{-1}\nabla^2 B, && (5.6)\\ 0 &= -B + \nabla^2 U, && (5.7)\\ 0 &= -\frac{\partial \Pi}{\partial Y}\cot\alpha + \nabla^2 V, && (5.8)\\ 0 &= -\frac{\partial \Pi}{\partial Z}\cot\alpha + B\cot\alpha + \nabla^2 W, && (5.9)\\ 0 &= \frac{\partial V}{\partial Y} + \frac{\partial W}{\partial Z}, && (5.10) \end{aligned}$$

where $Pr \equiv \nu/\kappa$ is the Prandtl number. This set of equations is similar to Equations. (5.1) - (5.5) is SF08. One difference is the absence of the Coriolis term, which links the downslope velocity to the cross-slope velocity, and vise versa. Secondly, we do not assume the length scales in the cross-slope direction to be much larger than the length scales in the vertical direction (i.e. $\partial^2/\partial Y^2 \ll \partial^2/\partial Z^2$).
In the above equations, the non-linear advective terms are neglected. Below we show that for laminar flow this approximation is justifiable. For turbulent flow, however, the approach is more questionable. This issue is addressed in Section 5.5.
Equation (5.10) permits the introduction of a stream function Ψ defined by $V = \partial\Psi/\partial Z$ and $W = -\partial\Psi/\partial Y$. The pressure is eliminated by taking the Z-derivative of (5.8) and subtracting the Y-derivative of (5.9), to obtain

$$\begin{aligned} 0 &= U + \frac{\partial \Psi}{\partial Y}\cot\alpha + \nabla^2 B, && (5.11)\\ 0 &= -B + \nabla^2 U, && (5.12)\\ 0 &= -\cot\alpha\frac{\partial B}{\partial Y} + \nabla^4 \Psi, && (5.13) \end{aligned}$$

where we assume $Pr = 1$. The system of equations (5.11) - (5.13) is further reduced to

$$\left[\nabla^6 + \nabla^2 + c\frac{\partial^2}{\partial Y^2}\right] B = 0, \qquad (5.14)$$

where $c \equiv \cot^2\alpha$.
We solve Equations (5.11) - (5.13) by using Fourier series and the fact that the buoyancy, downslope velocity and stream function are assumed to be periodic in a horizontal domain with width

$$\tau = 2L_c(1 + L_{ntrl}/L_c), \qquad (5.15)$$

see Figure 5.1. The position of the domain within the coordinate system is chosen in a way that $Y = 0$ is in the middle of the strip. The non-dimensional

half-width of the negatively buoyant surface, L_c, is obtained by scaling the dimensional half-width of the strip by l_s. Note, although L_c is the half-width of the strip, we shall in the remainder refer to this variables as the strip width. The non-dimensional width of the neutrally buoyant surface, L_{ntrl}, is defined in a similar way.

Since we use Fourier series to solve the flow problem analytically, we must apply periodic boundary conditions in the cross-slope direction. This periodicity implies that there is an infinite number of isolated strips. However, if the neutrally buoyant surface separating a given strip from its neighbours is very broad, then the neighbouring strips should only minimally influence the flow over the given strip.

For boundary conditions in the vertical direction, we require the buoyancy and velocity fields to vanish far above the surface, i.e. $B, U, \Psi \to 0$ as $Z \to \infty$. At the surface we impose the no-slip condition to the downslope and cross-slope velocities, the impermeability condition to the slope-normal velocity, and prescribe the buoyancy, which depends on the cross-slope location. The non-dimensional surface buoyancy in the strip region is $B(|Y/L_c| \leq 1, Z = 0) = -1$, and for the neutrally buoyant surface $B(|Y/L_c| > 1, Z = 0) = 0$.

It can be seen that this boundary value problem (differential equations and boundary conditions) has only two degrees of freedom: the slope angle α, and the non-dimensional length scale characterizing the width of the cold strip L_c. There is a third parameter, the ratio of the strip width to the width of the computational domain, but our intention is to consider strips that are isolated (as much as possible) so this ratio will eventually drop from the problem. In practice, it will be made as small as computational resources will allow. It should be noted that none of the non-dimensional governing parameters of the problem can be interpreted as a Reynolds number.

We solve (5.14) by expanding B as

$$B(Y,Z) = \sum_{n=1}^{\infty} \left[a_n(Z) \cos\left(\frac{2n\pi}{\tau} Y\right) + \tilde{a}_n(Z) \sin\left(\frac{2n\pi}{\tau} Y\right) \right] + a_0(Z). \quad (5.16)$$

We introduce the new variable $p \equiv n\pi/[L_c(1+\mathcal{R})]$, where the isolation parameter is defined as

$$\mathcal{R} \equiv L_{ntrl}/L_c. \quad (5.17)$$

It varies from 0 (Prandtl model, no surface with neutral buoyancy) to ∞ (an isolated strip). Due to the choice of coordinate system and surface boundary conditions, B is an even function in Y, which gives $\tilde{a}_n = 0\ \forall n$. Below we sketch how the general solution to (5.11) - (5.13) is obtained, with the detailed derivation being given in Appendix 5A.

Since (5.14) is a linear homogeneous differential equation with constant coefficients, we anticipate that it admits exponential solutions. Accordingly, in (5.16) we assume that $a_n(Z) \propto e^{mZ}$, yielding a sixth-order ordinary differential equation in Z. The proportionality constants associated with a_n are

determined by the boundary conditions. The general solution to (5.14) is (see also Equation 5A.3)

$$B(Y,Z) = \sum_{n=1}^{\infty} \cos(pY) \left[C_n e^{m_1 Z} + D_n e^{m_2 Z} + E_n e^{m_3 Z} \right] + a_0(Z), \qquad (5.18)$$

with C_n, D_n, and E_n being constants determined by the boundary conditions. By the requirement that the buoyancy vanishes far above the surface, only three exponents m are retained, see Equation (5A.2). The $n = 0$ contribution to the Fourier series is discussed separately in Appendix 5C.
Regarding B as known, the stream function Ψ can be determined from (5.13), which is a fourth-order, linear, non-homogeneous differential equation. The solution is the sum of a particular solution (see Equation 5A.5) and the solution to the homogeneous part (see Equation 5A.7):

$$\Psi(Y,Z) = \sum_{n=1}^{\infty} \sin(pY) \left[\beta_{1,n} C_n e^{m_1 Z} + \beta_{2,n} D_n e^{m_2 Z} + \beta_{3,n} E_n e^{m_3 Z} + \gamma_n e^{-pZ} \right]. \qquad (5.19)$$

Because the expansion is carried out over sines, the $n = 0$ contribution to the Fourier series for Ψ is zero. The constants $\beta_{\sigma,n}$ in Equation (5A.6), are associated with the particular solution and relate the stream function to the buoyancy. The constants γ_n are associated with the solution to the homogeneous differential equation and are determined by the boundary conditions.
Lastly, the downslope velocity U is found using (5.12). The general solution is obtained using the same procedure as for the stream function, i.e. finding a particular solution (see Equation 5A.9) and adding the solution to the homogeneous differential equation (see Equation 5A.11):

$$\begin{aligned} U(Y,Z) &= \sum_{n=1}^{\infty} \cos(pY) \left[\delta_{1,n} C_n e^{m_1 Z} + \delta_{2,n} D_n e^{m_2 Z} + \delta_{3,n} E_n e^{m_3 Z} + \epsilon_n e^{-pZ} \right] \\ &+ \quad n = 0 \text{ contribution.} \end{aligned} \qquad (5.20)$$

The constants $\delta_{\sigma,n}$ relate the downslope velocity to the buoyancy, see (5A.10), whereas ϵ_n are constants associated with the solution to the homogeneous differential equation and are determined by the surface boundary condition.
In total five constants are determined by the surface boundary conditions. The surface buoyancy B_s, which is -1 in the strip region and 0 outside, is expanded in a Fourier series with Fourier coefficients $\mathcal{B}_n$, see (5B.1). The no-slip condition is applied to U and V $(= \partial\Psi/\partial Z)$, while the impermeability condition is applied to W $(= -\partial\Psi/\partial Y)$. Lastly, we use the Fourier representation of U, Ψ and B in (5.11). The resulting equations, which are worked out in Appendix

5B, can be summarized in a matrix form as

$$\begin{pmatrix} 1 & 1 & 1 & 0 & 0 \\ \delta_1 & \delta_2 & \delta_3 & 1 & 0 \\ m_1\beta_1 & m_2\beta_2 & m_3\beta_3 & 0 & -p \\ \beta_1 & \beta_2 & \beta_3 & 0 & 1 \\ \upsilon_1 & \upsilon_2 & \upsilon_2 & 1 & p\sqrt{c} \end{pmatrix} \begin{pmatrix} C_n \\ D_n \\ E_n \\ \epsilon_n \\ \gamma_n \end{pmatrix} = \begin{pmatrix} \mathcal{B}_n \\ 0 \\ 0 \\ 0 \\ 0 \end{pmatrix}, \qquad (5.21)$$

where $\upsilon_\sigma = \delta_{\sigma,n} + p\beta_{\sigma,n}\sqrt{c} + m_\sigma^2 - p^2$ (no summation over σ).
For $n = 0$ the constants $\delta_{\sigma,n}$ and $\beta_{\sigma,n}$ become singular. In Appendix 5C we look at the $n = 0$ contribution to the Fourier series (5.18) and (5.20), and find that these first terms yield solutions to the buoyancy and downslope velocity fields that are proportional to the Prandtl solution. In Section 5.4, the strip-centre vertical profiles of buoyancy and downslope velocity are compared to the Prandtl solution, which in a non-dimensional form reads:

$$\begin{aligned} B_{Pr}(Z) &= -e^{-Z/\sqrt{2}} \cos\left(Z/\sqrt{2}\right), \quad \text{and} \\ U_{Pr}(Z) &= e^{-Z/\sqrt{2}} \sin\left(Z/\sqrt{2}\right). \end{aligned} \qquad (5.22)$$

In Appendix 5C we show that for the homogeneous slope ($\mathcal{R} = 0$), the new analytical solution reverts to the Prandtl solution.

5.3 Model verification

Although our analytical model reverts to the Prandtl model in the case $\mathcal{R} = 0$, it is desirable to verify the model for a non-zero $\mathcal{R}$. In this section we present a comparison of the analytical model with results from a numerical simulation of a laminar katabatic flow.
The numerical code is based on the works by Nieuwstadt (1990), Fedorovich *et al.* (2001), Shapiro and Fedorovich (2004), and Shapiro and Fedorovich (2006). The adaptation of the model to simulation of flow over an isolated strip is described in SF08. The numerical simulation input parameters are the following: $\alpha = 3\,^{\circ}$, $N = 1\,\mathrm{s}^{-1}$, the surface buoyancy of the strip is b_0 = -0.01 ms^{-2}, and the diffusion coefficients ν and κ are $10^{-4}\,\mathrm{m}^2\mathrm{s}^{-1}$. Note that the values of the input parameters are chosen to ensure that the flow is laminar (low Reynolds number). The scale factors introduced in the last section provide $l_s = 4.37\,\mathrm{cm}$, $u_s = 0.01\,\mathrm{ms}^{-1}$ and $b_s = 0.01\,\mathrm{ms}^{-2}$, yielding the Reynolds number $Re \approx 4$.
In both the numerical simulation and analytical model, periodic boundary conditions are applied in the cross-slope direction. In order to simulate the flow induced by an isolated strip, a very large number of grid points is needed to put the lateral computational boundaries at a sufficiently large distance away from the cold strip (i.e. to have very large zones of neutrally buoyant surface

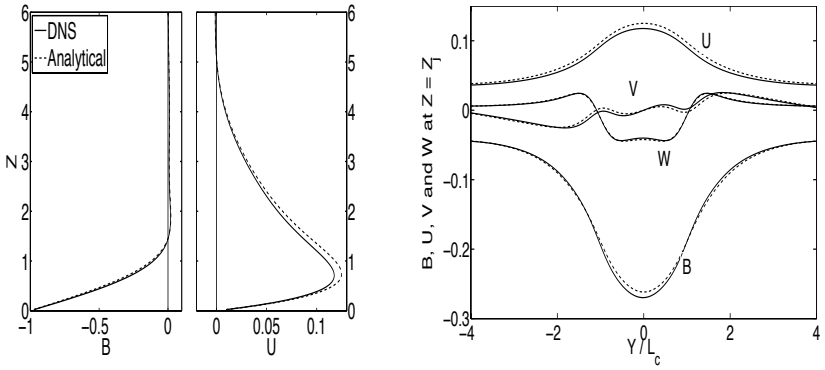

(a) (b)

Figure 5.2. Comparison of numerical simulation and analytical results of laminar flow ($Re \approx 4$) induced by a non-isolated strip: (a) buoyancy and downslope velocity at the centre of the strip, and (b) buoyancy and velocity components as functions of the cross-slope location. In (b) all variables are evaluated at the height of the wind maximum.

on either side of the cold strip). The computational costs are reduced by considering a non-isolated strip; in this case the isolation parameter is $\mathcal{R} = 3.41$. We adopted this value of $\mathcal{R}$ for the purpose of model verification.
The numerical simulation was carried out until a steady-state solution was reached. An excerpt of the numerical results is shown in Figure 5.2 together with the analytical results.
Figure 5.2(a) shows the buoyancy and the downslope velocity at the centre of the strip. Only small differences are noted between the numerical and analytical results. The most pronounced discrepancy is in the downslope velocity. For $Z \lesssim 4$ the analytical model overestimates U, but at most by $\sim 10\%$. The differences between the analytical and numerical results are likely due to a combined effect of the non-linear terms and numerical truncation errors.
In Figure 5.2(b) we show the numerical and analytical results for the buoyancy and the three velocity components as functions of cross-slope distance. All variables are evaluated at the height of the wind maximum Z_j. As noted above, the analytical model slightly overestimates the downslope velocity, foremost at $Y = 0$. In the strip region, small differences are noted between the buoyancy profiles. The numerical results show a larger negative buoyancy. The largest relative difference between the analytical and numerical results of buoyancy is 3%. Small differences are also seen in the profiles of cross-slope and slope-normal velocities. However, all variables point to a good overall agreement between the numerical and analytical data.
In the previous section, we discussed the application of periodic boundary con-

ditions in the cross-slope direction. This implies that we consider repeated negatively buoyant strips separated by neutrally buoyant surface patches. In the remainder we focus on the flow induced by an isolated strip. A cold strip can be considered virtually isolated if the buoyancy and velocity components of the katabatic flow approach zero at a sufficiently large distance from the strip, which can only happen if the width of the neutrally buoyant surface is very large. In our model this is achieved by using a large $\mathcal{R}$. The question how large the isolation parameter should be in order for the strip to be regarded as isolated, is answered by running the analytical model with different $\mathcal{R}$ and looking for convergence. Relative differences between solutions to the model using $\mathcal{R} = 250$ and 1000 were found to be negligible, hence $\mathcal{R} = 250$ may be considered sufficient.

5.4 Results

In this section we analyze the influence of the strip width L_c and slope angle α on the katabatic flow. With a constant slope angle $\alpha = 5\,^{\circ}$ we use the analytical model to evaluate three flow cases with the strip widths $L_c = 1, 5,$ and 10. With a fixed strip width, $L_c = 5$, three flow cases with slope angles $\alpha = 1, 5,$ and $10\,^{\circ}$ are studied. The input parameters are given in Table 5.1. Each case is assigned a label indicating the strip width and the slope angle, e.g. case L1A5 has a strip width 1 and a slope angle of $5\,^{\circ}$.
Below we present flow variables over $Y - Z$ planes. The model values are evaluated on a mesh with lateral and vertical grid spacing $\Delta Y = 0.015$ and $\Delta Z = 0.133$, respectively. The width of the domain is $-30 \leq Y/L_c \leq 30$ and the vertical extension is $0 \leq Z \leq 20$; for plotting purposes the figures only show a domain subsection. Furthermore, in the cross-slope direction the figures are scaled by the width of the strip in a manner that the surface cooling is always in the region $-1 \leq Y/L_c \leq 1$. Note that the lateral extent of the numerical mesh is not related to the isolation parameter.

5.4.1 Buoyancy and downslope velocity

The buoyancy in our model is a function of the cross-slope location as well as height. Figure 5.3 shows a cross-section of the buoyancy fields for various strip widths. At the surface, the scaled buoyancy is -1 in the strip region and 0 outside. For $Z \lesssim 2$ all cases show a pool of negative buoyancy (seen as an area enclosed by negative contour lines). The magnitude of this negative buoyancy drops sharply outside the strip region. Further aloft B becomes positive as in the original Prandtl solution. The cross-slope and slope-normal extents of the positive buoyancy decrease with increasing L_c. Both the maximum and minimum of the buoyancy are found at the centre of the strip.
Figure 5.4 shows the buoyancy fields for various slope angles. The effect of the

Table 5.1. Summary of modelled cases. Rows are sorted according to strip width (rows 1 - 3) and slope angle (rows 4 - 6). Note that case L5A5 appears twice. Results from the Prandtl solution are shown in the bottom row. The maximum buoyancy $\max(B)$ and downslope velocity $\max(U)$ are in the centre of the strip. The maximum counter flow is outside the strip, at height $Z_{\min(U)}$ and $Y = \pm Y_{\min(U)}$. In the dimensionless Prandtl solutions the extrema are independent of the slope angle, and there is no cross-slope variability in B or U.

	L_c	α deg	$\max(B)\ 10^{-2}$	$Z_{\max(B)}$	$\max(U)\ 10^{-2}$	$Z_{\max(U)}$	$\min(U)\ 10^{-2}$	$Z_{\min(U)}$	$Y_{\min(U)}$
L1A5	1	5	3.60	2.07	11.68	0.73	-0.25	5.40	23.91
L5A5	5	5	6.12	2.73	27.18	1.00	-1.22	5.40	4.95
L10A5	10	5	6.54	3.00	32.02	1.13	-2.30	5.40	2.70
L5A1	5	1	4.36	1.80	15.36	0.87	-0.45	5.26	15.21
L5A5	5	5	6.12	2.73	27.18	1.00	-1.22	5.40	4.95
L5A10	5	10	6.26	3.00	30.67	1.13	-1.39	5.40	3.54
Pr	∞	-	6.70	3.33	32.24	1.11	-1.39	5.55	-

slope angle on the buoyancy field is similar to that of the strip width. With increasing α the cross-slope extents of the pools of both positive and negative B decrease. Figures 5.4(a-c) indicate that for increasing α the negative buoyancy field becomes increasingly homogeneous in the strip region.

Figures 5.5(a,b) display the vertical profiles of the mid-strip ($Y = 0$) buoyancy as a function of the strip width and slope angle, respectively. In all cases the buoyancy is -1 at the surface and increases to a (positive) maximum at $Z \sim 2 - 3.5$. The height and magnitude of the buoyancy maximum increase with increasing L_c and α. For larger strip widths and slope angles, the height and magnitude of the buoyancy maximum approach values predicted by the Prandtl model.

Next we look at the downslope velocity U. Figure 5.6 presents contour plots of the downslope velocity as function of strip width. A jet-like wind maximum is observed over the strip, and the downslope velocity spreads in the cross-slope direction. As α increases, the cross-slope spread of U decreases but the vertical spread of U increases.

There is a profound difference between the along-slope velocity field, U, predicted by our model and the Prandtl solution. In the latter, the downslope wind maximum is capped by a layer of weak up-slope flow. In our solution, however, the downslope velocity over the centre of the strip slowly approaches zero for large Z without passing through negative values (no counter flow over

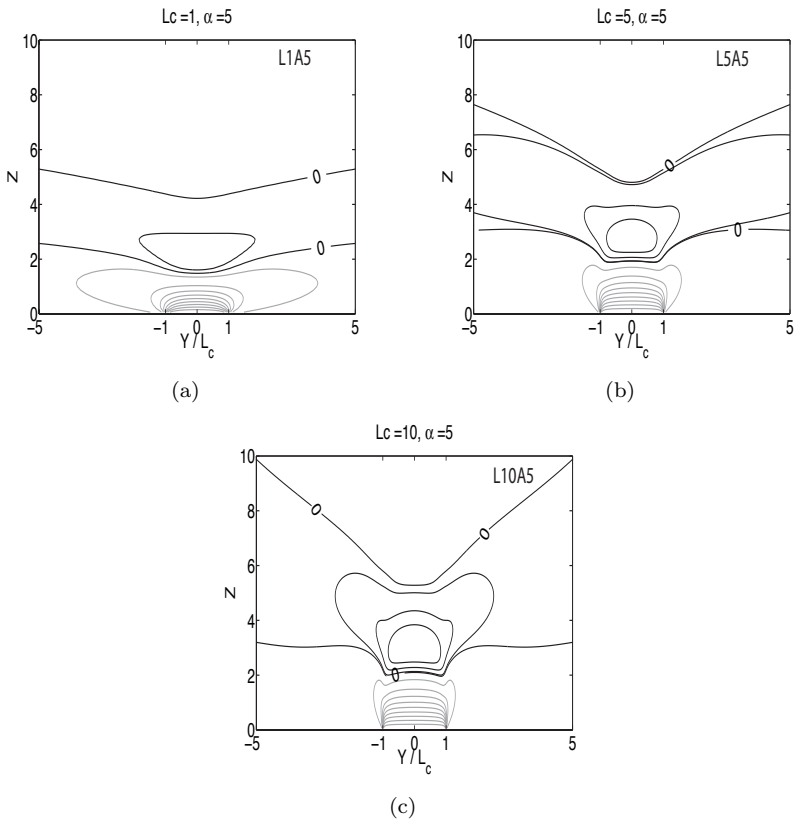

Figure 5.3. Contour plots of the buoyancy as a function of the strip width, illustrated by cases L1A5 (a) L5A5 (b) and L10A5 (c). Positive contour (black) intervals are 0.02 and negative contour (grey) intervals are 0.1. Zero contours are indicated with "0". Note that the horizontal axis is scaled to ensure that the buoyancy forcing is always between -1 and 1. The X-axis is directed out of the plot.

the centre of the strip). Instead, the counter flow occurs outside the strip. The up-slope flow is symmetric in $Y = 0$ as it takes place over the neutrally buoyant surfaces adjacent to the strip. A similar horizontal displacement of the return flow with respect to the strip was found in SF08, except the return flow there was not symmetric in $Y = 0$ due to the Coriolis force.
For $L_c = 1$, the counter flow is found at $|Y| > 20$, which is outside the figure domain. Figures 5.6(b,c) and Table 5.1 show that with increasing L_c the maximum counter flow intensifies and shifts closer to the strip. The height of the maximum counter flow $Z_{\min(U)}$ is fairly constant. Numerical results, evaluated on a grid with vertical grid distance $\Delta Z = 0.133$, show that in all cases the

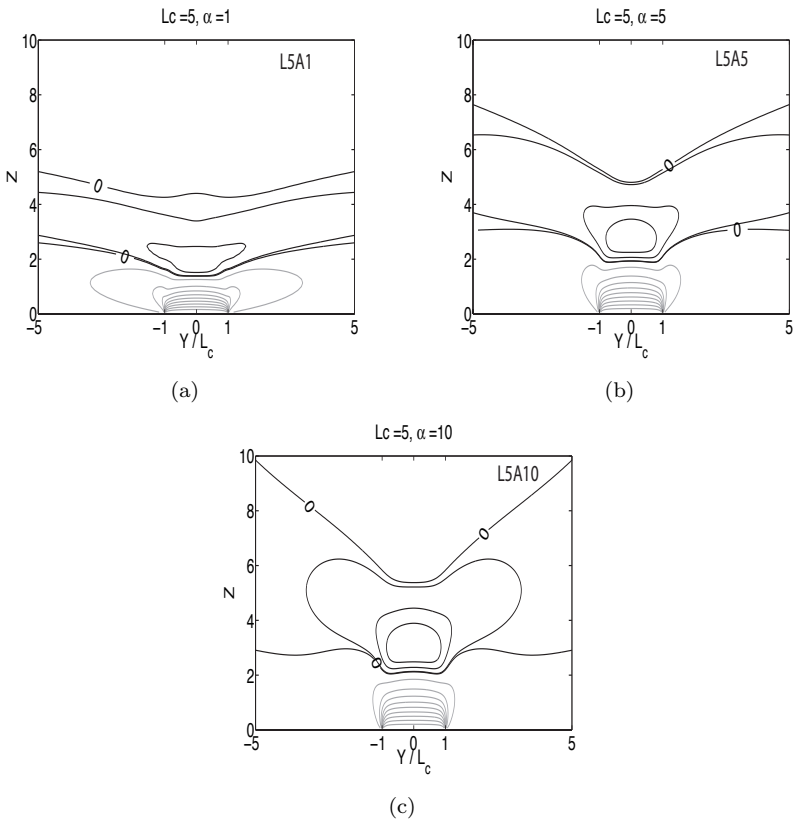

Figure 5.4. As in Figure 5.3 but for the buoyancy as a function of the slope angle: (a) case L5A1, (b) L5A5 and (c) L5A10.

height of the maximum counter flow is at $Z = 5.40$. However, results from a case with a larger strip width ($L_c = 15$) show a maximum counter flow at $Z = 5.53$, indicating that $Z_{\min(U)}$ varies only slowly L_c.

The contour plots of downslope velocity as function of the slope angle in Figure 5.7 show several similarities with the downslope velocity fields as functions of the strip width in Figure 5.6. For small slope angles the downslope flow extends in the cross-slope direction well beyond the strip. This extent decreases with increasing α. Outside the strip region, the peak counter flow increases in magnitude and draws closer to the strip with increasing α. The height of the maximum up-slope flow varies only slowly with α, ranging from 5.26 to 5.40 (difference of one grid level).

The wind maximum is located at the centre of the strip ($Y = 0$) for all L_c and α. The vertical profiles of U as a function of L_c and α are shown in

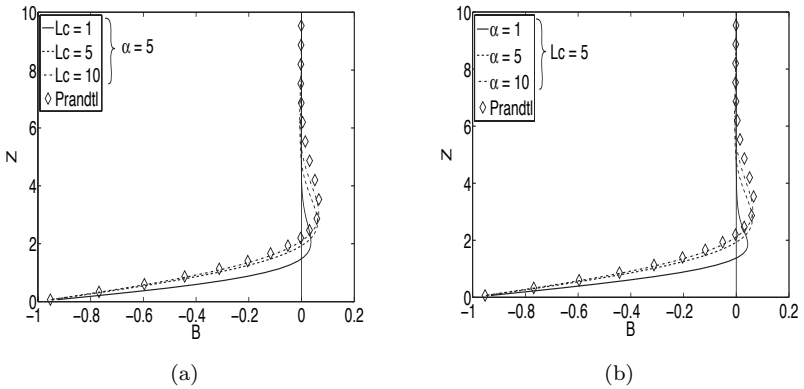

(a) (b)

Figure 5.5. Vertical profiles of the buoyancy at the strip centre as functions of the (a) strip width and (b) slope angle. The Prandtl profile of buoyancy (infinitely wide strip, independent of the slope angle) included for comparison, see text for details.

Figures 5.8(a,b), respectively. For the smallest strip width and slope angle, the wind maximum is less than half the wind maximum predicted by the Prandtl model. The magnitude of the wind maximum increases with increasing L_c and α, and a small increase in the wind maximum height Z_j is observed. It is interesting to point out that in the dimensionless Prandtl solutions, the height and magnitude of the wind maximum are independent of the slope angle.
A notable characteristic of the Prandtl solutions is the velocity oscillation about zero as Z increases. With a limited strip width the oscillation is the most pronounced for the wide strip and steep slope. However, the oscillation occurs around a positive value of U. All velocity profiles at the centre of the strip tend to zero for large Z without passing through negative values.

5.4.2 Cross-slope and slope-normal flow

The inhomogeneous surface forcing in our model produces vertical and cross-slope motions. Figure 5.9 shows contour plots of the stream function Ψ as a function of L_c. Close to the surface, vortices near the strip edges are observed. The motion is clockwise along negative contours. Below the wind maximum, the fluid above the cold surface descends and moves towards the strip edge where it is detrained from the strip region. Outside the strip, the motion is at first away from the strip and ascending, and thereafter a rising motion towards the strip is observed. The fluid re-enters the strip region above the wind maximum, and the circulation is closed by a branch of sinking motion.
Near the surface, $Z \lesssim 2.5$, an increase in L_c yields an increase in the contour line density, which corresponds to an increase in magnitudes of V and W.

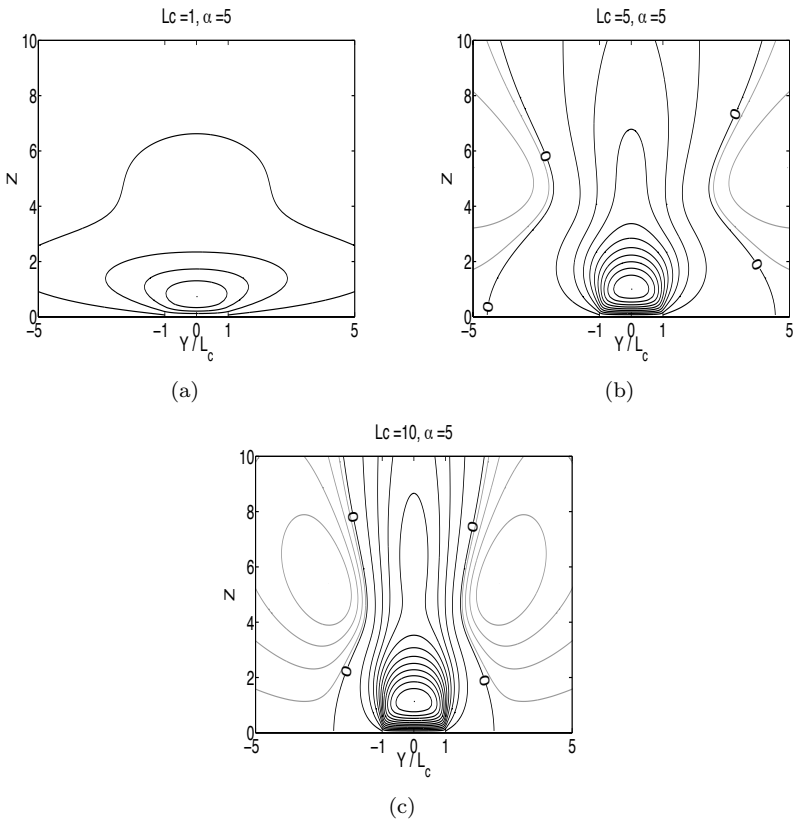

Figure 5.6. As in Figure 5.3 but for the downslope velocity U as a function of the strip width. Positive contour interval is 0.025, negative contour interval is 0.005. Note that the positive flow is directed out of the paper.

Figure 5.9 and Table 5.2 show that the height of the maximum Ψ is close to the height of the downslope wind maximum Z_j. The cross-slope circulation in the interior of the strip region ($|Y/L_c| \lessapprox 0.5$, $Z \lessapprox 2.5$) becomes centered around the strip edges for an increasing strip width. For large L_c, our model solution near the strip centre resembles the Prandtl solution.
Further away from the surface, $Z \gtrsim 2.5$, another set of vortices is observed. The circulation is opposite to the one in the lowermost vortices. We note that the cross-slope extent of the elevated pair of vortices decreases with increasing L_c. Instead, the vertical extent of the contour lines increases. For cases L1A5 and L5A5 the maximum Ψ is found near the wind maximum height, but for larger L_c, e.g. in the L10A5 case, $\max(\Psi)$ is associated with the uppermost pair of vortices ($Z \sim 5.75$).

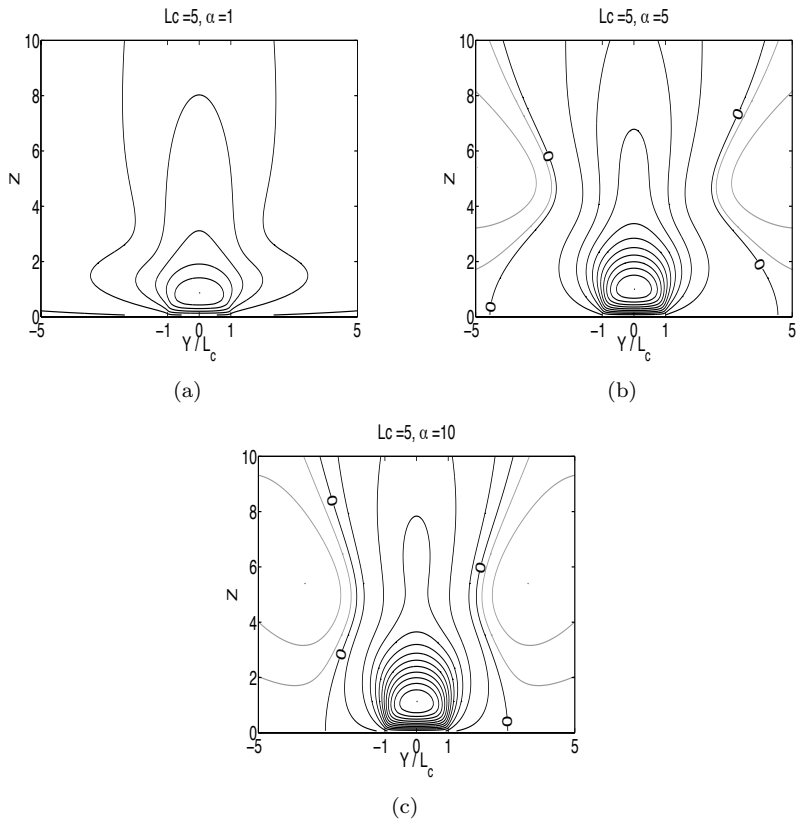

Figure 5.7. As in Figure 5.6 but for the downslope velocity U as a function of the slope angle.

Figure 5.10 shows Ψ as a function of the slope angle. An inspection of Figures 5.9 and 5.10 allows to conclude that an increasing slope angle affects Ψ similarly to an increase in L_c. In Figure 5.10, the maximum Ψ at $Z \gtrsim 2.5$ increases with increasing α, and the cross-slope extent of the contour lines decreases whereas the vertical extent increases. A notable difference with Figure 5.9 is that the maximum Ψ close to the surface ($Z \lesssim 2.5$) at some point starts decreasing. Near the surface the maximum values of Ψ for $\alpha = 5$ and $10^{\,o}$ are $8.4 \cdot 10^{-2}$ and $7.0 \cdot 10^{-2}$, respectively. The maximum V values for cases L5A5 and L5A10 are, respectively, $3.6 \cdot 10^{-2}$ and $3.2 \cdot 10^{-2}$. As may be concluded from the gradients of Ψ, the cross-slope velocity and slope-normal velocity both decrease in magnitude as α increases. Apparently, for slope angles larger than some critical value, $\alpha > \alpha_c$, the cross-slope circulation decreases. Since the cross-slope circulation is also determined by the strip width, we ex-

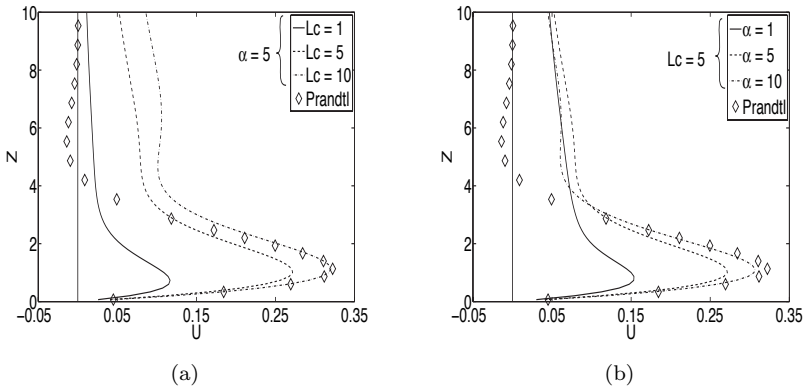

(a) (b)

Figure 5.8. As Figure 5.5 but for the downslope velocity U.

pect α_c to be a function of L_c as well. This is an issue that should be studied further.

5.5 Conclusions

In this chapter we focus on small-scale shallow katabatic flow for which the Coriolis effect is assumed to be negligible. The flow is induced by a negatively buoyant strip with limited width. We present a dimensionless analytical solution in which the slope angle and the (dimensionless) width of the negatively buoyant strip are governing parameters.

The developed analytical model can be viewed as an extension to the Prandtl model. We have verified that the model reverts to the classical Prandtl model for an infinitely wide strip. The model is validated by comparing the results to the results from numerical simulations of a katabatic flow with a low Reynolds number ($Re \approx 4$).

The effects of the strip width L_c and the slope angle α are investigated. The negative buoyancy diffuses from the strip primarily outward. The outward diffusion decreases for broader strips and larger slope angles. At the centre of the strip, the maximum (positive) buoyancy increases for broad strips and large slope angles. A limit for the maximum buoyancy is given by the Prandtl model. It is interesting to note that observations of glacier winds hardly show any positive buoyancy values, e.g. Chapter 3. Compared to the Prandtl model, the reduced positive buoyancy predicted by our model is thus in better qualitative agreement with observations. This suggests that secondary lateral circulations, which are likely to occur in a katabatic flow of finite width, may be important for the katabatic flow dynamics.

Table 5.2. Summary of maxima in the stream function Ψ in terms of absolute values of Ψ. Note that Ψ is an odd function of Y, so that the minimum values in Ψ are equal in magnitude to the maximum values. The first three columns include data on the pair of vortices close to the surface ($Z \lesssim 2.5$) whereas the three last columns refer to the elevated pair of vortices ($Z \gtrsim 2.5$).

	$\max(\Psi)$ 10^{-2}	$Y_{\max(\Psi)}$	$Z_{\max(\Psi)}$	$\max(\Psi)$ 10^{-2}	$Y_{\max(\Psi)}$	$Z_{\max(\Psi)}$
L1A5	4.68	1.20	0.87	0.01	11.28	5.26
L5A5	8.37	0.99	1.13	5.39	2.55	5.40
L10A5	8.44	0.99	1.13	10.07	1.59	5.67
L5A1	7.22	1.02	0.73	1.59	6.60	4.73
L5A5	8.37	0.99	1.13	5.39	2.55	5.40
L5A10	7.03	0.99	1.27	7.42	1.98	5.80
	$Z \leq 2.5$			$Z > 2.5$		

The downslope velocity, which is caused by the negative buoyancy, attains a maximum at the centre of the strip. The magnitude of the maximum decreases toward the edges of the strip. As in the Prandtl model, we observe a counter flow. A particular result from our model, though, is that the counter flow is located outside the strip region. For larger L_c and α, the positive downslope velocity field becomes more confined to the strip region, while the counter flow intensifies and moves toward the strip. With increasing L_c and α, the magnitude of the wind maximum approaches the wind maximum predicted by the Prandtl model.

In the Prandtl model, the downslope wind decreases rapidly above the wind maximum and then oscillates around $U = 0$, as shown in Figure 5.8. In the case of an isolated strip, however, the downslope velocity at the centre of the strip remains positive and reduces to zero monotonically. The relatively slow decrease in U above the wind maximum is supported by observations of katabatic flow over valley glacier For example, the glacier wind observed over the Pasterze glacier, Austria, had a positive downslope velocity up to 50-200 m, see Chapter 3. The same observations, reanalyzed in Van den Broeke (1997b), showed that the height at which the downslope velocity became negative, had a diurnal cycle. It was also found that the daytime heating of the (ice-free) valley walls induced a downslope flow (i.e. down the valley walls) that merged with the glacier wind. These findings again illustrate the importance of including a cross-slope variation in the surface buoyancy when modelling the katabatic flow over a valley glacier.

In our analytical model, the finiteness of the negatively buoyant strip is responsible for inducing a cross-slope circulation. As in SF08, we find that close to the surface, a vortex develops on each strip edge. Immediately above the

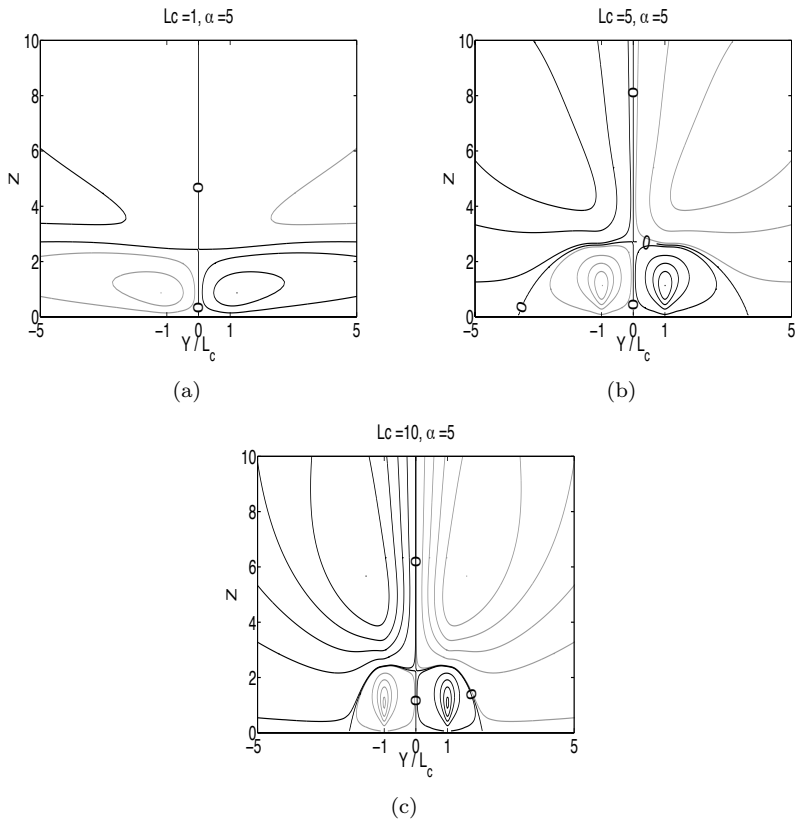

Figure 5.9. As Figure 5.3 but for the stream function Ψ as a function of L_c. The motion is clockwise along negative contours. Positive and negative contour intervals are 0.02.

surface, fluid descends and is detrained from the strip region. Outside the strip, the fluid first attains an outward ascending motion, and thereafter the direction shifts towards the strip. Upon re-entering the strip region the fluid starts descending again.

Further aloft, a second pair of counter-rotating vortices produce an ascending and outward motion above the strip. The intensity of the two pairs of vortices increases with increasing L_c and α. By increasing the slope angle from 5 to 10° we found that the circulation in the lowermost pair of vortices decreases. This suggests that the intensity of the cross-slope and slope-normal flow has a maximum at some given slope angle.

An apparent deficiency of the analytical model is the neglect of the non-linear terms in the governing equations. For low Reynolds number flow, this approach

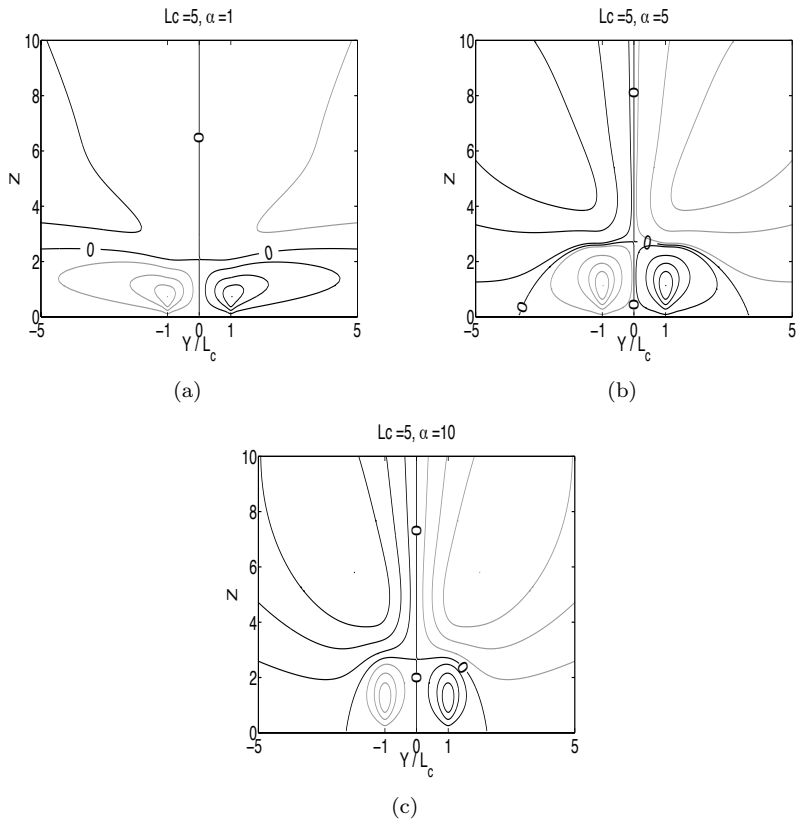

Figure 5.10. As Figure 5.9 but as a function of the slope angle.

does work as was shown by comparison of analytical predictions with numerical simulation results. However, for large Reynolds numbers (turbulent flow) we cannot *a priori* assume a negligible cross-slope advection of e.g. cross-slope velocity. Preliminary results from a large-eddy simulation (LES), described in Chapter 3, of turbulent katabatic flow over a non-islated strip ($\mathcal{R} = 4$) has shown that below the wind maximum the turbulent diffusion terms in the momentum balance are larger than the advection terms. However, further aloft, turbulent diffusion plays only a minor role. The large-eddy simulation results do show a near-surface vortex at each strip edge, but unlike the analytical model no elevated vortices are found. Future tests should be conducted to see if the elevated vortices appear in LES for flow cases where the strip is more isolated.

In the proposed analytical model, the surface buoyancy was assumed to be symmetric around the strip centre. A cross-slope variation of the surface buoy-

ancy different from the one discussed in this paper may be considered, provided the requirement of symmetry is fulfilled. However, a symmetric surface forcing is a highly idealized situation. For instance, diurnal solar heating of the air above a valley glacier is usually asymmetric. A possible extension of our model would be able to account for such an asymmetric surface forcing.

5A General solution

Applying the Fourier representation (5.16) in (5.14) yields:

$$\begin{aligned} 0 &= \sum_{n=1}^{\infty} \cos(pY) \left[\frac{\mathrm{d}^6 a_n}{\mathrm{d}Z^6} - 3p^2 \frac{\mathrm{d}^4 a_n}{\mathrm{d}Z^4} + \left(3p^4+1\right) \frac{\mathrm{d}^2 a_n}{\mathrm{d}Z^2} - p^6 a_n - p^2 (c+1)\, a_n \right]. \\ &+ a_0(Z) \end{aligned} \tag{5A.1}$$

Below it will be apparent that the $n = 0$ contribution to the Fourier series will yield a singularity. Therefore we first present a solution for $n > 0$. The $n = 0$ contribution is analyzed separately in Appendix 5C.
Assume that a_n behaves exponentially: $a_n(Z) \propto e^{mZ}$, with proportionality coefficients being determined by the boundary conditions. Since the $\cos(pY)$ factors (as functions of n) are linearly independent, the terms enclosed by square brackets should sum to zero for every n, hence

$$0 = \xi^3 - 3t\xi^2 + \left(3t^2+1\right)\xi - t^3 - tc - t,$$

where $\xi \equiv m^2$ and $t \equiv p^2$.
The general solution to the cubic equation $\chi^3 + h_2\chi^2 + h_1\chi + h_0 = 0$ (h_i are constants) is (e.g. Abramowitz and Stegun, 1964)

$$\begin{aligned} \chi_1 &= \frac{-1}{3}h_2 + (S+T), \\ \chi_2, \quad \chi_3 &= \frac{-1}{3}h_2 - \frac{1}{2}(S+T) \pm \frac{i\sqrt{3}}{2}(S-T), \\ S &= \left[R+\sqrt{D}\right]^{1/3}, \quad T = \left[R-\sqrt{D}\right]^{1/3} \quad \text{with} \quad D = Q^3 + R^2, \\ Q &= \frac{3h_1 - h_2^2}{9} \quad \text{and} \quad R = \frac{9h_2h_1 - 27h_0 - 2h_2^3}{54}. \end{aligned}$$

The roots of ξ become

$$\xi_1 = t + \rho, \quad \xi_2 = t - \frac{1}{2}\rho + \frac{i\sqrt{3}}{2}\eta, \quad \text{and} \quad \xi_3 = t - \frac{1}{2}\rho - \frac{i\sqrt{3}}{2}\eta,$$

where $\rho \equiv \mathcal{S}^{1/3} - \mathcal{T}^{1/3}$, $\eta \equiv \mathcal{S}^{1/3} + \mathcal{T}^{1/3}$ and

$$\mathcal{S} \equiv \frac{tc}{2} + \sqrt{\frac{1}{27} + \frac{t^2c^2}{4}} \quad \text{and} \quad \mathcal{T} \equiv \left| \frac{tc}{2} - \sqrt{\frac{1}{27} + \frac{t^2c^2}{4}} \right|.$$

The polar form of the complex root ξ_2 can be written as

$$\xi_2 = \sqrt{\left(t - \rho/2 + i\sqrt{3}\eta/2\right)\left(t - \rho/2 - i\sqrt{3}\eta/2\right)}e^{i\theta} = \zeta e^{i\theta},$$

and similarly $\xi_3 = \zeta e^{-i\theta}$, where $\theta = \text{atan}\left[(\sqrt{3}\eta/2)/(t - \rho/2)\right]$.
More precisely,

$$\begin{aligned} \zeta\cos\theta &= t - \rho/2 \Rightarrow \cos\theta = \frac{t - \rho/2}{\zeta}, \\ \zeta\sin\theta &= \sqrt{3}\eta/2 \Rightarrow \sin\theta = \frac{\sqrt{3}}{2}\frac{\eta}{\zeta}. \end{aligned}$$

Since both η and ζ are positive, $\sin\theta$ is positive, which implies that θ is in the first or second quadrant, depending on the sign of $t - \rho/2$. Therefore, when obtaining the roots $m = \pm\sqrt{\xi_2}$, the angle $\theta/2$ is guaranteed to be in the first quadrant. We seek for a_n an exponential function e^{mZ} that is bounded for all Z, and thus the roots with positive real parts must be rejected.
The three physical roots are

$$m_1 = -\sqrt{t + \rho} \quad , \quad m_2 = -\sqrt{\zeta}e^{i\theta/2} \quad \text{and} \quad m_3 = -\sqrt{\zeta}e^{-i\theta/2}. \qquad (5A.2)$$

The expression for a_n is a superposition of the three exponential functions:

$$a_n(Z) = C_n e^{m_1 Z} + D_n e^{m_2 Z} + E_n e^{m_3 Z},$$

and the full solution to (5A.1) becomes

$$B(Y, Z) = \sum_{n=1}^{\infty} \cos(pY)\left[C_n e^{m_1 Z} + D_n e^{m_2 Z} + E_n e^{m_3 Z}\right], \qquad (5A.3)$$

with C_n, D_n, and E_n being constants determined by the boundary conditions. The stream function Ψ is constrained by (5.13) to satisfy

$$\nabla^4\Psi = \cot\alpha \sum_{n=1}^{\infty} -p\sin(pY)\left[C_n e^{m_1 Z} + D_n e^{m_2 Z} + E_n e^{m_3 Z}\right], \qquad (5A.4)$$

which is a linear, non-homogeneous differential equation. The solution is the sum of the solution to the homogeneous differential equation plus a particular solution, $\Psi = \Psi_h + \Psi_p$. Seeking a particular solution on the form

$$\Psi_p = \sum_{n=1}^{\infty} \sin(pY)\left[\beta_{1,n} C_n e^{m_1 Z} + \beta_{2,n} D_n e^{m_2 Z} + \beta_{3,n} E_n e^{m_3 Z}\right],$$

where $\beta_{\sigma,n}$ are constants, we get

$$\begin{aligned}\nabla^4\Psi_p &= \sum_{n=1}^{\infty}\sin(pY)\Big\{\beta_{1,n}C_n\left(m_1^4-2p^2m_1^2+p^4\right)e^{m_1Z} \\ &+ \beta_{2,n}D_n\left(m_2^4-2p^2m_2^2+p^4\right)e^{m_2Z}+\beta_{3,n}E_n\left(m_3^4-2p^2m_3^2+p^4\right)e^{m_3Z}\Big\}.\end{aligned} \tag{5A.5}$$

Applying (5A.5) in (5A.4) yields

$$\begin{aligned}\beta_{1,n} &= -p\cot\alpha/\left(m_1^4-2p^2m_1^2+p^4\right), \\ \beta_{2,n} &= -p\cot\alpha/\left(m_2^4-2p^2m_2^2+p^4\right), \\ \beta_{3,n} &= -p\cot\alpha/\left(m_3^4-2p^2m_3^2+p^4\right).\end{aligned} \tag{5A.6}$$

In solving the homogeneous part of the differential equation, we assume $\Psi_h = \sum_{n=1}^{\infty}\tilde{\psi}_n\sin(pY)$ and $\tilde{\psi}_n = \gamma_n e^{gZ}$, γ_n being constants, yielding

$$\nabla^4\Psi_h = \sum_{n=1}^{\infty}\left(g^4-2g^2p^2+p^4\right)\gamma_n e^{gz}\sin(pY) = 0.$$

Since $\sin(pY)$ are linearly independent (for different n), we must have $g^4-2g^2p^2+p^4=0$, or $g=\pm p$. A fourth-order differential equation has four solutions. In this case $\tilde{\psi}$ must be of the form $\gamma_n e^{\pm pZ}$ or $\gamma_n Z e^{\pm pZ}$ (e.g. Kreyszig, 1999). Since the solutions must be bounded as Z goes to infinity, the terms associated with a positive exponent are omitted. Moreover, it can be shown that the expressions for U and B do not contain terms on the form Ze^{-pZ}, i.e. they must also be rejected from the solution to the homogeneous differential equation. We thus find that

$$\Psi_h = \sum_{n=1}^{\infty}\gamma_n e^{-pZ}\sin(pY). \tag{5A.7}$$

The full solution to Ψ becomes

$$\Psi = \sum_{n=1}^{\infty}\sin(pY)\left[\beta_{1,n}C_n e^{m_1Z}+\beta_{2,n}D_n e^{m_2Z}+\beta_{3,n}E_n e^{m_3Z}+\gamma_n e^{-pZ}\right]. \tag{5A.8}$$

From (5.12) we have $\nabla^2 U = B$, which is a second-order non-homogeneous differential equation. Following the approach above, we will solve for $U = U_h + U_p$ where we seek the particular solution U_p in the form

$$U_p = \sum_{n=1}^{\infty}\cos(pY)\left[\delta_{1,n}C_n e^{m_1Z}+\delta_{2,n}D_n e^{m_2Z}+\delta_{3,n}E_n e^{m_3Z}\right], \tag{5A.9}$$

with $\delta_{\sigma,n}$ being constants. The Laplacian of the particular solution is:

$$\begin{aligned}\nabla^2 U_p &= \sum_{n=1}^{\infty} \cos(pY)\Big[\left(m_1^2 - p^2\right)\delta_{1,n} C_n e^{m_1 Z} \\ &+ \left(m_2^2 - p^2\right)\delta_{2,n} D_n e^{m_1 Z} + \left(m_3^2 - p^2\right)\delta_{3,n} E_n e^{m_1 Z}\Big],\end{aligned}$$

which must equal the right hand side of (5A.3). Equating exponents of the same power yields:

$$\delta_{1,n} = 1/\left(m_1^2 - p^2\right), \quad \delta_{2,n} = 1/\left(m_2^2 - p^2\right), \quad \delta_{3,n} = 1/\left(m_3^2 - p^2\right). \tag{5A.10}$$

For the homogeneous part U_h, assume a solution on the form $U_h = \sum_{n=1}^{\infty} \tilde{u}\cos(pY)$ with $\tilde{u} = \epsilon_n e^{gZ}$, where ϵ_n are constants. The Laplacian of U_h gives

$$\nabla^2 U_h = \sum_{n=1}^{\infty} \cos(pY)\left(g^2 - p^2\right)\epsilon_n e^{gZ}. \tag{5A.11}$$

Since the right hand side of (5A.11) must vanish, $g = \pm p$. Omitting the non-physical root $g = +p$, the sum of the homogeneous and particular solutions becomes

$$U = \sum_{n=1}^{\infty} \cos(pY)\left[\delta_{1,n} C_n e^{m_1 Z} + \delta_{2,n} D_n e^{m_2 Z} + \delta_{3,n} E_n e^{m_3 Z} + \epsilon_n e^{-pZ}\right]. \tag{5A.12}$$

This concludes the general solution to the three variables B, Ψ and U given by (5A.3), (5A.8) and (5A.12), respectively, with constants given by (5A.6) and (5A.10).

5B Surface boundary conditions

In deriving the general expressions for B, U and Ψ we applied the periodic boundary condition in the cross-slope direction, and required that flow variables vanish as $Z \to \infty$. Here we focus on the surface boundary conditions ($Z = 0$). The surface buoyancy is -1 in the strip region and 0 outside, i.e.

$$B_s(Y) \equiv B(Y, 0) = -1 \quad \text{if} \quad |Y| \le L_c, \quad 0 \quad \text{otherwise.}$$

The Fourier representation is

$$B_s = \sum_{n=1}^{\infty} \mathcal{B}_n \cos(pY) + \mathcal{B}_0. \tag{5B.1}$$

The coefficients $\mathcal{B}_n$ are given by

$$\begin{aligned} \mathcal{B}_0 &= \frac{1}{\tau}\int_{-\tau/2}^{\tau/2} B_s dY = \frac{-1}{1+\mathcal{R}}, \\ \text{and} & \qquad\qquad (5B.2) \\ \mathcal{B}_n &= \frac{2}{\tau}\int_{-\tau/2}^{\tau/2} B_s \cos(pY) dY = \frac{-2}{n\pi}\sin\left(\frac{n\pi}{1+\mathcal{R}}\right). \end{aligned}$$

Combining Equations (5A.3) and (5B.1) evaluated at the surface gives

$$\mathcal{B}_n = C_n + D_n + E_n.$$

At the surface we further impose the no-slip condition for the three velocity components. For $n > 0$, evaluating Equations (5A.8) and (5A.12) yields for U, $V = \partial\Psi/\partial Z$, and $W = -\partial\Psi/\partial Y$, at $Z = 0$ yields, respectively

$$\begin{aligned} 0 &= \delta_{1,n}C_n + \delta_{2,n}D_n + \delta_{3,n}E_n + \epsilon_n, \\ 0 &= m_1\beta_{1,n}C_n + m_2\beta_{2,n}D_n + m_3\beta_{3,n}E_n - p\gamma_n, \\ 0 &= -\beta_{1,n}C_n - \beta_{2,n}D_n - \beta_{3,n}E_n - \gamma_n. \end{aligned}$$

Lastly, using the Fourier representation of U, Ψ and B in (5.11) at $Z = 0$, we obtain

$$\begin{aligned} 0 &= \sum_{n=1}^{\infty}\cos(pY)\Big\{C_n(\delta_{1,n} + p\beta_{1,n}\sqrt{c} + m_1^2 - p^2) + D_n(\delta_{2,n} + p\beta_{2,n}\sqrt{c} + m_2^2 - p^2) \\ &+ E_n(\delta_{3,n} + p\beta_{3,n}\sqrt{c} + m_3^2 - p^2) + (\epsilon_n + p\sqrt{c}\gamma_n)\Big\}. \end{aligned}$$

In Equation (5.21) the surface boundary conditions are summarized in a matrix form.

5C The n = 0 contribution and the Prandtl solution

In the developed analytical model, the constants $\beta_{\sigma,n}$ and $\delta_{\sigma,n}$ in (5A.6) and (5A.10), respectively, become singular for $n = 0$. The first term in the Fourier representations of B and U must therefore be treated separately. Note that since the stream function is proportional to $\sin(pY)$, Equation (5A.8) has no $n = 0$ contribution.
For $n = 0$, Equation (5A.1) reduces to $m^6 + m^2 = 0$, which has the solutions $m = 0$ or $m = (-1 \pm i)/\sqrt{2}$. The roots of m that have a positive real part have been omitted. The $n = 0$ contribution to the Fourier representation of

the buoyancy becomes

$$\begin{aligned} B(\forall Y, Z)|_{n=0} &= D_0 \exp\left[(-1+i)Z/\sqrt{2}\right] + E_0 \exp\left[(-1-i)Z/\sqrt{2}\right] \\ &+ c_1 + c_2 \cdot Z, \end{aligned} \tag{5C.1}$$

The last two terms are associated with the two identical roots $m = 0$. They produce, respectively, a constant buoyancy and a buoyancy that increases with height. Both terms violate the boundary condition requiring that the buoyancy vanishes far above the surface, hence both constants c_1 and c_2 must be zero. In order to evaluate the expression for the downslope velocity (5A.12) we must revisit the steps leading to (5A.9) - (5A.11). From the latter equation we find that $\cos(0)g^2\epsilon_0 e^{gZ} = 0$, i.e. $g = 0$. The particular solution U_p, however, is nonzero. Seeking a solution on the form (5A.9) and using the new roots m, we obtain

$$\nabla^2 U_p = -i\delta_{2,0} D_0 \exp\left[(-1+i)Z/\sqrt{2}\right] + i\delta_{3,0} E_0 \exp\left[(-1-i)Z/\sqrt{2}\right].$$

Equating exponents with those in Equation (5C.1) yields $\delta_{2,0} = i$ and $\delta_{3,0} = -i$. The $n = 0$ contribution to the Fourier representation of U is thus

$$U|_{n=0} = iD_0 \exp\left[(-1+i)Z/\sqrt{(2)}\right] - iE_0 \exp\left[(-1-i)Z/\sqrt{(2)}\right]. \tag{5C.2}$$

From the discussion on the surface boundary conditions (Appendix 5B) we know that the buoyancy at the surface is equal to $\mathcal{B}_0$, i.e. $\mathcal{B}_0 = D_0 + E_0$. The no-slip condition implies $0 = iD_0 - iE_0$. With these boundary conditions, the solutions to (5C.1) and (5C.2) become

$$\begin{aligned} B(Y, Z)|_{n=0} &= \mathcal{B}_0 e^{-Z/\sqrt{2}} \cos(Z/\sqrt{2}), \quad \text{and} \\ U(Y, Z)|_{n=0} &= -\mathcal{B}_0 e^{-Z/\sqrt{2}} \sin(Z/\sqrt{2}). \end{aligned}$$

The result should be compared to the Prandtl solution, which in terms of the non-dimensional variables introduced in Section 5.2, is

$$\begin{aligned} B_{Pr}(Z) &= -e^{-Z/\sqrt{2}} \cos\left(Z/\sqrt{2}\right), \quad \text{and} \\ U_{Pr}(Z) &= e^{-Z/\sqrt{2}} \sin\left(Z/\sqrt{2}\right). \end{aligned}$$

The sign is changed in order to ensure consistency with the sign of b_0. In the Prandtl model the negatively buoyant surface is infinitely wide, i.e. the isolation parameter $\mathcal{R}$ is zero. Using $\mathcal{R} = 0$ in (5B.2) yields $\mathcal{B}_0 = -1$ and $\mathcal{B}_n = 0$ for $n > 0$. This shows that the model solution reverts to the Prandtl solution for $\mathcal{R} = 0$.

Summary

The atmosphere is in scientific descriptions frequent divided into different regions, and the region that is adjacent to the earth's surface is called the atmospheric boundary layer (ABL). The structure of this boundary layer, and the atmospheric motions within it, are influenced by several factors such as topography, different surface types (e.g. water, various vegetation types), and the diurnal solar heating. The daytime solar heating produces rising thermals, which in fact are large turbulent eddies. On the other hand, during the night, or the polar winter period, there is no solar heating, but rather a radiative cooling of the ABL, which is responsible for the ABL becoming stably stratified, i.e. the potential temperature increases with height. In the nocturnal stable boundary layer (SBL), the turbulent eddies are much smaller compared to the eddies in the daytime boundary layer.

When a stratified ABL is heated or cooled from below by an inclined surface, a horizontal potential temperature difference may arise between an air parcel close to the slope and one further away but at the same height. This potential temperature difference gives the near-surface air parcel a buoyancy force with respect to its environment. If the air parcel is warmer (i.e. less dense) than its environment, it will start moving up the slope, whereas a parcel that is colder (i.e. denser) than the ambient atmosphere will start descending down the slope. These thermally induced up-slope and downslope flows, are called anabatic and katabatic winds, respectively.

Katabatic winds are characterized by persisting wind profiles exhibiting a wind maximum of the order of several metres per second. The wind maximum is normally located close to the surface, say a couple of metres to tens of metres above the ground. As a consequence hereof, the wind profiles have

large vertical[2] gradients, and the associated wind shear is a key factor in the production of turbulence.
Turbulence is an important feature of katabatic winds, it is responsible for the vertical mixing of momentum and heat in the lowest part of the boundary layer. The mixing effectively transports heat from the boundary layer to the ground, thus acting to heat the surface. The katabatic winds over glaciers also transport heat to the surface. Provided the ice is at the melting temperature, the extra added heat causes melting. This melting has during the last couple of decades caused glacier to retreat, which has been linked to global warming. In atmospheric sciences, the dynamics of the ABL, including katabatic winds, have been studied using various types of numerical models. One such model is dedicated to resolve the motions of the turbulent eddies that are so frequently observed in the ABL, and is called large-eddy simulation (LES). LES builds on some well established properties concerning turbulence, namely that in any turbulent flow there is a large range of eddy-scales, that the large eddies contain the most energy, and as they break forming new smaller eddies, the energy is cascaded down to the small (assumed) isotropic turbulent eddies where it is dissipated. In LES, the motions of the large eddies are explicitly resolved, hence the terminology "resolved motions". These large eddies are distinguished from the small eddies by filtering the governing equations, whereby the filter should lie in the inertial sub-range (that part of the energy spectrum where there is a pure transfer of energy from large eddies to small eddies). The small eddies thus have a characteristic length scale smaller than the filter, and their effect on the mean flow is parameterized in the so-called subfilter scale (SFS) model. It is furthermore important to note that the filter should be (much) larger than the numerical grid distance. If this is not the case, the numerical mesh will influence the model outcome by introducing a numerical dissipation of energy, hence reducing the credibility of the results.

In the early days of LES, the technique was used to study convection in the daytime boundary layer. This boundary layer contains a few regions of stable stratification, e.g. the inversion, which were difficult to simulate because the size of the largest eddies was smaller than the filter. Refining the filter would require using a finer numerical mesh, which was frequently not an option due to the high computational costs. Instead, the problem of poor resolution was mitigated by defining the filter (also called filter parameterizations) such that its size was reduced beyond the numerical grid size. In more recent time, say the last 10 - 15 years, the increase in computer power has made provision for the use of finer numerical grids, which has also made it possible to perform LES studies of the SBL. Despite this increase in computer power, the eddy sizes in the SBL are so small that the chosen filter width is typically of the same order as the numerical grid distance, and is still frequently also allowed to be smaller than the grid distance.

[2]Here vertical means slope-normal.

In Chapter 2, a LES study of an SBL over a plane surface is presented, and the influence of the mesh size on the model results is examined. One way to study this, is to consider the turbulent kinetic energy (TKE) of the resolved motions, the TKE derived from the SFS model, and the sum of these two terms, e.g. the total TKE of the turbulent motions. It is desirable that the bulk of the total TKE comes from the resolved motions, which is found to only be possible if the numerical resolution is high. However, how fine the numerical mesh should be, must be derived from the flow problem.
Chapter 2 also considers how the filter parameterization influences the model results. Of the four parameterizations regarded, one is conceptually correct (e.g. the filter width is larger than the grid distance), whereas the remaining three permit the filter to be smaller than the grid distance. It is found that the conceptually correct filter yields a larger SFS contribution to the total TKE compared to the other simulations. However, the budgets of the resolved TKE show that when the filter is smaller than the grid size, the numerical dissipation of TKE is of the same order as the modelled dissipation. On the other hand, when the filter is larger than the grid distance, this numerical dissipation plays only a minor role compared to the modelled dissipation. Based on these results, and on conceptual arguments, it is recommended using a filter that is larger than the grid distance.
LES codes frequently apply periodic boundary conditions in the horizontal directions, i.e. what flows out of the model domain on one side re-enters on the opposite side. In this way, the boundary layer has an infinite extent in the horizontal directions. For the horizontal ABL, this approximation works well because the horizontal variations in the velocity and potential temperature fields are much smaller than in the vertical direction. On the other hand, the potential temperature field over an inclined surface varies not only with height, but also with downslope distance. Nevertheless, as described in Chapter 3 (published as Axelsen and Van Dop, 2009a), periodic boundary conditions can be retained if one instead assumes that the mean buoyancy is invariant with downslope distance, i.e. the mean difference between the potential temperature of an air parcel participating in the katabatic flow and its environment does not vary along the slope (note that turbulent fluctuations in the buoyancy field are permitted). Observations have shown that this assumption is valid if the environment is strongly stratified or the slope is steep. On the other hand, by invoking the assumption of a periodic buoyancy field in an LES code, the model results must be considered quasi one-dimensional, i.e. the results can only be used to study how the katabatic flow profiles vary with height. The implication of this and other assumptions are discussed more thoroughly in Chapter 3, which presents a recipe for how an LES code that was designed to study the horizontal ABL, can be modified to simulate slope winds.
The LES code's ability to simulate katabatic winds is validated by comparing the model results to observations obtained at the Pasterze (Austria) and the Vatnajökull (Iceland) glaciers. The observations consist of balloon and

mast measurements of the wind speed, wind direction and temperature. At Pasterze, mast measurements of the momentum and buoyancy fluxes were also stored. Only a few data were deemed suitable for the model validation: First, the balloon measurement of the downslope velocity had to agree with the mast measurement, which is frequently difficult close to the surface. Second, a clear stratification of the ambient atmosphere was required. Lastly, since the effort was on simulating downslope winds, observations that showed a substantial cross-slope flow were not used.

The model validation shows relatively good agreement between the simulated and observed profiles of momentum and buoyancy, whereas the momentum and buoyancy flux profiles yield a less satisfactory result. There are several reasons for the discrepancies. Despite the effort to eliminate observations with a cross-slope flow, the Pasterze observations always showed a small cross-slope wind, which generates turbulence and hence affects the structure of the katabatic flow. Also, secondary forcings due to inhomogeneities (e.g. surface undulations, cross-slope variation in the surface buoyancy), gravity waves, etc, also influence the observed katabatic flow, but are not modelled. Lastly, only stationary katabatic winds are simulated, and it is debatable whether the observed downslope winds are truly stationary.

Katabatic winds are moderated by several factors such as ambient winds, the stratification of the ambient atmosphere, the slope angle, and the roughness of the terrain. Although several measurement campaigns have studied the effect of these factors on katabatic flows, it is virtually impossible for these studies to isolate the effect of one single factor. In numerical models, on the other hand, one parameter can be changed whilst keeping the other parameters fixed, yielding results that can be used in a sensitivity study. Chapter 4 (published as Axelsen and Van Dop, 2009b) presents a LES study of the effects of the slope angle, the stability of the ambient atmosphere, and the surface buoyancy flux on katabatic winds. The results show that the height and magnitude of the katabatic wind maximum increase with increasing surface buoyancy flux, but decrease with larger slope angle and ambient stratification. The negative buoyancy in the katabatic layer increases for larger surface buoyancy fluxes and smaller slope angles, whereas it is only slightly affected by a change in the stratification of the ambient atmosphere. The simulations further show that the momentum flux increases from a negative value at the surface to zero at the height of the wind maximum, an that it has a maximum further aloft. The buoyancy flux profiles decrease monotonically from the surface value to zero. These profiles do not decrease linearly as in the horizontal SBL. Instead the buoyancy flux profiles are slightly curved with respect to height in such a way that the buoyancy flux divergence is larger near the surface than further aloft.

The fluxes of momentum and buoyancy are examples of second-order moments. LES can also be used to study higher-order moments such as the TKE budgets of the resolved motions. In the bulk of the boundary layer, they show an approximate balance between shear production and turbulent

dissipation of TKE. Near the wind maximum height, the balance is between the (positive) turbulent transport of TKE and turbulent dissipation.
In the atmospheric boundary layer, turbulence plays a key role in the mixing and transport of momentum and buoyancy. The mixing is frequently mathematically treated using mixing or exchange coefficients. In the SBL, these exchange coefficients for momentum and buoyancy usually differ, i.e. these two properties mix at different rates. The ratio of the momentum exchange to buoyancy exchange is characterized by the Prandtl number. The numerical simulations show that the Prandtl number of the resolved motions is a function of a.o. height and stability. The vertical profiles of the Prandtl number show a mean value close to unity, and that it increases around the wind maximum. There the stability of the flow increases due to the decrease in shear production of turbulence. The simulations further confirm a previously proposed linear relation between the Prandtl number and the stability.
The presentation of the TKE budgets and the Prandtl number was possible because LES is capable of resolving the motions of the largest eddies in the katabatic winds. On the other hand, much simpler, analytical models have previously also been used to study katabatic flows. Two of these are discussed in Chapter 4, namely the classical Prandtl (1942) model, and one of its extensions presented by Grisogono and Oerlemans (2001a,b). From these two analytical models, two linear relations for estimating the surface buoyancy flux based on mean quantities are derived. These relations can also be regarded as parameterizations. One states that the surface buoyancy flux can be estimated from data on the wind maximum height, the ambient stratification, the slope angle, and the surface buoyancy. The second relation is very similar, it estimates the surface buoyancy flux using the same variables as above, except the surface buoyancy is replaced by the magnitude of the wind maximum. These linear relations include proportionality constants that must be empirically obtained. The analytically derived linear relations are verified by the LES results, though the proportionality coefficients differ. The relations are with various success compared to the Pasterze observations. The relation that yields the most satisfactory results is also compared to more idealized data (i.e. time-averaged observations and numerical results from other studies), and the resulting estimates give reasonable results.
Chapter 5 (article accepted for publishing, Axelsen *et al.*, 2009) discusses katabatic flows that are induced by an infinitely long cold strip with limited with. The study is conducted using a newly developed analytical model, which assumes the surface buoyancy to be homogeneous in the downslope direction, but inhomogeneous in the cross-slope direction. The model has been verified by results from a numerical simulation, and is furthermore found to revert to the classical Prandtl model if the strip width goes to infinity.
The analytical model is used to study the effect of the strip width and the slope angle on katabatic winds. It is found that the buoyancy and downslope velocity fields reach maximum values at the centre of the strip, and that they spread

outward in the cross-slope direction. Furthermore, the cross-slope variation in the surface buoyancy produces cross-slope and slope-normal velocities. These two velocity fields combined show the presence of two vortices near each strip edge. One vortex near the ground shows that the air above the cold strip descends towards the surface where it is detrained from the strip region. The air then starts ascending and moves back in over the strip. The second vortex is found further aloft, and shows the opposite circulation: The fluid over the negatively buoyant surface first ascends and detrains from the strip region, then starts to sink and moves back into the strip region.

The cross-slope and slope-normal velocities produced by the new model are in contrast to the Prandtl model, which assumes that the flow is only in the slope-parallel direction. These two analytical models also differ in the vertical profiles of buoyancy and downslope velocity at the strip centre. Compared to the classical Prandtl model, the new model predicts that the downslope velocity profile is less sharp around the wind maximum, and yields a smaller (positive) buoyancy maximum. These predictions are favoured by observations of katabatic winds, e.g. the Pasterze observations showed a 'blunt' wind maximum and no significant region of positive buoyancy. These results indicate the necessity to account for an inhomogeneous surface forcing when modelling katabatic winds.

Samenvatting

In wetenschappelijke beschrijvingen wordt de atmosfeer vaak in lagen ingedeeld. De laag die net boven het aardoppervlak ligt, wordt de atmosferische grenslaag (en: atmopsheric boundary layer, ABL) genoemd. De structuur en de dynamiek van deze grenslaag worden beïnvloed door meerdere factoren. Voorbeelden hiervan zijn de topografie, de verschillen tussen oppervlaktesoorten (water, verschillende vegetatiesoorten) en de dagelijkse opwarming door de zon. In het laatste geval ontstaat er thermiekbellen, die feitelijk grote turbulente wervels zijn. Anderzijds koelt de ABL gedurende de nacht en de polaire winter af, waardoor de ABL stabiel gestratificeerd wordt. Dit kenmerkt zich doordat de potentiële temperatuur[3] met de hoogte toeneemt. In de nachtelijke stabiele grenslaag (en: stable boundary layer, SBL) zijn de turbulente wervels veel kleiner dan de wervels overdag.
Als een gestratificeerde grenslaag door een hellend oppervlak wordt opgewarmd of afgekoeld, ontstaat er een horizontale gradiënt in het potentiële temperatuurveld. Het verschil in potentiële temperatuur tussen een luchtpakketje bij de grond en een verder weg (maar op dezelfde hoogte) geeft het pakketje bij de grond een Archimedeskracht ten opzicht van diens omgeving. In deze beschrijving zal voortaan de Archimedeskracht door de temperatuur of het temperatuurverschil worden vervangen. Als een pakketje warmer (dwz. lichter, positief temperatuurverschil) is dan zijn omgeving, zal het langs de helling omhoog gaan stromen. Een pakketje dat kouder (zwaarder, negatief temperatuurverschil) dan zijn omgeving is, zal langs de helling neerwaarts gaan stromen. Deze thermische geïnduceerde opwaartse en neerwaartse stromingen worden respec-

[3]Dwz. een temperatuur die een drukcorrectie bevat: het is de temperatuur die een luchtpakket zou aannemen als het adiabatisch naar een referentiedruk zou worden verplaatst. Vaak is de referentiedruk gelijk aan de druk bij de grond.

tievelijk anabatische en katabatische stromingen genoemd.
Katabatische stromingen worden gekenmerkt door een aanhoudende wind. De snelheid van de stroming kan wiskundig worden beschreven met behulp van een (vertikaal[4]) snelheidsprofiel. Dit profiel heeft een maximum met een typische waarde van enkele meters per seconde. Het windmaximum bevindt zich enkele meters tot tientallen meters boven de grond. De grote verandering in windsnelheid bij het oppervlak zorgt voor een grote verticale windgradiënt, wat een voorwaarde is voor de productie van turbulentie door windschering.
Turbulentie is een belangrijke eigenschap van katabatische stromingen, omdat deze voor een verticale menging van impuls en warmte in het onderste deel van de grenslaag zorgt. Deze menging is verantwoordelijk voor transport van warmte uit de grenslaag naar de grond, waardoor het oppervlak wordt opgewarmd. De katabatische stromingen boven gletsjers zorgen dus voor opwarming van het ijs. Indien het ijs op het smeltpunt is, zoals in de ablatiezone gedurende de zomerperiode, zal de extra toegevoerde warmte tot smelten leiden. Gletsjers zijn de afgelopen decennia hierdoor gekrompen en dit is gerelateerd aan klimaatveranderingen.
Wetenschappers hebben de dynamische processen in de ABL, inclusief de katabatische stromingen, met behulp van verschillende soorten numerieke modellen bestudeerd. Een van de soorten modellen richt zich op het oplossen van de bewegingsvergelijkingen van de grootste turbulente wervels in de grenslaag en wordt grote-wervel simulatie (en: large-eddy simulation, LES) genoemd. LES baseert zich op eigenschappen van turbulentie: Een turbulente stroming bevat turbulente wervels met verschillende ruimtelijke schalen en de meeste energie zit in de grootste wervels. Als deze grote wervels breken, ontstaan nieuwe (kleinere) wervels en is er een energiecascade naar de kleinere wervels toe. De dissipatie van deze energie vindt plaats op heel kleine schaal, waar de turbulentie (verondersteld) isostroop is. LES lost expliciet de bewegingsvergelijkingen voor de grote wervels op. Deze wervels worden onderscheiden van de kleine wervels door de bewegingsvergelijkingen te filteren, waarbij wordt verondersteld dat het filter in de inertiële sub-range ligt (dat deel van het energiespectrum waar uitsluitend overdracht van energie van grote naar kleine wervels is). De kleine wervels hebben een karakteristieke lengteschaal die kleiner is dan het filter en hun invloed op de gemiddelde stroming wordt geparameteriseerd in het zogenoemde subfilter-scale (SFS) model. Ook moet worden opgemerkt, dat dit filter (veel) groter dan de numerieke roosterafstand dient te zijn. Mocht dat niet het geval zijn, dan veroorzaakt het numerieke rooster een numerieke dissipatie van energie, welke de validiteit van de modelresultaten vermindert.
In het begin werd LES gebruikt om convectie in de ABL te bestuderen. De convectieve grenslaag kent ook gebieden waar de atmosfeer stabiel gestratificeerd is, b.v. de inversie. Dit leidde tot problemen, omdat daar de lengteschaal van de grootste wervels kleiner was dan het filter. Een kleiner filter kiezen

[4]Verticaal betekent hier loodrecht op de helling.

vereist ook een fijner rooster, wat toen veelal niet mogelijk was vanwege de beperkte computercapaciteit. In plaats daarvan werd het probleem benaderd door het filter kleiner dan het rooster te maken. De laatste 10-15 jaar zijn de mogelijkheden van computers steeds groter geworden en kunnen nu fijnere roosters worden gebruikt. Dit heeft tevens LES studies van de SBL mogelijk gemaakt. Ondanks de vooruitgang in de computertechnologie is de turbulente lengteschaal van wervels in de SBL dusdanig klein, dat het filter van dezelfde grootte is als het numerieke rooster.
Een LES studie van een horizontale SBL wordt in hoofdstuk 2 beschreven. Hierin wordt de invloed van de roosterafstand op de modelresultaten bestudeerd. Dit geschiedt door de turbulente kinetische energie (TKE) van de opgeloste schalen, van het SFS model en de totale TKE te bekijken. Het is wenselijk dat het overgrote deel van de TKE uit de opgeloste schalen komt, wat volgens de resultaten alleen mogelijk is indien de numerieke resolutie hoog is. Echter, hoe fijn de numerieke resolutie moet zijn, moet uit het stromingsprobleem worden afgeleid.
In Hoofdstuk 2 wordt ook het effect van het filter op de modelresultaten onderzocht. Vier filters zijn getest, waarvan één conceptueel correct is (dwz. het filter is groter dan de roosterafstand) terwijl de anderen een waarde kleiner dan de roosterafstand toestaan. De resultaten laten zien, dat vergeleken met de overige simulaties, het conceptueel correcte filter een grotere SFS bijdrage aan de totale TKE levert. De TKE budgetten van de opgeloste schalen tonen daarentegen aan, dat alleen het conceptuele filter een kleine numerieke dissipatie teweegbrengt. De overige filters produceren een grotere numerieke dissipatie die dezelfde ordegrootte heeft als de gemodelleerde dissispatie. Gebaseerd op deze resultaten en conceptuele argumenten wordt daarom aanbevolen om een filter te kiezen dat groter dan de roosterafstand is.
In LES worden vaak periodieke randvoorwaarden in de horizontale richtingen toegepast, dwz. wat aan de ene zijde van het domein eruit stroomt, komt aan de andere zijde weer binnen. Als gevolg hiervan is de grenslaag in de horizontale richtingen oneindig lang uitgerekt. Deze aanname werkt goed voor de horizontale ABL, omdat de horizontale veranderingen in het snelheidsveld en potentiële temperatuurveld veel kleiner zijn dan in de verticale richting. Het potentiële temperatuurveld boven een hellend oppervlak varieert daarentegen niet alleen met de hoogte, maar ook langs de helling zelf. Desondanks kunnen periodieke randvoorwaarden worden toegepast als verondersteld wordt dat het gemiddelde temperatuurverschil langs de helling niet verandert, dwz. het gemiddelde temperatuurverschil tussen de katabatische laag en de omgeving is constant (merk op dat turbulente fluctuaties in het temperatuurveld wel zijn toegestaan). Deze aanname berust op waarnemingen van katabatische stromingen in een zeer stabiel medium of boven een steile helling. Het nadeel van de aanname is echter, dat de modelresultaten quasi ééndimensionaal zijn; ze kunnen alleen informatie geven over hoe de katabatische profielen met de hoogte variëren. De implicaties van deze en andere veronderstellingen worden

in Hoofdstuk 3 (gepubliceerd in Axelsen and Van Dop, 2009a) uitvoerig besproken. Daar staat ook beschreven hoe een LES code, geschreven voor de horizontale grenslaag, kan worden aangepast om stromingen boven hellingen te simuleren. In Hoofdstuk 3 wordt ook de geschiktheid van het numerieke model om katabatische stromingen te simuleren onderzocht door modelresultaten met metingen te vergelijken. De waarnemingen zijn van de Pasterze (Oostenrijk) en Vatnajökull (IJsland) gletsjers en bestaan uit ballon- en mastmetingen van windsnelheid, windrichting en temperatuur. De Pasterze-waarnemingen omvatten tevens metingen van de impulsflux en warmtefluxen[5]. Slechts enkele waarnemingen waren voor de modelvalidatie geschikt. Ten eerste moest worden geëist, dat de ballonmetingen van de snelheid goed overeen zouden komen met de mastmetingen. Dat is dichtbij het oppervlak vaak lastig. Ten tweede moest uit de ballongegevens een eenduidige achtergrondstratificatie kunnen worden afgeleid. Verder was een vaak voorkomend verschijnsel een wind die haaks op de helling stond. Omdat de gesimuleerde stromingen alleen langs de helling gericht waren, konden deze metingen niet worden gebruikt.
De modelvalidatie laat een relatief goede overeenkomst zien tussen de gesimuleerde en waargenomen snelheidsprofielen en temperatuurprofielen. De gesimuleerde fluxprofielen van impuls en warmte komen daarentegen minder goed overeen met de metingen. De verschillen worden door meerdere factoren veroorzaakt. Zo laten b.v. de Pasterze data, ondanks de bovengenoemde selectie, altijd een matige stroming haaks op de helling zien. Het effect van deze stroming is het opwekken van turbulentie die de structuur van de katabatische laag beïnvloed. De waargenomen stroming hangt tevens af van fysische processen die niet in het numerieke model zijn meegenomen. Inhomogeniteiten (veranderingen in het oppervlak en variatie in het oppervlaktetemperatuurverschil), zwaartekrachtsgolven enz., zijn hier voorbeelden van. Alleen stationaire katabatische stromingen worden gesimuleerd en het is te betwisten of de waargenomen winden daadwerkelijk stationair zijn.
Katabatische stromingen worden beïnvloedt door meerdere factoren, zoals een achtergrondwind, de stratificatie van de atmosfeer, de hellingshoek en de ruwheid van het oppervlak. Veel meetcampagnes zijn opgezet om het effect van deze factoren op de katabatische stromingen te bestuderen, maar het is nagenoeg onmogelijk het effect van een individuele factor te isoleren. In numerieke modellen daarentegen, kan één parameter worden gevarieerd terwijl de anderen onveranderd blijven. Zo kunnen simulaties met verschillende waardes voor de inputparameters data voor een gevoeligheidsanalyse opleveren. In Hoofdstuk 4 (gepubliceerd in Axelsen and Van Dop, 2009b) wordt LES gebruikt om het effect van de hellingshoek, de stabiliteit van de atmosfeer en oppervlaktewarmteflux op stationaire katabatische stromingen te onderzoeken. De resultaten laten zien dat het windmaximum en diens hoogte toenemen met een toenemende oppervlaktewarmteflux en dat ze daarentegen afnemen als de hel-

[5]Met de warmteflux wordt hier uitsluitend de voelbare warmteflux bedoeld.

lingshoek of de stratificatie toeneemt. Het negatieve temperatuurverschil in de katabatische laag neemt toe indien de warmteflux aan het oppervlak toeneemt of de helling afneemt, terwijl een verandering in de stratificatie amper een effect heeft. De simulaties wijzen ook uit, dat de flux van impuls toeneemt van een negatieve waarde aan het oppervlak en naar nul gaat bij het windmaximum. Op een grotere hoogte heeft de flux een maximum. De warmtefluxprofielen, daarentegen, nemen monotoon af van de grondwaarde naar nul. Deze profielen laten geen lineaire afname zien zoals in de horizontale SBL, maar nemen bij de grond sneller af dan op grotere hoogtes.
De impuls- en warmtefluxen zijn voorbeelden van tweede-orde momenten. LES kan ook worden gebruikt om hogere-orde momenten, zoals de TKE budgetten van opgeloste bewegingen, te bestuderen. In het overgrote deel van de grenslaag tonen deze budgetten een balans aan die bij benadering tussen productie door schering en turbulente dissipatie gevormd wordt. Bij het windmaximum, daarentegen, is er een balans tussen het (positieve) turbulente transport van TKE en turbulente dissipatie.
Turbulentie speelt in de atmosferische grenslaag een belangrijke rol bij het mengen en transporteren van impuls en warmte. De menging wordt vaak beschreven met behulp van uitwisselingscoefficiënten. Deze uitwisselingscoefficiënten voor impuls en warmte verschillen in de SBL, dwz. de snelheden waarmee deze twee eigenschappen van de stroming mengen verschillen. De verhouding tussen de uitwisselingscoeficienten wordt het Prandt-getal genoemd. De simulaties laten zien dat het Prandtl getal van de opgeloste schalen een functie van oa. hoogte en stabiliteit is. De verticale profielen van het Prandtl getal geven een gemiddelde waarde dichtbij één en laten tevens een toename rond het windmaximum zien. Daar neemt de stabiliteit van de stroming toe vanwege een afname in de productie van turbulentie. De simulaties bevestigen ook een eerder voorgestelde lineaire relatie tussen het Prandtl getal en de stabiliteit.
De presentatie van de TKE budgetten en het Prandtl getal is mogelijk, omdat LES de bewegingen van de grootste wervels in een katabatische stroming kan oplossen. Veel simpelere, analytische modellen worden ook gebruikt om katabatische stromingen te bestuderen. Twee van deze modellen, namelijk het Prandtl (1942) model en een meer uitgebreide versie daarvan, gepresenteerd door Grisogono and Oerlemans (2001a,b), worden in Hoofdstuk 4 uitvoerig beschreven. Van deze twee analytische modellen worden twee relaties afgeleid, waarmee de oppervlaktewarmteflux op basis van gemiddelde grootheden kan worden bepaald. Deze relaties kunnen ook als parameterizaties worden beschouwd. De ene gebruikt de windmaximum hoogte, de stratificatie, de hellingshoek en het oppervlaktetemperatuurverschil om de warmteflux aan de grond te bepalen. De tweede relatie lijkt daar veel op, alleen gebruikt die de (grootte van) het windmaximum in plaatst van het oppervlaktetemperatuurverschil. De lineaire relaties bevatten proportionaliteitconstanten die empirisch bepaald moeten worden. De analytische verbanden worden door de LES resultaten bevestigd, alleen verschillen de proportionaliteitsconstanten. Een verdere

vergelijking van de parameterizaties met Pasterze waarnemingen levert minder bevredigende resultaten op. Van de twee relaties vergelijkt de ene het best met de waarnemingen. Deze relatie wordt ook gebruikt om de oppervlakte warmteflux van geïdealiseerde waarnemingen (tijdgemiddelde metingen en numerieke resultaten uit andere studies) te schatten en redelijke resultaten worden gevonden.

Hoofdstuk 5 (geaccepteerd voor publicatie, Axelsen *et al.*, 2009) behandelt katabatische stromingen opgewekt over oneindig lange gletsjers van een beperkte breedte. Het onderzoek is uitgevoerd met behulp van een nieuw ontworpen analytisch model, waarin wordt aangenomen dat het oppervlaktetemperatuurverschil in de richting van de gletsjer homogeen is, maar inhomogeen is in transversale richting. De juistheid van het model werd bevestigd door een numerieke simulatie. Verder wordt aangetoond dat indien de gletsjerbreedte naar oneindig gaat, de oplossing van het klassieke Prandtl model terug wordt gevonden.

Het analytische model is gebruikt om het effect van de gletsjerbreedte en de hellingshoek op katabatische winden te bestuderen. Er is gebleken dat het (positieve) temperatuurverschil en de neerwaartse snelheid maximumwaarden bereiken in het centrum van de ijsvlakte. Het temperatuurverschil en neerwaardse snelheid opgewekt door het koude oppervlak spreiden zich uit in de transversale richting. Daarnaast produceert de transversale variatie in het oppervlaktetemperatuurverschil snelheden in de transversale en verticale richtingen. De gecombineerde snelheidsvelden tonen de aanwezigheid van twee vortexen bij elke gletsjerrand aan. Een vortex dichtbij het oppervlak laat zien dat de lucht boven het koude oppervlakt naar het oppervlak en naar buiten beweegt. De lucht stijgt dan en beweegt zich terug over de ijsvlakte. De tweede vortex bevindt zich verder omhoog en laat een tegenovergestelde circulatie zien. De stroming boven het koude oppervlakte stijgt en beweegt naar buiten, daalt vervolgens en beweegt zich in de richting van het ijs.

De transversale en verticale snelheden in het nieuwe model wijken af van het Prandtl model, wat aanneemt dat de stroming uitsluitend neerwaarts langs de helling is. Deze twee analytische modellen verschillen ook in de verticale profielen van het temperatuurverschil en de snelheid parallel aan de helling. Vergeleken met het klassieke Prandtl model, voorspelt het nieuwe model dat het profiel van de snelheid langs de helling minder scherp is met betrekking tot het windmaximum. Tevens is het maximale temperatuurverschil kleiner dan in het Prandtl model. Dit wordt onderschreven door observaties van katabatische winden. De Pasterze observaties lieten een afgevlakt windmaximum en geen significante laag van positief temperatuurverschil zien. Deze resultaten impliceren dat men rekening dient te houden met inhomogeniteiten in de oppervlakteforcering wanneer katabatische winden worden gemodelleerd.

A

Nomenclature

Table A.1. Summary of symbols used in Chapters 1 - 4. Some of the LES variables are filtered, and are denoted by an overbar. In Chapter 4 this notation is discontinued.

Symbol	Description
	Upper-case Roman
A_s, A_b, A_w	Non-dimensional constants used in various filter parameterizations
BP	Buoyancy production of resolved TKE
C_k	Kolmogorov constant
C_s	Smagorinsky coefficient
DIS	Modelled dissipation of resolved TKE
$\overline{E}(\mathbf{x}, t)$	TKE or resolved motions
G	Filter function
F	Total buoyancy flux
F_s	(Total) Surface buoyancy flux
H	Height scale
K_m^{SFS}	Turbulence exchange coefficient of
K_h^{SFS}, K_b^{SFS}	momentum, heat and buoyancy
MP	Mechanical (shear) production of resolved TKE
N	Brunt-Väisälä frequency
PR	Pressure redistribution of resolved TKE
Pr	Prandtl number
Pr^{SFS}	SFS Prandtl number
$\mathcal{R}$	Residual TKE
Re	Reynolds number
$\overline{S}_{ij}$	Filtered rate of strain tensor

Continued on next page

Symbol	Description
S_i^m ,S^θ	Source / sink of momentum and heat
$\overline{S}_{ij}$	Resolved strain rate tensor
S	Wind speed
T_0	Reference temperature
TR	Transport of resolved TKE
V	Velocity scale

	Lower case Roman
$\overline{b}$	Buoyancy
$\overline{b}_s$	Surface buoyancy
c_ϵ	LES dissipation coefficient
$\overline{e'}$	Filtered SFS TKE
f	Longitudinal autocorrelation
g	Gravitational acceleration
h, $\tilde{h}$	Boundary layer depth (see Section 2.5)
h	Height scale GO model (see Section 4.2)
l_ϵ	Characteristic length scale of turbulent eddies
l_u	Integral length scale
p	Pressure
$\mathbf{u}'(\mathbf{x},\mathbf{t})$	Residual (SFS) velocity field
$\mathbf{u}(\mathbf{x},\mathbf{t})$	Eulerian velocity field
$u(\mathbf{x},t)$	x component of velocity field
$\overline{\mathbf{u}}(\mathbf{x},\mathbf{t})$	Filtered (resolved) velocity field
u_*	Friction velocity
u_m	Magnitude of katabatic wind maximum
t	Time
z_j	Height of katabatic wind maximum
z_0	Roughness height, roughness length

	Upper-case Greek
Δ	Grid spacing
Λ	Local Obukhov length scale
Ω_i	Earth's angular speed of rotation
Θ_a	Ambient potential temperature

	Lower-case Greek
α	Slope angle
δ_{ij}	Kronecker delta
ε	Numerical error

Continued on next page

Symbol	Description
ϵ	Rate of dissipation of TKE
ϵ_{ijk}	Levi-Civita symbol
κ	von Karman constant (Section 2.5.2)
κ	Wave number
κ_ϵ, κ_λ, κ_Δ	Wave number associated with the length scales of the most energetic eddies, filter width, and grid distance
λ	Filter width
λ_b, λ_s	Filter widths based on buoyancy and shear
ν	Kinematic viscosity
ν_r	Residual eddy viscosity
$\overline{\pi}$	Filtered modified pressure
ρ	Density
ρ_0	Reference density
σ_θ, σ_u, σ_v, σ_w	Standard deviations of filtered temperature fluctuations and the filtered velocity fluctuations ($\overline{u}$, $\overline{v}$, $\overline{w}$).
τ_{osc}	Time scale of katabatic flow
τ	Total momentum flux
τ_{ij}^{SFS}	Residual stress tensor
$\tau_{\theta j}^{\text{SFS}}$, τ_{bj}^{SFS}	SFS heat and buoyancy flux
θ	Potential temperature
ζ	Nondimensional height

Table A.2. Summary of symbols frequently used in Chapter 5. Capitol variable are non-dimensional. Their dimensional counterparts are not included here.

Symbol	Description
B, B_{Pr}	Buoyancy, Prandtl profile of buoyancy
L_c, L_{ntrl}	Widths of cold and neutrally buoyant surfaces
N	Brunt-Väisälä frequency
$\mathcal{R}$	Isolation parameter
Ψ	Stream function
U, V, W	Velocity components
U_{Pr}	Prandtl profile of downslope velocity
X, Y, Z	Coordinates

Table A.3. Abbreviations

	Abbreviations
ABL	Atmospheric boundary layer
CBL	Convective boundary layer
GO01(a,b)	Grisogono and Oerlemans (2001a,b)
LES	Large-eddy simulation
LLJ	Low-level jet
NBL	Neutral boundary layer
S90	Schumann (1990)
SBL	Stable boundary layer
SFS	Subfilter scale
TKE	Turbulent kinetic energy
ZH04	Zhong and Whiteman (2004)

Bibliography

Abramowitz, M. and Stegun, I. A. (1964). *Handbook of mathematical functions with formulas, graphs and mathematical tables*. National Bureau of Standards Applied Mathematics Series NO. 55, US Dept. of Commerce; Washington D.C.

Anderson, P. S. (2009). Measurement of Prandtl number as a function of Richardson number avoiding self-correlation. *Bound.-Layer Meteorol.*, **131**, 345–362.

Andrén, A. (1994). The structure of stably stratified atmospheric boundary layers: A large-eddy simulation study. *Quart. J. Roy. Meteorol. Soc.*, **121**, 961–985.

Andrén, A., Brown, A., Graf, J., Mason, P. J., Moeng, C. H., Nieuwstadt, F. T. M., and Schumann, U. (1994). Large-eddy simulation of a neutrally stratified boundary layer: An intercomparison of four computer codes. *Quart. J. Roy. Meteorol. Soc.*, **120**, 1457–1484.

Arritt, R. and Pielke, R. (1986). Interactions of nocturnal slope flows with ambient winds. *Bound.-Layer Meteorol.*, **37**, 183–195.

Asselin, R. (1972). Frequency filter for time integration. *Mon. Wea. Rev.*, **100**, 487–490.

Axelsen, S. L. and Van Dop, H. (2009a). Large-eddy simulation of katabatic winds. Part I: Comparison with observations. *Acta Geophysica.*, **57**(4), 803 – 836. DOI: 10.2478/s11600-009-0041-6.

Axelsen, S. L. and Van Dop, H. (2009b). Large-eddy simulation of katabatic winds. Part II: Sensitivity study and comparison with analytical models. *Acta Geophysica.*, **57**(4), 837 – 856. DOI: 10.2478/s11600-009-0042-5.

Axelsen, S. L., Shapiro, A., Fedorovich, E., and Van Dop, H. (2009). Analytical solution for katabatic flow induced by an isolated cold strip. *Environ. Fluid Mech.* DOI: 10.1007/s10652-009-9158-z Accepted for publishing.

Baas, P., Steeneveld, G. J., Van de Wiel, B. J. H., and Holtslag, A. A. M. (2006). Exploring self-correlation in flux-gradient relationships for stably stratified conditions. *J. Atmos. Sci.*, **63**, 3045–3054.

Ball, F. K. (1956). The theory of strong katabatic winds. *Aust. J. Phys.*, **9**, 373–386.

Bange, J. and Roth, R. (1999). Helicopter-borne flux measurements in the nocturnal boundary layer over land - a case study. *Bound.-Layer Meteorol.*, **920**, 295–325.

Banta, R. M., Olivier, L. D., Levinson, D. H., and Ruffieux, D. (1995). Influence of canyon-induced flows on flow and dispersion over adjacent plains. *Theor. Appl. Climatol.*, **52**, 27–42.

Banta, R. M., Shepson, P. B., Bottenheim, J. W., Anlauf, K. G., Wiebe, H. A., Gallant, A., Biesenthal, T., Olivier, L. D., Zhu, C.-J., McKendry, I. G., and Steyn, D. G. (1997). Nocturnal cleansing flows in a tributary valley. *Atmos. Environ.*, **31**, 2147–2162.

Basu, S. and Porté-Agel, F. (2006). Large-eddy simulation of stably stratified atmospheric boundary layer turbulence: A scale-dependent dynamic modeling approach. *J. Atmos. Sci.*, **63**, 2074 – 2091.

Basu, S., Porté-Agel, F., Foufoula-Georgiou, E., Vinuesa, J.-F., and Pahlow, M. (2005). Revisiting the local scaling hypothesis in stably stratified atmospheric boundary-layer turbulence: an integration of field and laboratory measurement with large-eddy simulations. *Bound.-Layer Meteorol.*

Beare, R. J. *et al.* (2006). An intercomparison of large-eddy simulations of the stable boundary layer. *Bound.-Layer Meteorol.*, **118**, 247– 272 .

Beare, R. J. and MacVean, M. K. (2004). Resolution sensitivity and scaling of large-eddy simulations of the stable boundary layer. *Bound.-Layer Meteorol.*, **112**, 257–281.

Beljaars, A. and Holtslag, A. A. M. (1991). Flux parameterization over land surfaces for atmospheric models. *J. Appl. Meteorol.*, **30**, 327–341.

Boris, J. P., Grinstein, F. F., Oran, E. S., and Kolbe, R. L. (1992). New insights into large eddy simulation. *Fluid Dyn. Res.*, **10**, 199–228.

Bromwich, D. H., Cassano, J. J., *et al.* (2001). Mesoscale modeling of katabatic winds over greenland with the polar mm5. *Mon. Wea. Rev.*, **129**, 2290–2309.

Brown, A. R., Derbyshire, S. H., and Mason, P. J. (1994). Large-eddy simulation of stable atmospheric boundary layers with a revised stochastic subgrid model. *Quart. J. Roy. Meteorol. Soc.*, **120**, 373–407.

Businger, J. A., Wyngaard, J. C., Izumi, Y., and Bradley, E. F. (1971). Flux profile relationships in the atmospheric boundary layer. *J. Atmos. Sci.*, **28**, 181–189.

Chiba, O. and Kobayashi, S. (1986). A study of the structure of low-level katabatic winds at Mizuho station, East Antarctica. *Bound.-Layer Meteorol.*, **37**, 343–355.

Cuijpers, J. W. M. (1990). Subgrid parametrization in a large-eddy simulation model. In *Ninth Symp. on Turbulence and Diffusion*, pages 176–179. Roskilde, Denmark, Amer. Meteorol. Soc.

Cuijpers, J. W. M. (1994). *Large-eddy simulation of cumulus convection*. Ph.D. thesis, IMAU, Utrecht University.

Cuxart, J. and Jiménez, M. A. (2007). Mixing processes in a nocturnal low-level jet: an LES study. *J. Atmos. Sci.*, **64**, 1666–1679.

Deardorff, J. W. (1976). On the entrainment rate of a stratocumulus-topped mixed layer. *Quart. J. Roy. Meteorol. Soc.*, **102**, 563–582.

Deardorff, J. W. (1980). Stratocumulus-capped mixed layers derived from a three-dimensional model. *Bound.-Layer Meteorol.*, **18**, 495–527.

Denby, B. (1999). Second-order modelling of turbulence in katabatic flows. *Bound.-Layer Meteorol.*, **92**, 67–100.

Denby, B. and Greuell, W. (1999). The use of bulk and profile methods under conditions of strong katabatic flow. Kluwer Academic Publishers.

Doran, J. C. and Horst, T. W. (1983). Observations and models of simple nocturnal slope flows. *J. Atmos. Sci.*, **40**, 708–717.

Dyer, A. (1974). A review of flux-profile relationships. *Bound.-Layer Meteorol.*, **7**, 363–372.

Egger, J. (1981). On the linear two-dimensional theory of thermally induced slope winds. *Beitr. Z. Phys. Atmos.*, **54**, 465–481.

Egger, J. (1985). Slope winds and the axisymmetric circulation over Antarctica. *J. Atmos. Sci.*, **42**, 1859–1867.

Egger, J. (1990). Thermally forced flows: Theory. In W. Blumen, editor, *Atmospheric processes over complex terrain*. Am. Met. Soc.

Ellison, T. H. and Turner, J. S. (1959). Turbulent entrainment in stratified flows. *J. Fluid Mech.*, **6**, 423–448.

Fedorovich, E. and Shapiro, A. (2009). Structure of numerically simulated katabatic and anabatic flows along steep slopes. *Acta Geophysica.* DOI: 10.2478/s11600-009-0027-4.

Fedorovich, E., Nieuwstadt, F. T. M., and Kaiser, R. (2001). Numerical and laboratory study of a horizontally evolving convective boundary layer. Part 1: Transition regimes and development of the mixed layer. *J. Atmos. Sci.*, **58**, 70 – 86.

Fleagle, R. G. (1950). A theory of air drainage. *J. Meteorol.*, **7**, 227–232.

Foken, T. (1997). On the turbulence structure in the stable boundary layer over the Greenland ice sheet. *Bound.-Layer Meteorol.*, **85**, 111–136.

Foken, T. (2006). 50 years of the Moning-Obukhov similarity theory. *Bound.-Layer Meteorol.*, **119**, 431–447.

Garratt, J. R. (1992). *The Atmospheric Boundary Layer*. Cambridge University Press. 316 pp.

Germano, M., Piomelli, U., Moin, P., and Cabot, W. H. (1991). A dynamic sub-grid scale eddy viscosity model. *Phys. Fluids*, **3**, 1760–1765.

Geurts, B. J. (2004). *Elements of direct and large-eddy simulation*. Edwards, New York.

Giesen, R., Andreassen, L., Van den Broeke, M., and Oerlemans, J. (2009). Comparison of the meteorology and surface energy balance at Storbreen and Midtdalsbreen, two glaciers in Southern Norway. *The Cryosphere*, **3**, 57 – 74.

Giesen, R. H., Van den Broeke, M. R., Oerlemans, J., and Andreassen, L. M. (2008). Surface energy balance in the ablation zone of Midtdalsbreen, a glacier in Southern Norway: Interannual variability and the effect of clouds. *J. Geophys. Res.*, **113**, 1–17.

Glendening, J. W. and Haack, T. (2001). Influence of advection differencing error upon large-eddy simulation accuracy. *Bound.-Layer Meteorol.*, **98**, 127–153.

Grachev, A. A., Andreas, E. L., Fairall, C. W., Guest, P. S., and Persson, P. O. G. (2007). On the turbulent Prandtl number in the stable atmospheric boundary layer. *Bound.-Layer Meteorol.*, **125**, 329–341.

Grisogono, B. (2003). Post-onset behaviour of the pure katabatic flow. *Bound.-Layer Meteorol.*, **107**, 157 – 175.

Grisogono, B. and Oerlemans, J. (2001a). Katabatic flow: Analytic solution for gradually varying eddy diffusivities. *J. Atmos. Sci.*, **58**, 3349 – 3354.

Grisogono, B. and Oerlemans, J. (2001b). A theory for the estimation of surface fluxes in simple katabatic flows. *Quart. J. Roy. Meteorol. Soc.*, **127**, 2725 – 2739.

Grisogono, B., Jericevic, A., and Kraljevic, L. (2007). The low-level katabatic jet height versus Monin-Obukhov height. *Quart. J. Roy. Meteorol. Soc.*, **133**, 2133 – 2136.

Gutman, L. N. and Malbakhov, V. M. (1964). On the theory of katabatic winds of Antarctica. *Met. Issled.*, **9**, 150 – 155. In Russian.

Gutman, L. N. and Melgarejo, J. W. (1981). On the laws of geostrophic drag and heat transfer over a slightly inclined terrain. *J. Atmos. Sci.*, **38**, 1714 – 1724.

Haiden, T. and Whiteman, C. D. (2005). Katabatic flow mechanisms on a low-angle slope. *J. Appl. Meteorol.*, **44**, 113–126.

Hartogenisis, O. K. and De Bruin, H. A. R. (2005). Monin-Obukhov similatity functions of the structure parameter of temperature and turbulent kinetic energy dissipation rate in the stable boundary layer. *Bound.-Layer Meteorol.*, **116**, 253–276.

Holton, J. R. (1992). *An introduction to dymamical meteorology*. Academic Press.

Horst, T. W. and Doran, J. C. (1986). Nocturnal drainage flow on simple slopes. *Bound.-Layer Meteorol.*, **34**, 263–286.

Howell, J. F. and Sun, J. (1999). Surface-layer fluxes in stable conditions. *Bound.-Layer Meteorol.*, **90**, 495–520.

Hunt, J. C. R., Stretch, D. D., and Britter, R. E. (1988). Length scales in stably stratified turbulent flows and their use in turbulence models. In J. S. Puttock, editor, *Stably stratified Flows and Dense Gas Dispersion*, pages 285–321. Clarendon Press.

Jonker, H. J. J., Duynkerke, P. G., and Cuijpers, J. W. M. (1999). Mesoscale fluctuations in scalars generated by boundary layer convection. *J. Atmos. Sci.*, **56**, 801–808.

Kavcic, I. and Grisogono, B. (2007). Katabatic flow with Coriolis effect and gradually varying eddy diffusivity. *Bound.-Layer Meteorol.*, **125**, 377 – 387.

Klein, T., Heinemann, G., Bromwic, D. H., Cassano, J. J., and Hines, K. M. (2001). Mesoscale modeling of katabatic winds over Greenland and comparisons with AWS and aircraft data. *Meteorol. Atmos. Phys.*, **78**, 115–132.

Kodoma, Y., Wendler, G., and Ishikawa, N. (1989). The diurnal variation of the boundary layer in summer in Adelie Land, Eastern Antarctica. *J. Appl. Meteorol.*, **28**, 16–24.

Kondo, H. (1984). The difference of the slope wind between day and night. *J. Meteorol. Soc. Jap.*, **62**, 224–233.

Kosović, B. and Curry, J. A. (2000). A large eddy simulation study of a quasi-steady, stably stratified atmospheric bounday layer. *J. Atmos. Sci.*, **57**, 1052–1068.

Kreyszig, E. (1999). *Advanced engeneering mathematics*. John Wiley and Sons, Inc. 8th edition.

Kundu, P. K. and Cohen, I. M. (2004). *Fluid Mech.* Elsevier Academic Press.

Leonard, A. (1974). Energy cascade in large-eddy simulation of turbulent fluid flow. *Adv. Geophys.*, **18**, 237–248.

Lilly, D. K. (1968). Models of cloud-topped mixed layers under a strong inversion. *Quart. J. Roy. Meteorol. Soc.*, **94**, 292–309.

Lykosov, V. N. and Gutman, L. N. (1972). Turbulent boundary layer above a sloping underlying surface. *Izv. Acad. Sci. USSR, Atmos. Ocean. Phys.*, **8**, 799–809.

Mahrt, L. (1982). Momentum balance of gravity flows. *J. Atmos. Sci.*, **39**, 2701–2711.

Mahrt, L. (1998). Stratified atmospheric boundary layers and breakdown of models. *Theoret. Comput. Fluid Dyn.*, **11**, 263–279.

Mahrt, L. (2001). Shallow drainage flows. *Bound.-Layer Meteorol.*, **101**, 243–260.

Mahrt, L. and Larsen, S. (1990). Relation of slope winds to the ambient flow over gentle terrain. *Bound.-Layer Meteorol.*, **53**, 93–102.

Manins, P. C. and Sawford, B. L. (1979). A model of katabatic winds. *J. Atmos. Sci.*, **36**, 619–630.

Mason, P. J. and Derbyshire, S. H. (1990). Large-eddy simulation of the stably-stratified atmospheric boundary layer. *Bound.-Layer Meteorol.*, **53**, 117–162.

Meesters, A. G. C. A., Bink, N. J., Henneken, E. A. C., Vugts, H. F., and Cannemeijer, F. (1997a). Katabatic wind profiles over the Greenland ice sheet: Observation and modelling. *Bound.-Layer Meteorol.*, **85**, 475–496.

Meesters, A. G. C. A., Bink, N. J., Vugts, H. F., Cannemeijer, F., and Henneken, E. A. C. (1997b). Turbulence observations above a smooth melting surface on the Greenland ice sheet. *Bound.-Layer Meteorol.*, **85**, 81–110.

Monti, P., Fernando, H. J. S., Princevac, M., Chan, W. C., Kowalewski, T. A., and Pardyjak, E. R. (2002). Observations of flow and turbulence in the nocturnal boundary layer over a slope. *J. Atmos. Sci.*, **59**, 2513–2534.

Nappo, C. J. (2002). *An introduction to atmospheric gravity waves*. Academic Press.

Nappo, C. J. and Rao, K. (1987). A model study of pure katabatic flows. *Tellus*, **39A**, 61–71.

Nieuwstadt, F. T. M. (1984). The turbulent structure of the stable nocturnal boundary layer. *J. Atmos. Sci.*, **41**, 2202–2216.

Nieuwstadt, F. T. M. (1990). Direct and large-eddy simulation of free convection. In *Proc. 9th International Heat Transfer Conference*. Amer. Soc. Mech. Eng.: New York.

Nieuwstadt, F. T. M. and Brost, R. A. (1986). The decay of convective turbulence. *J. Atmos. Sci.*, **43**, 532–546.

Oerlemans, J. (1994). Quantifying global warming from retreat of glaciers. *Science*, **264**, 243–245.

Oerlemans, J. (1998). The atmospheric boundary layer over melting glaciers. In *Clear and cloudy boundary layers*, pages 129–153. Netherlands Academy of Siences (KNAW).

Oerlemans, J. and Klok, E. J. (2002). Energy balance of a glacier surface: Analysis of automatic weather station data from Morteratschgletcher,Switzerland. *Arct. Antarct. Alp. Res.*, **34**, 477–485.

Oerlemans, J., Björnson, H., Kuhn, M., Obleitner, F., Palsson, F., Smeets, C. J. J. P., Vugts, H. F., and De Wolde, J. (1999). Glacio-meteorological investigations on Vatnajökull, Iceland, summer 1996: An overview. *Bound.-Layer Meteorol.*, **92**, 3–26.

Ohya, Y. (2001). Wind tunnel study of atmospheric stable boundary layers over a rough surface. *Bound.-Layer Meteorol.*, **98**, 57–82.

Papadopoulos, K. H. and Helmis, C. G. (1999). Evening and morning transition of katabatic flows. *Bound.-Layer Meteorol.*, **92**, 195–227.

Papadopoulos, K. H., Helmis, C. G., Soilemes, A. T., Kalogiros, J., Papageorgas, P. G., and Asimakopoulos, D. N. (1997). The structure of katabatic flows down a simple slope. *Quart. J. Roy. Meteorol. Soc.*, **123**, 1581–1601.

Parish, T. R. (1984). A numerical study of strong katabatic winds over Antarctica. *Mon. Wea. Rev.*, **112**, 545–554.

Parmhed, O., Oerlemans, J., and Grisogono, B. (2004). Describing surface fluxes in katabatic flow on Breidamerkurjökull, Iceland. *Quart. J. Roy. Meteorol. Soc.*, **130**, 1137–1151.

Pettré, P., Renaud, M. F., Renaud, R., Déqué, M., and André, J. C. (1990). Study of the influence of katabatic flows on the Antarctic circulation using GCM simulations. *Meteorol. Atmos. Phys.*, **43**, 187–195.

Pope, S. B. (2000). *Turbulent Flows*. Cambridge University Press.

Prandtl, L. (1942). *Führer durch die Strömungslehre*. Vieweg u. Sohn, Braunschweig.

Raasch, S. and Etling, D. (1991). Numerical simulation of rotating turbulent thermal convection. *Beitr. Phys. Atmos.*, **64**, 185–199.

Rao, K. S. and Snodgrass, H. F. (1981). A nonstationary nocturnal drainage flow model. *Bound.-Layer Meteorol.*, **20**, 309–320.

Sagaut, P. (1998). *Large-Eddy Simulation for Incompressible Flow*. Springer. 319pp.

Schumann, U. (1990). Large-eddy simulation of the up-slope boundary layer. *Quart. J. Roy. Meteorol. Soc.*, **116**, 637–670.

Sen Roy, S. and Balling Jr., R. C. (2004). Analysis of Hawaiian diurnal rainfall patterns. *Theor. Appl. Climatol*, **79**, 209–214.

Shapiro, A. and Fedorovich, E. (2004). Prandtl number dependence of unsteady natural convection along a vertical plate in a stably stratified fluid. *Int. J. Heat and Mass Transfer*, **47**, 4911–4927.

Shapiro, A. and Fedorovich, E. (2006). Natural convection in a stably stratified fluid along vertical plates and cylinders with temporally periodic surface temperature variations. *J. Fluid Mech.*, **546**, 295–311.

Shapiro, A. and Fedorovich, E. (2007). Katabatic flow along a differentially cooled sloping surface. *J. Fluid Mech.*, **571**, 149–175.

Shapiro, A. and Fedorovich, E. (2008). Coriolis effects in homogeneous and inhomogeneous katabatic flows. *Quart. J. Roy. Meteorol. Soc.*, **134**, 353 – 370.

Siebesma, A. P. and Cuijpers, J. W. M. (1995). Evaluation of parametric assumptions for shallow cumulus convection. *J. Atmos. Sci.*, **52**, 650–666.

Siebesma, A. P. and Holtslag, A. A. M. (1996). Model impacts on entrainment and detrainment rates in shallow cumulus convection. *J. Atmos. Sci.*, **53**, 2354–2364.

Skyllingstad, E. D. (2003). Large-eddy simulaion of katabatic flows. *Bound.-Layer Meteorol.*, **106**, 217–243.

Smeets, C. J. P. P., Duynkerke, P. G., and Vugts, H. F. (1998). Turbulence characteristics of the stable boundary layer over a mid-latitude glacier. Part I: A combination of katabatic and large scale forcing. *Bound.-Layer Meteorol.*, **87**, 117–145.

Smeets, C. J. P. P., Duynkerke, P. G., and Vugts, H. F. (1999). Observed wind profiles and turbulence fluxes over an ice surface with changing surface roughness. *Bound.-Layer Meteorol.*, **92**, 99–121.

Smith, C. M. and Skyllingstad, E. D. (2005). Numerical simulation of katabatic flow with changing slope angle. *Mon. Wea. Rev.*, **133**, 3065–3080.

Söderberg, S. and Parmhed, O. (2006). Numerical modelling of katabatic flow over a melting outflow glacier. *Bound.-Layer Meteorol.*, **120**, 509–534.

Soler, M. R., Infante, C., Buenestado, P., and Mahrt, L. (2002). Observations of nocturnal drainage flow in a shallow gully. *Bound.-Layer Meteorol.*, **105**, 253–273.

Solomon, S., Qin, D., Manning, M., *et al.*, editors (2007). *Climate change 2007. Tthe physical sience basis*. Cambridge University press. Working group 1. Contribution to the Fourth Assessment.

Stiperski, I., Kavcic, I., Grisogono, B., and Durran, D. R. (2007). Including Coriolis effects in the Prandtl model for katabatic flow. *Quart. J. Roy. Meteorol. Soc.*, **133**, 101– 106.

Strang, E. J. and Fernando, H. J. S. (2001). Vertical mixing and transports through a stratified shear layer. *J. Phys. Oceanography*, **31**, 2026– 2048.

Stull, R. B. (1988). *An introduction to Boundary Layer Meteorology*. Kluwer Academic Publishers. 666 pp.

Van As, D. and Van den Broeke, M. R. (2007). Causes of the variability in the summertime Antarctic boundary-layer climate. *Int. J. Climatol.*, **27**, 1735–1751.

Van den Berg, W. J., Van den Broeke, M. R., and Van Meijgaard, E. (2008). Spatial structures in the heat budget of the Antarctic atmospheric boundary layer. *The Cryosphere*, **2**, 1–12.

Van den Broeke, M., Van Lipzig, N., and Van Meijgaard, E. (2002). Momentum budget of the East-Antarctic atmospheric boundary layer: results of a regional climate model. *J. Atmos. Sci.*, **59**, 3117–3129.

Van den Broeke, M. R. (1997a). Momentum, heat, and moisture budgets of the katabatic wind layer over a midlatitude glacier in summer. *J. Appl. Meteorol.*, **36**, 763–774.

Van den Broeke, M. R. (1997b). Structure and diurnal variations of the atmospheric boundary layer over a mid-latitude glacier in the summer. *Bound.-Layer Meteorol.*, **83**, 183–205.

Van den Broeke, M. R., Van de Wal, R. S. W., and Wild, M. (1997). Representation of Antarctic katabatic winds in a high resolution GCM and a note on their climate sensitivity. *J. Clim.*, **10**, 3111–3130.

Van der Avoird, E. and Duynkerke, P. G. (1999). Turbulence in a katabatic flow. does it resemble turbulence in stable boundary layers over flat surfaces? *Bound.-Layer Meteorol.*, **92**, 39 – 66.

Van Dop, H. and Axelsen, S. L. (2007). Large eddy simulation of the stable boundary-layer: A retrospect to Nieuwstadt's early work. *Flow Turb. Combust.*, **79**, 235–249.

Van Lipzig, N. P. M., Van Meijgaard, E., and Oerlemans, J. (1999). Evalutation of a regional atmospheric model using measurements of surface heat exchange processes from a site in Antarctica. *Mon. Wea. Rev.*, **127**, 1994–2011.

White, P. W. (2003). IFS documentation cycle CY23r4 Part IV: Physical processes. Technical report, European Centre for Medium-Range Weather Forecasts, Reading, UK. 166pp.

Whiteman, C. D. (2000). *Mountain Meteorology: Fundamentals and Applications*. Oxford University Press.

Whiteman, C. D. and Zhong, S. (2008). Downslope flows on a low-angle slope and their interactions with valley inversions. Part I: Observations. *J. Appl. Meteorol. Climatol.*, **47**, 2023–2038.

Wicker, L. J. and Skamarock, W. C. (2002). Time-splitting methods for elastic models using forward time schemes. *Mon. Wea. Rev.*, **130**, 2088–2097.

Wyngaard, J. C. (2004). Toward numerical modelling in the "Terra Incognita". *J. Atmos. Sci.*, **61**, 1816–1826.

Yamada, T. (1983). Simulations of nocturnal drainage flows by a q^2l turbulence closure model. *J. Atmos. Sci.*, **40**, 91–106.

Zhong, S. and Whiteman, C. D. (2004). The dynamics of drainage flows developed on a low angle slope in a large valley. Technical report, 11th Conference on mountain meteorology and mesoscale Alpine program annual meeting, Bartlett, New Hampshire.

Zhong, S. and Whiteman, C. D. (2008). Downslope flows on a low-angle slope and their interactions with valley inversions. Part II: Numerical modeling. *J. Appl. Meteorol. Climatol.*, **47**, 2039–2057.

Zilitinkevich, S. S. and Esau, I. N. (2007). Similarity theory and calculation of turbulent fluxes at the surface for the stably stratified atmospheric boundary layer. *Bound.-Layer Meteorol.*, **125**, 193–205.

Zilitinkevich, S. S., Elperin, T., Kleeorin, N., and Rogachevskii, I. (2007). Energy- and flux- budget (efb) turbulence closure model for stably stratified flows. part i: steady state, homogeneous regimes. *Bound.-Layer Meteorol.*, **125**, 167–191.

Zilitinkevich, S. S., Elperin, T., Kleeorin, N., Rogachevskii, I., Esau, I. N., Mauritsen, T., and Miles, M. W. (2008). Turbulence energetics in stably stratified geophysical flows: Strong and weak mixing regimes. *Quart. J. Roy. Meteorol. Soc.*, **134**, 793–799.

Scientific publications

Axelsen, S. L. and Van Dop, H. (2009a). Large-eddy simulation of katabatic winds. Part I: Comparison with observations. *Acta Geophysica.*, **57**(4), 803 – 836. DOI: 10.2478/s11600-009-0041-6.

Axelsen, S. L. and Van Dop, H. (2009b). Large-eddy simulation of katabatic winds. Part II: Sensitivity study and comparison with analytical models. *Acta Geophysica.*, **57**(4), 837 – 856. DOI: 10.2478/s11600-009-0042-5.

Axelsen, S. L., Shapiro, A., Fedorovich, E., and Van Dop, H. (2009). Analytical solution for katabatic flow induced by an isolated cold strip. *Environ. Fluid Mech.* DOI: 10.1007/s10652-009-9158-z Accepted for publishing.

Van Dop, H. and Axelsen, S. L. 2007:. Large eddy simulation of the stable boundary-layer: A retrospect to Nieuwstadt's early work. *Flow Turbulence Combustion*, **79**, 235–249.

Dankwoord

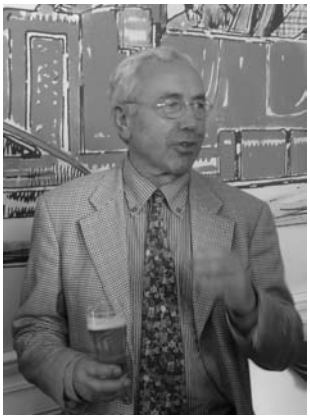

Het feit dat dit boek er eindelijk is, heb ik aan Han te danken. Toen ik aan mijn afstudeerproject werkte, kreeg ik te horen dat er op het IMAU een plek was voor een promovendus grenslaagmeteorologie. Ondanks dat ik nog maanden aan mijn scriptie moest werken, heeft Han me de baan aangeboden. Uiteraard ben ik ook Hans (met een 's') dankbaar voor het feit dat deze positie werd bekostigd.
Grenslaagmeteorologie en large-eddy simulation waren soms taaie en ondoorgrondelijke onderwerpen, maar veelal ook heel inspirerende werk. Op de kamer van Han kon ik al mijn ideeën, gedachten en vragen kwijt; snel aankloppen en vervolgens Han's kantoor binnenvallen was vrijwel altijd mogelijk. Han, ik wens je ook te bedanken voor het meedenken. Als een promovendus een onderzoeker in kinderschoenen is, dan is het geruststellend om te weten dat de begeleider meedenkt over hoe je de veters het best kunt strikken.

In the summer of 2007, Han told me that a professor from Oklahoma would pay us a short visit. "Sure, I can prepare some plots", I said. A couple of days later Evgeni showed up. Large-eddy simulation of katabatic winds was (and still is) a novelty, so he was really interested in our work. At the end of our conversation, Evgeni invited me to visit Oklahoma for a couple of months. That's when my American adventure began. I would like to express my gratitude towards Evgeni not only for giving me this opportunity, but also for helping me around in a new place and in a new culture, and of course for all the scientific input I received during my stay in Norman and after I returned to Utrecht.

After getting somewhat settled in Norman, work began. I had long wanted to do some analytical work, so the math-genius Alan took it upon himself to show me some tricks of the trade. During my stay in Norman, I would frequently run into mathematical challenges, and Alan would enthusiastically explain how they could be solved. When I returned to Utrecht, a new conceptual model for katabatic winds induced by inhomogeneous surface forcing had been born. Some details still had to be resolved, and by e-mail Alan helped me out.

Waar begon het nou eigenlijk allemaal? In het eerste jaar van de masteropleiding heb ik vakken gevolgd. Een paar van de behandelde onderwerpen vond ik dusdanig interessant dat ik daar een heel jaar aan wilde wijden. Toen ik een afstudeerproject moest kiezen, heb ik vooral gekeken naar de orginaliteit van het onderzoek en wat ik van de begeleider kon verwachten. Wolkenonderzoek bij Stephan was een makkelijke keuze. Het gold als een ongeschreven regel, dat we minstens om de twee dagen bijeenkwamen om de laatste resultaten te bespreken. Mijn wens om door te willen leren en de enthousiaste samenwerking met Stephan waren de twee belangrijkste redenen om voor een promovenduspositie te willen solliciteren.

Tijdens het afstuderen zat ik samen met Jeroen in de studentenkamer. Elke dag werd er om 10 en 15 uur koffie omgeroepen en wij stonden veelal als eersten bij de koffiekan. Toen Jeroen een half jaar na mij aan zijn promotieonderzoek begon, zetten we die traditie voort. Alles wat ik meemaakte, zowel blijdschap als frustratie uit de werk- of privesfeer, kon ik bij Jeroen kwijt. Ook de andere mensen van het IMAU wens ik te bedanken voor input en gezelligheid en een paar mensen in het bijzonder: Rianne was een paar maanden voor mij aan haar onderzoek begonnen en had vaak net die praktische dingen onderzocht die ik moest weten. Erik wil ik bedanken voor alle computerhulp. Ook bedankt aan de kamergenoten voor alle gesprekken. Uiteindelijk heb ik in de loop der jaren er drie van versleten, Hylke, Gerben en Jan. Vooral een dank aan Hylke, die mij de weg in de promovendiwereld op het IMAU heeft wijsgemaakt.

Saskia, in de zomer van 2008 heb ik jou ontmoet. Mijn leven is door jou vrolijker geworden en dat heeft ook op mijn werk een positieve werking gehad. Je hebt met volle aandacht naar mijn onderzoek geluisterd en mij uitgedaagd om het verhaal in leekmanstaal uit te leggen. Daarnaast heb je me heel veel geholpen bij de Nederlandstalige stukken in dit proefschrift.
Ikke minst skal jeg takke alle sammen i Norge og Spania, selv i de vanskeligste tider har dere alltid visst sikkert at jeg skulle fullføre denne oppgaven.

Curriculum Vitae

Ik, Simon Looijen Axelsen, werd op 23 april 1978 geboren te Arendal, een stad aan de zuidkust van Noorwegen. Arendal is omringd door meerdere eilanden en op zo'n eiland, Tromøy, woonde ik vanaf het jaar dat ik voor het eerst naar school mocht tot ik 17 was. Zoekende naar iets nieuws, besloot ik om als uitwisselingsstudent naar het vaderland van mijn moeder (Nederland) te vertrekken. Van 1996 tot 1997 heb ik ruim tien maanden puberstreekjes in Reeuwijk en het nabijgelegen Gouda uitgehaald. De maatschappelijke vrijheid die mij toen overspoelde vond ik zo fascinerend, dat ik besloot om ooit terug te keren naar het zo dichtbevolkte land.
Na terugkeer naar Noorwegen heb ik de middelbare school afgerond en stond ik te popelen toen Koning Harald mij een groen uniform gaf. Al gauw besefte ik dat ik meer uitdagingen nodig had dan de dienstplicht mij kon bieden. Het besluit om te gaan studeren was snel genomen. Onderweg naar Nederland heb ik van 1999 tot 2003 op het Niels Bohr instituut te Kopenhagen, Denemarken, natuurkunde gestudeerd. Toen daar werd besloten in het cursusaanbod te snijden, kocht ik een enkele reis naar Utrecht.
In 2005 heb ik de masteropleiding Meteorologie en Fysische Oceanografie tot goed einde gebracht en kon ik gelijk aan mijn promotieonderzoek beginnen. Het eindresultaat van dit onderzoeksproject, dat net iets meer dan vier jaar heeft geduurd, is het boek dat je nu vasthoudt.